LBL-5725
c.1

LASER VELOCIMETER WITH HIGH SPATIAL RESOLUTION

Calvin Tom Chew
(M. S. thesis)

September 1976

Prepared for the U. S. Energy Research and
Development Administration under Contract W-7405-ENG-48

For Reference

Not to be taken from this room

LAWRENCE BERKELEY LABORATORY
UNIVERSITY OF CALIFORNIA
BERKELEY

LBL-5725
c.1

DISCLAIMER

This document was prepared as an account of work sponsored by the United States Government. While this document is believed to contain correct information, neither the United States Government nor any agency thereof, nor the Regents of the University of California, nor any of their employees, makes any warranty, express or implied, or assumes any legal responsibility for the accuracy, completeness, or usefulness of any information, apparatus, product, or process disclosed, or represents that its use would not infringe privately owned rights. Reference herein to any specific commercial product, process, or service by its trade name, trademark, manufacturer, or otherwise, does not necessarily constitute or imply its endorsement, recommendation, or favoring by the United States Government or any agency thereof, or the Regents of the University of California. The views and opinions of authors expressed herein do not necessarily state or reflect those of the United States Government or any agency thereof or the Regents of the University of California.

0 0 0 0 4 6 0 8 0 4 1

LBL-5725

LASER VELOCIMETER WITH HIGH SPATIAL RESOLUTION

Calvin Tom Chew

Materials and Molecular Research Division, Lawrence Berkeley Laboratory
and Department of Chemical Engineering, University of California,
Berkeley, California 94720

ABSTRACT

Aspects to be considered in the design of a laser Doppler velocimeter have been studied in detail. These aspects were applied to the construction of a velocimeter capable of high spatial resolution and accurate scanning. Moreover the device operates interchangeably both in the reference and differential modes, thus giving the three velocity components at any selected point of measurement. Experiments have been performed with the velocimeter to test its reliability in velocity measurements. These tests have been carried out using a rotating disk and scaled down flow channel.

0 0 0 0 4 6 0 8 0 4 2

Table of Contents

ABSTRACT v

I. INTRODUCTION 1

A. The Electrochemical Reactor Cell 1

B. The Laser Doppler Velocimeter 2

II. SPECIFICATIONS AND DESIGN CONSIDERATIONS 6

III. THE CONSTRUCTION 16

A. Mounting Stage for the Velocimeter 16

B. The Observing Lens 23

C. The Laser Module 25

1. The Laser 25

2. The Depolarizer Spatial Filter 25

3. The Laser Mount 30

D. The Translator Module 32

IV. THE TWO MODES 36

A. The Reference Mode 36

1. Theory 36

2. Signal Contrast 39

3. Reference Beam Sources 42

i) glass plate 42

ii) path compensator 48

4. Probe Volume 51

B. The Differential Mode 60

1. Theory 60

2. Beamsplitters 63

3. The Geometric Beamsplitter 69

a. Theory and contruction 69

b. Mount 75

c. Shortcomings 77

4. The Amplitude Beamsplitter 78

a. Theory 78

b. Construction 85

c. The Beamsplitter Mount 91

d. Advantages 93

5. Altering the Probe Volume 97

6. Scattering Particles 100

V. EXPERIMENTAL 103

A. Differential Mode 103

B. Miniature Flow Channel 104

C. Rotating Disk 110

D. Hollow Metallized Glass Spheres 114

VI. CONCLUSION 118

APPENDICES 120

REFERENCES 136

ACKNOWLEDGEMENTS 142

0 0 0 0 4 6 0 8 0 4 3

I. INTRODUCTION

A. The Electrochemical Reactor Cell

The hydrodynamic boundary layer through its influence on the mass transfer boundary layer has a large effect on the electrolytic mass transfer rate. Since these layers determine the limiting rate of electrode reactions, their understanding is vital to the design of such electrochemical processes for energy conversion, synthesis of chemicals and the preparation of metals.

In studies on the deposition of copper onto a horizontal upward facing copper cathode, Tobias and Hickman[1] noted under certain current densities and Reynolds numbers that the electrode became streaked. Close examination of the cross section of the cathode surface reviewed a series of crests and troughs. This pattern was attributed to the combined effects of forced and natural convection.

When air near the earth's surface is warmed by the sun, it becomes less dense and rises. Wind blowing across the earth's surface also imposes forced convection normal to the density driven natural convection. The velocity field under combined forced and natural convection will be neither the hexagonal cells of natural convection, nor the laminar flow of forced convection, but under certain conditions result in roll cells.[2,3] Driving forces similar to this case but on the electrode led the above authors to suggest the existence of roll cells on the electrodes. But attempts to confirm the flow field using dark field microscopy were unsuccessful.[4]

Experiments on the horizontal electrode rectangular duct $Cu/CuSO_4/Cu$ electrochemical reactor showed significant increases in the limiting current in the flow regime of combined natural and forced convection. McLarnon in his interferometrically[5] obtained concentration profiles on the same system gave only qualitative information on the effects of natural convection since light deflection effects represented an integrated effect through most of the boundary layer.

B. The Laser Doppler Velocimeter

An earlier reference mode laser Doppler velocimeter had been built for viewing the flow cell,[6] but the device was much too crude for measuring the more interesting boundary layer region. Also several years of neglect together with no processing electronics being provided had left the velocimeter inoperable. Hence the present device was designed and constructed. Since interferometric studies yielded data only on concentration fields, the velocimeter was built to provide data on the hydrodynamic field. The combined data of these two instruments would well characterize the reactor system.

Interferograms in the regime of combined forced and free convection could also aid in correcting the location of probe volumes shifted by light deflection. Since the concentration changes little in the flow direction a two dimensional theoretic profile can be modeled. This could be sectioned into layers of constant concentration and a computer solution to light deflection can be calculated. If the resulting model and interferogram match, then this model could be used to correct for the location of the probe volume (see Fig. 1).

0 0 0 0 4 6 0 8 0 4 4

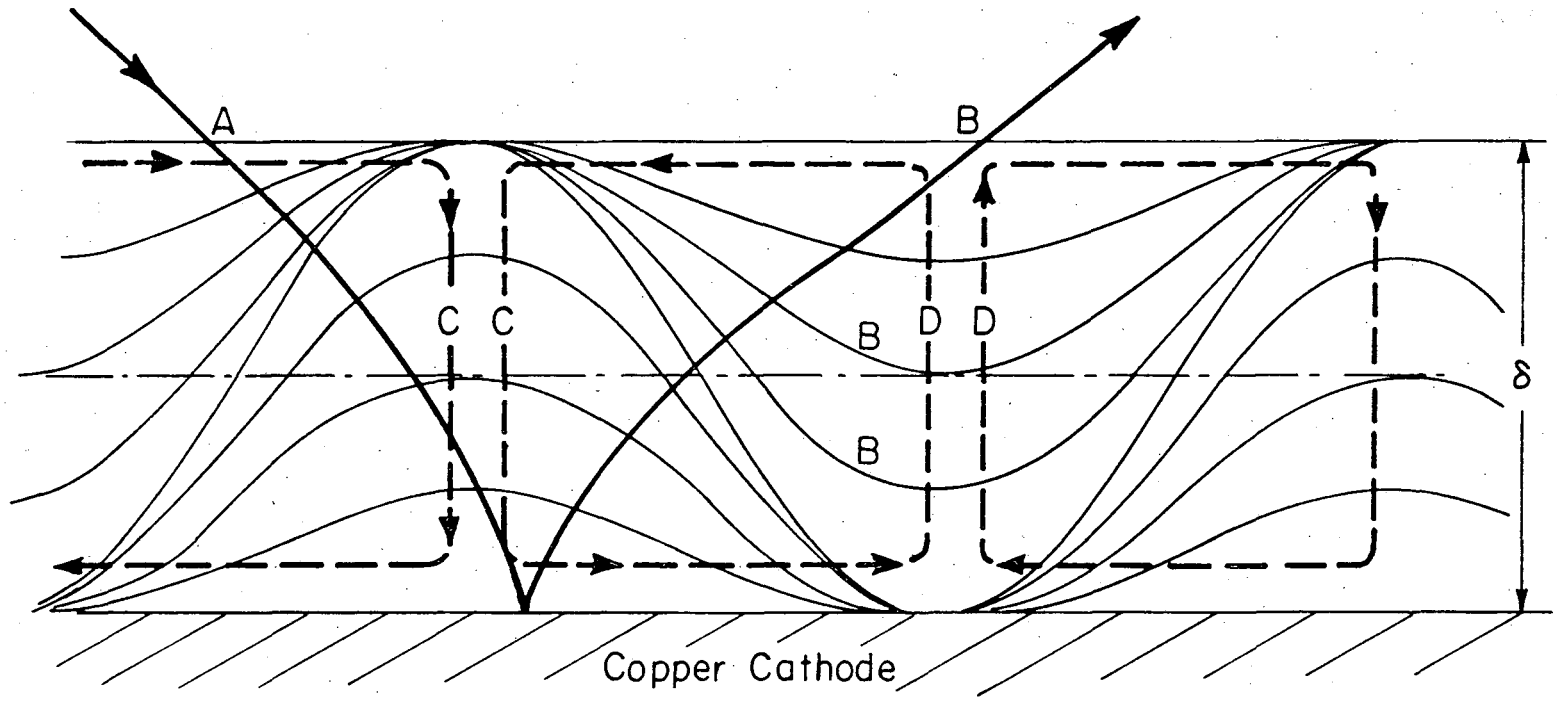

XBL 768-7418

Fig. 1. Light delfection caused by concentration gradients A laser beam is deflected by a hypothetical sinusoidally varying concentration field.

Symbols:
- A Laser beam
- B Lines of constant concentration
- C Sinking of heavier fresh electrolyte down to the electrode
- D Upwelling of the less dense exhausted electrolyte
- δ Boundary layer thickness

Alternative methods for quantitative velocity field determination exist, but are not as accurate as the laser velocimeter. The advantage of this instrument over other methods like hot wire anemometry are that the fluid is left unperturbed by the probe, the signal needs no calibration, and the signal is linearly proportional to the velocity.

Its advantages over other optical methods such as dark field microscopy is its finer light scattering particles which more closely represent the flow of the fluid. Microscopy cannot maintain a sufficient depth of focus when measuring the velocity of micron sized particles, nor can it measure velocities with the same accuracy. It also cannot give the velocity component along the microscope's optical axis if it is to have a sufficient depth of focus. The velocimeter with its very small probe volumes provides measurements approximating point velocities and with the locations of each point of measurement selected with accuracy, greatly excells over dye techniques. Measurements by laser velocimetry on velocity profiles in ducts for laminar[7-11] and turbulent flow[14-16] agrees well with theory and alternative techniques of measurement. The method has been well established as reliable and hence the laser velocimeter is well suited for studied on the flow in question.

The principle of a laser Doppler velocimeter is based on two simple wave phenomena, the Doppler effect and the superposition (linear addition) of waves. When monochromatic light scatters form a moving particle, its frequency experiences a Doppler shift, much like the famous red shift in celestial bodies. The interference of the shifted wave with that of an unshifted wave yields a beat frequency.

Since the beat frequency is linearly proportional to the particle velocity, one can back calculate the particles' velocity.

Yeh and Cummins[17] were the first to build a laser Doppler velocimeter. Rudd[18] and Durst[27] suggested alternative optical geometries to the Yeh and Cummins reference mode. Goldstein and Hagen[12] first reported the use of the differential mode geometry for measuring turbulent flows.

Various improvements have been made but mainly on the differential mode. These include rotating diffraction gratings,[19] acousto-optic,[20,21,62] and other[22,63] devices which shift the frequency of one beam by a fixed frequency onto which the Doppler frequency is added, thus giving directional sensitivity to the velocity measurements. Directional sensitivity has also been obtained by using a phase shift on one of the velocimeter's beams.[23,64] Other improvements were the simultaneous reading of two velocity components in a confocal backscatter system,[24] a three beam two component velocimeter,[25] white light velocimeters,[26,46] and electronic signal processing schemes.[28-30,65,67] Detailed analyses of signals have also been done[19,32,33,70] which included studies on the effect of scattering particle concentration[68] and probe volume cut off[31] on signal characteristics.

Laser Doppler velocimeters have been employed in a number of studies. Among these are blood flow in capillaries,[34] interstitial flows in packed beds,[35] statistical averages in turbulent velocities,[14] velocity profiles in flame jets,[36] vortices resulting from air flow over a sharp edge,[23] high current arc discharges,[37] electrokinetic studies[38,66] shock front velocities,[39] and measurement of the true airspeed of aircraft.[69]

II. SPECIFICATIONS AND DESIGN CONSIDERATIONS

In order to determine flow fields close to the electrode the velocimeter must have met the following specifications:

1) obtain all three spatial components of the velocity vector
2) have high spatial resolution (a small probe volume)
3) and scan the boundary layer with accuracy (account for light deflection when necessary)

Interferometric studies on the flow cell have shown for measurements in the mass transfer boundary layer, that light deflection errors on transmitted beams create considerable errors in the determination of the location of a measurement in the electrolyte. Moreover with the onset of natural convection deflection corrections of transmitted rays become very complex.

Light deflection effects could be minimized by a number of design features. Whereas viewing flows at an angle normal to the cell window simplified both the geometric factors in calculations and the equipment design, it unfortunately compounds deflection errors since rays must now pass through the region of highest concentration gradients. Observing the flow near the walls reduce deflection errors but the flows would have shown wall effects strongly. In addition blockage of one of the incident beams while in the differential mode would not have permitted measurements of one velocity component without extensive design modifications on the present flow channel. A three beam two component[25] laser velocimeter could have been used here to simultaneously

give two velocity components, but the duplication in electronics would have been too costly.

The above effects could be minimized by observing the boundary layer at a down ward angle. In this case both the incident and signal beams would have traversed a fully turbulent region of fairly constant index of refraction, and entered the boundary layer only at the location of measurement. Since the mass transfer layer was smaller than the hydrodynamic layer any effects of the flow field such as roll cells could have been observed in the region.

Most laser Doppler velocimeters so far constructed or which are commercially available have been forward scatter devices, probably because the forward scatter signal intensities were two to three orders of magnitude larger than the signals from backscatter devices.[34,40] Thus initial considerations were to purchase a forward scatter velocimeter[41-43] and modify it for viewing at an angle to the surface (downward observation) to avoid the penetration of the light through many of the light deflecting eddies. This downward aiming of the source optics (see Figs. 2 and 3) and the downward viewing of the receiving optics on the opposite side of the cell would have greatly reduced deflection effects of the large density gradients near the electrode surface.

But this set-up when mounted onto the flow cell showed several shortcomings. Because the measurements were taken quite close to the electrode which is of polished copper there was a forward reflection and a dimmer backreflection. (Roughening and corrosion of the electrode created a somewhat opaque surface allowing a diffuse back reflection)

Fig. 2. Forward scatter velocimeter in the differential mode. By observing the electrode at an angle $\theta=0$ one of the illuminating beams of the differential mode (A) is blocked by the electrode (G).

Symbols:

A Illuminating beams of the laser
B Camera lenses
C The flow cell which the velocimeter is probing
D Portions of beams A, reflected from the electrode surface into the collecting optics.
E Supports for the flow channel
F Glass walls of the flow channel
G Polished copper electrode
H Cone of light (signal beam) collected from scattering particles travelling through the illuminated probe volume (focal region)

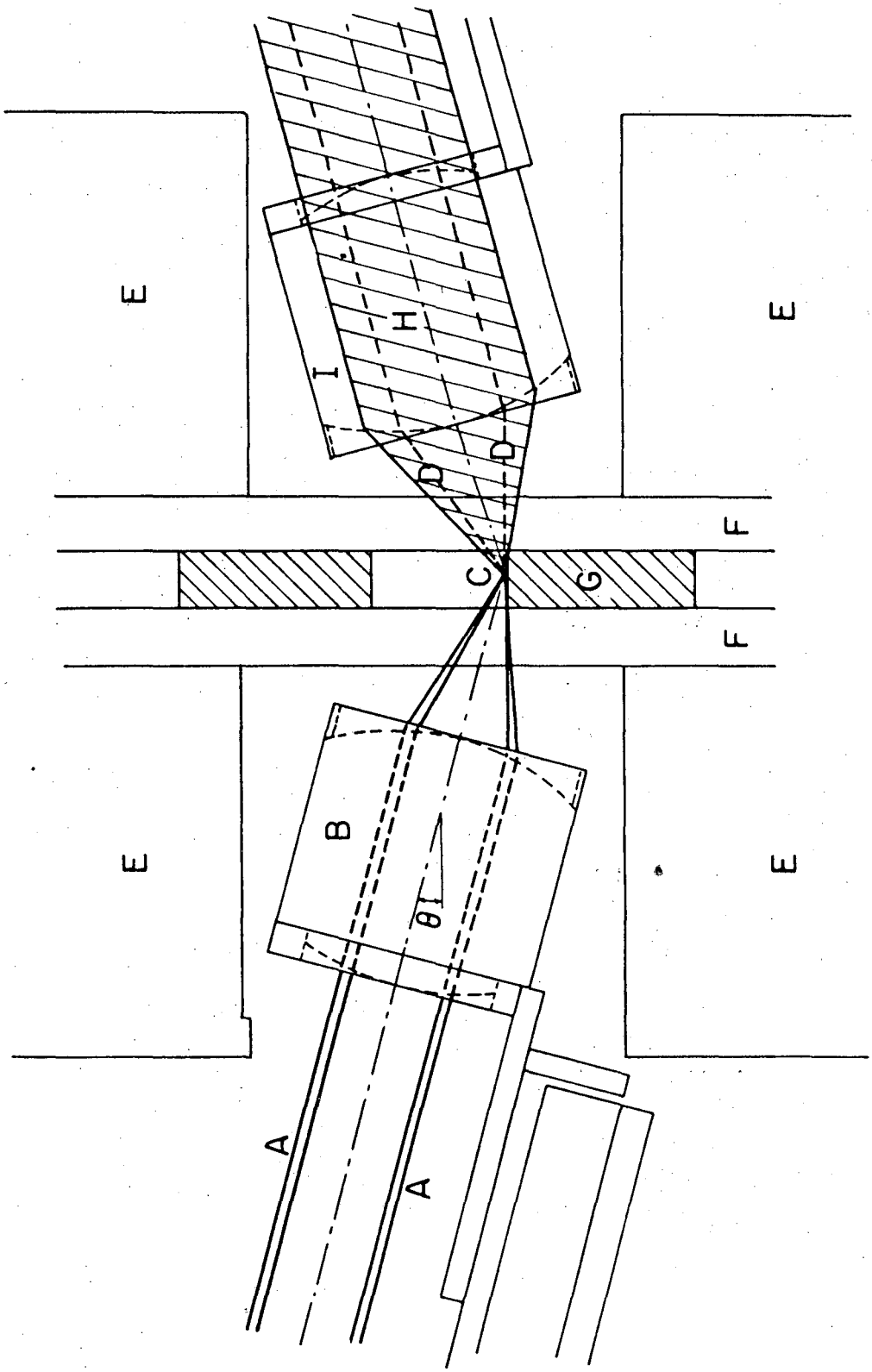

XBL 768-7422

Fig. 2.

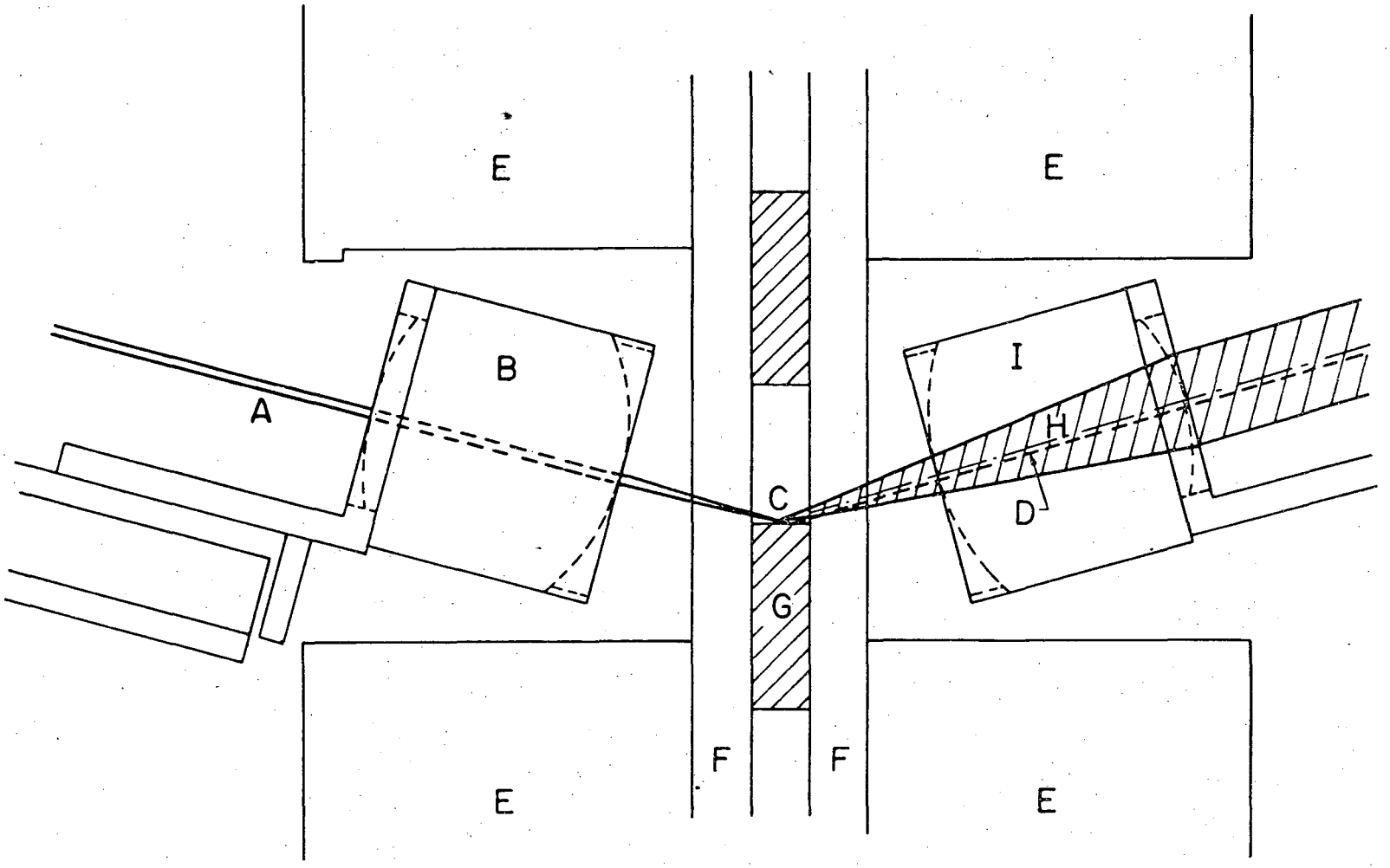

XBL 768- 7423

Fig. 3. Forward scatter velocimeter in the reference mode. The beam reflected from the polished electrode D, could easily enter coaxially into the collecting optic I. A beam entering at this position cannot be removed with a spatial filter and would reach the phototube.

Because of the forward reflection the much larger D.C. signal induced by this reflection would have washed out the smaller ac signal.

The flow channel size and platform built for the velocimeter would have required an overhead precision rail to suspend the receiving optics from the source platform. Such a rail would interfer with the removal of cell windows for the cleaning and polishing of the electrodes. And because of the rail's length, it would also introduce mechanical vibrations into the system.

Although the translators needed on both the source and receiving otpics assemblies would have increased construction time and investment, it was not the most unfortunate feature of the forward scatter device. The most serious shortcoming was the need to go focal point hunting with the observing optics. Since the cell windows refract and the concentration gradients deflect the illuminating beam and forward-scattered signal beam by an unknown amount, superimposing their focal points is very difficult. The focal point of the illuminating beam must be hunted with the observing optics until it is found by trial and error. Unless the observing optics is aligned with the focal region of the source optics the probe region will be unilluminated and hence give no signals. When the translators are shifted to probe another region, this trial and error focal point hunting must be repeated. This would have been an exceedingly tedious process even for the probing of a velocity field with a fairly coarse grid. (A 5×5×5 grid would have required 125 alignment procedures.)

Placing the illuminating an observing optics coaxially does not alleviate the above problems. In this case the beams traverse the largest number of light deflecting eddies and thus their focal points are shifted by an uncertain distance. This again required focal point hunting. (see Fig. 4) A coaxial optics configuration (as shown in Fig. 5) is especially poor for the reference mode because there can be much play in the observing focal point which could still observe a region with illuminated particles. This would create a large uncertainty in the location of the probe volume.

For study the y^+, (the dimensionless distance from the interface), dependence in the universal velocity profile[44] the refracted paths of the beams due to the glass wall is more easily calculated if cells with lucite walls with p-xylene or cells of glass walls with aniline were used. In the above cases the index of refraction of the window material is equal to that of the fluid so that beam deflections are calculable. The receiving optics can then be positioned beforehand by a precalculated amount.

Fig. 4. Coincidence of illuminating and observing probe volumes in the presence of deflection at the boundary layer and refraction at the cell wall.

Symbols:

A Illuminating beams
B Illuminated probe volume (focal region) displaced by light deflection and refraction at the cell wall
C Probe volume (focal region) of collecting optics
D Cone of the signal beam collected by lens E
E Lens collecting the signal
F Lenses of the spatial filter
G pinhole of spatial filter, restricting accepted light to that originally at the probe volume
H Photodetector
I Electrode
J Cell windows

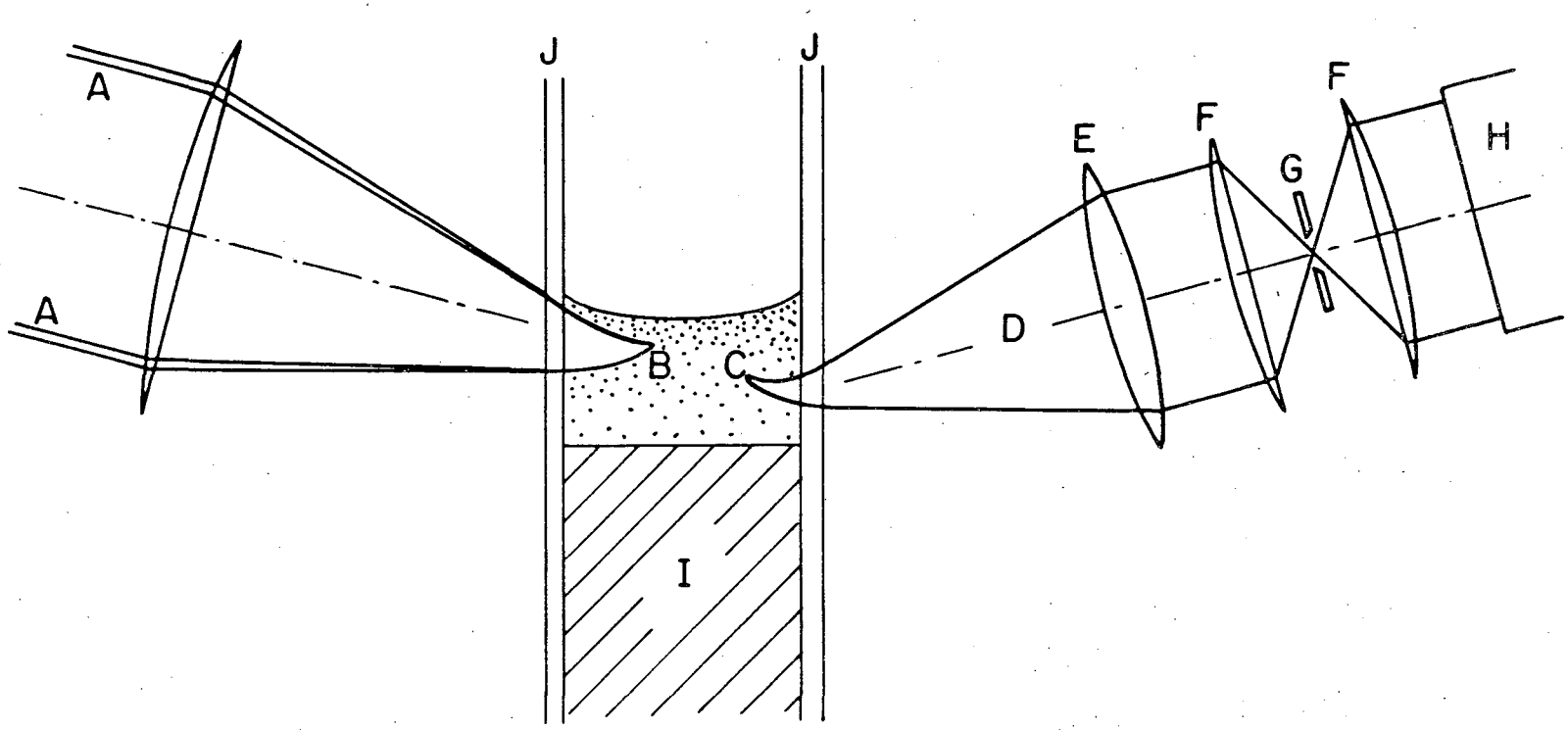

XBL 768-7424

Fig. 4.

0 0 0 0 4 6 0 8 0 5 0

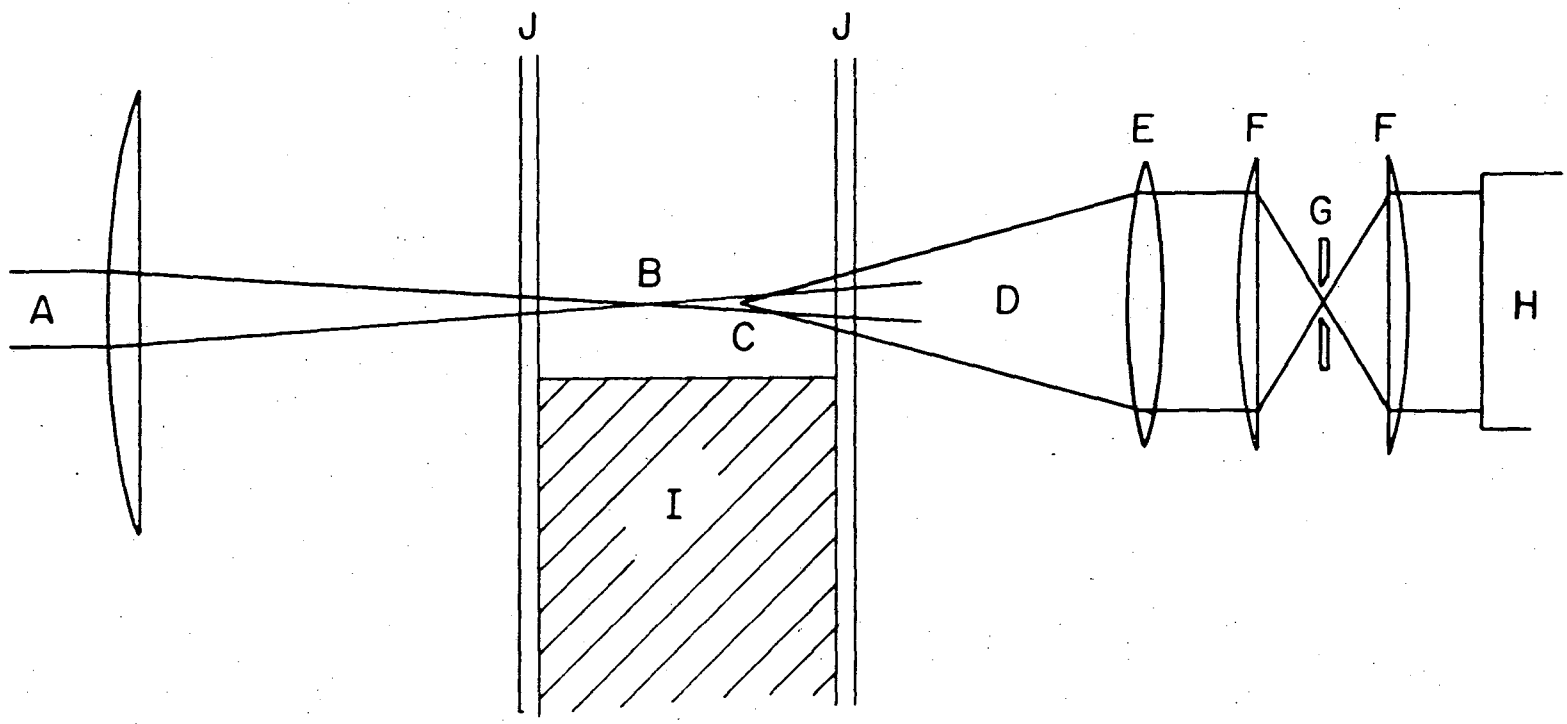

XBL 768-7425

Fig. 5. Reference mode with coaxial optics. Illuminated focal region is sampled by optics with point of observation C.

III. THE CONSTRUCTION

Figure 6 illustrates the final design of the laser Doppler velocimeter. The laser output (A) was first sent through a depolarizer spatial filter module. It then entered the beamsplitter module, and was brought by three mirrors into the beam positioning module. It then entered the translator module, which permitted the focal point of the observing lens (G) to be moved along the flow channel window. Light was backscattered from particles in the channel and returned confocally through the translator, into a spatial filter assembly (I,J,K), and finally into the phototube assembly. The output from the phototube when connected to a spectrum analyzer would then give the frequency of the Doppler beat. The laser, the above modules and the path compensation module were all mounted onto a rigid base plate for geometric stability.

A. Mounting Stage for the Velocimeter

The previous velocimeter had once rested on a lathe bed aluminum platform, which also supported a refractometer on the opposite side of the channel. The platform was constructed of 1/2 in. "U" plates (as shown by Beach[6]) and rode on grooved wheels. The platform was unstable because of its light open structure and the loose sockets of the grooved wheels. Weight placed on one side of the platform (velocimeter), was enough to raise the height of the opposite refractometer side. The platform slid easily toward and away from the channel since the wheels were not flush against their sockets. Not only did the

Fig. 6A. Overall view of the laser Doppler velocimeter operating in the reference mode. The laser beam is filtered and depolarized at A, and is brought by a series of mirrors C, through a hole in mirror D. The beam then goes through a stack of X, Y and Z translators (E,P and O) to the focusing lens G. At G the beam is focused into the flow channel. Light scattering from latex spheres seeded in the channel electrolyte (H) is also collected by G. The signal beam is positioned into the spatial filter (I,K,C,K) by mirror D. A reference beam is generated at N, and is sent through a path compensator, a neutral density filter R and a beam expander S. The expanded beam is superimposed onto the signal beam at the glass slide N'. The superimposed beams interfer, and the resulting intensity variation (the Doppler beat frequency) is converted into an ac current by a phototube.

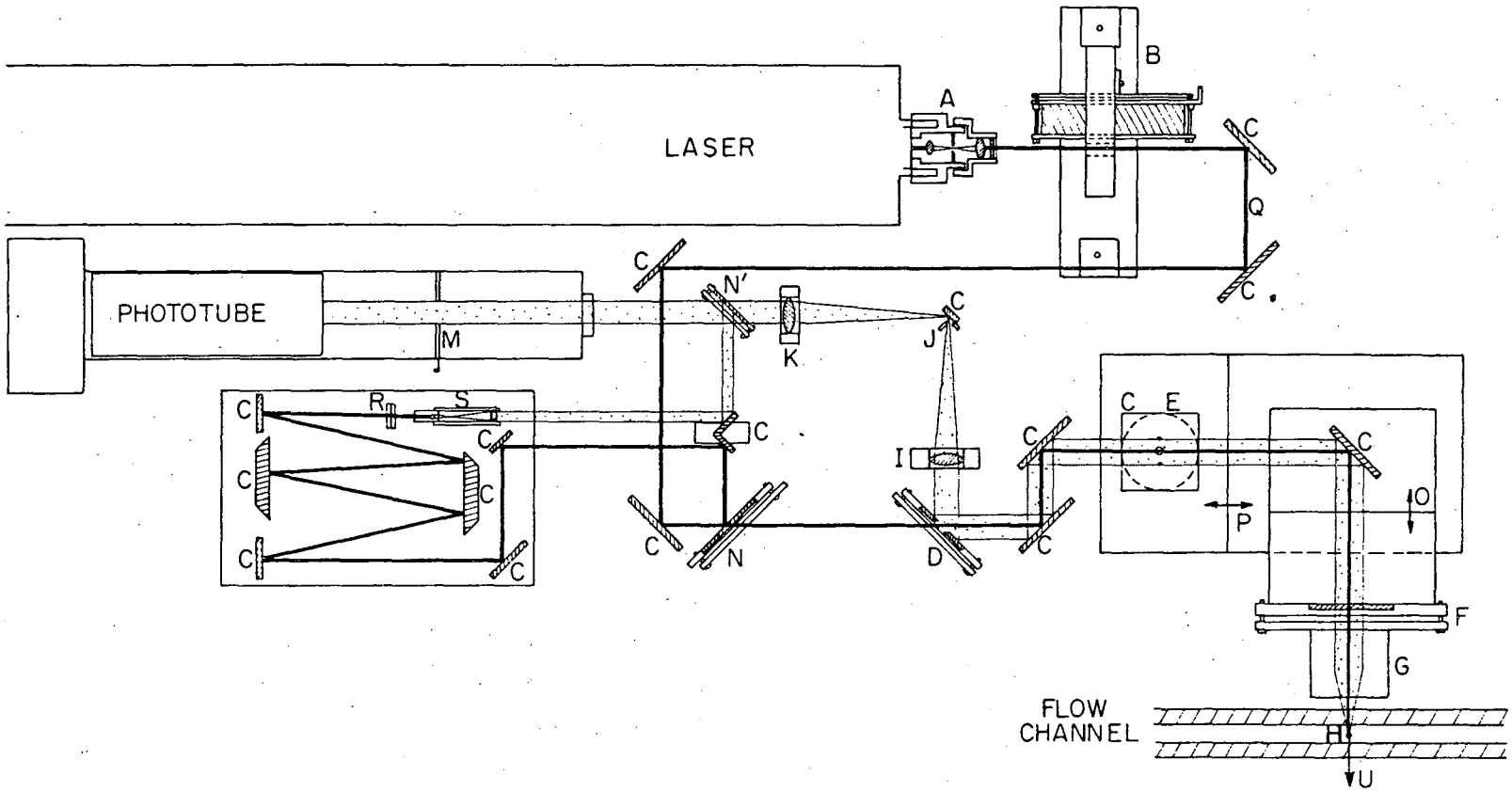
LASER
A
B
C
Q
PHOTOTUBE
M
N'
K
J
R
S
I
E
P
O
D
N
F
G
FLOW
CHANNEL
H
U
XBL 768-7428

Fig. 6A.

Fig. 6B. Overall view of laser Doppler velocimeter operating in the differential mode. The laser beam is split into two beams of equal intensity at beamsplitter B. The pair of beams Q travel through two holes in mirror D and finally arrives at the focusing lens G. The pair of beams are then focused into the flow channel.

Symbols:

A Depolarizer and spatial filter
B Rotatable beamsplitter (slides out of laser beam path for operation in the reference mode
C Opaque first surface aluminum mirrors
D Mirror with five holes to allow passage of laser beams
E prism of vertical translator assembly
F Former location of coated glass slide used as a reference beam source (replaced by path compensator, N and N').
G Camera lens
H Micron sized Dow latex spheres
I 88 mm achromat lens
J 50 micron diameter pinhole, part of the spatial filter assembly
K 100 mm lens
L Spectral filter (.6328 microns)
M Iris diaphragm
N Reference beam source (glass plate with side where exit beam exits coated with a MgF_2 antireflective coating)
N' glass plate where signal and reference beams are united before entering the phototube
O Direction of motion of Y translator
P Direction of motion of X translator
Q Illuminating laser beams
R Neutral density filter
S Beam expander (9.6:1)

Backscattered signal beam and reference beam

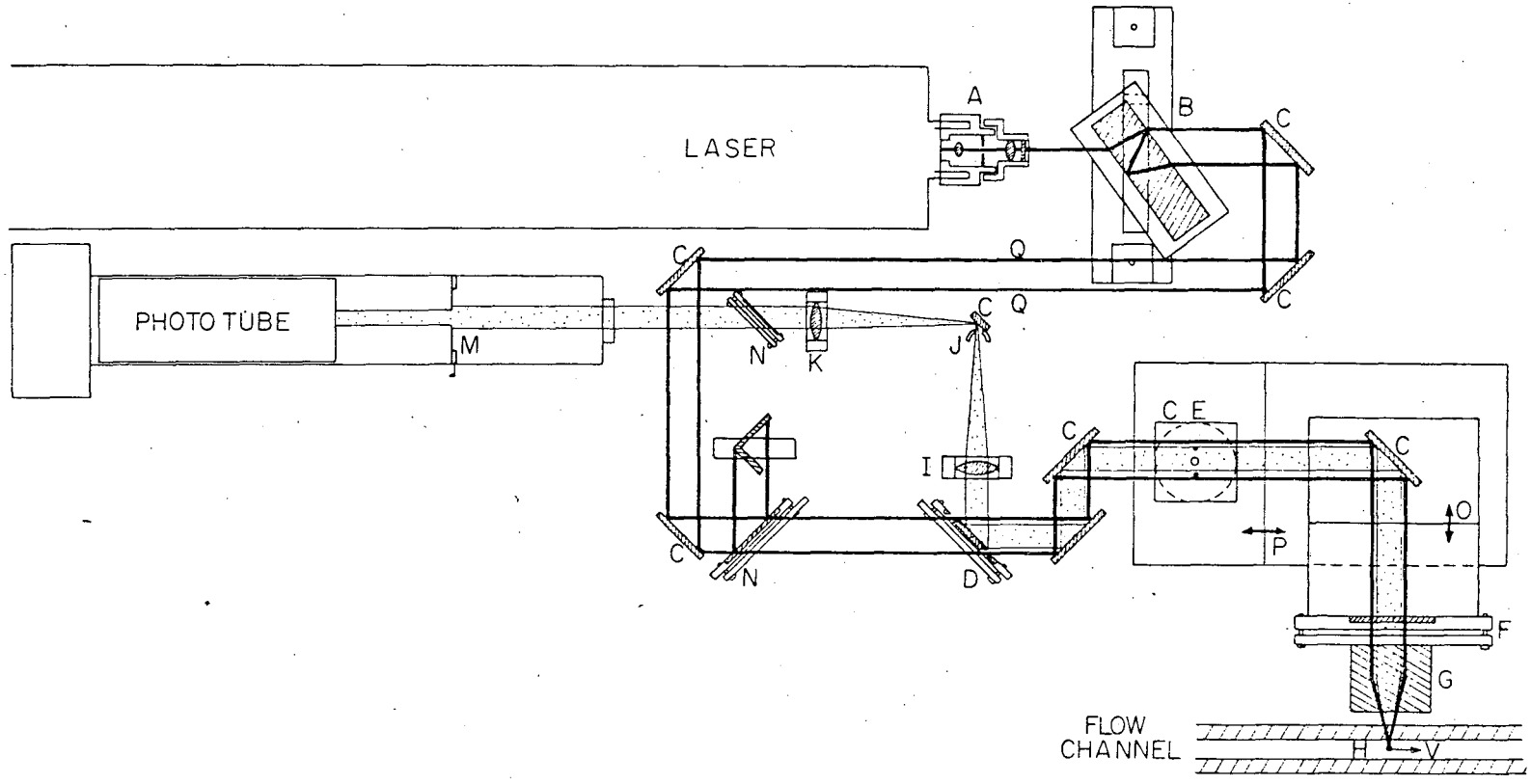

XBL 768-7429

Fig. 6B.

0 0 0 0 4 6 0 8 0 5 3

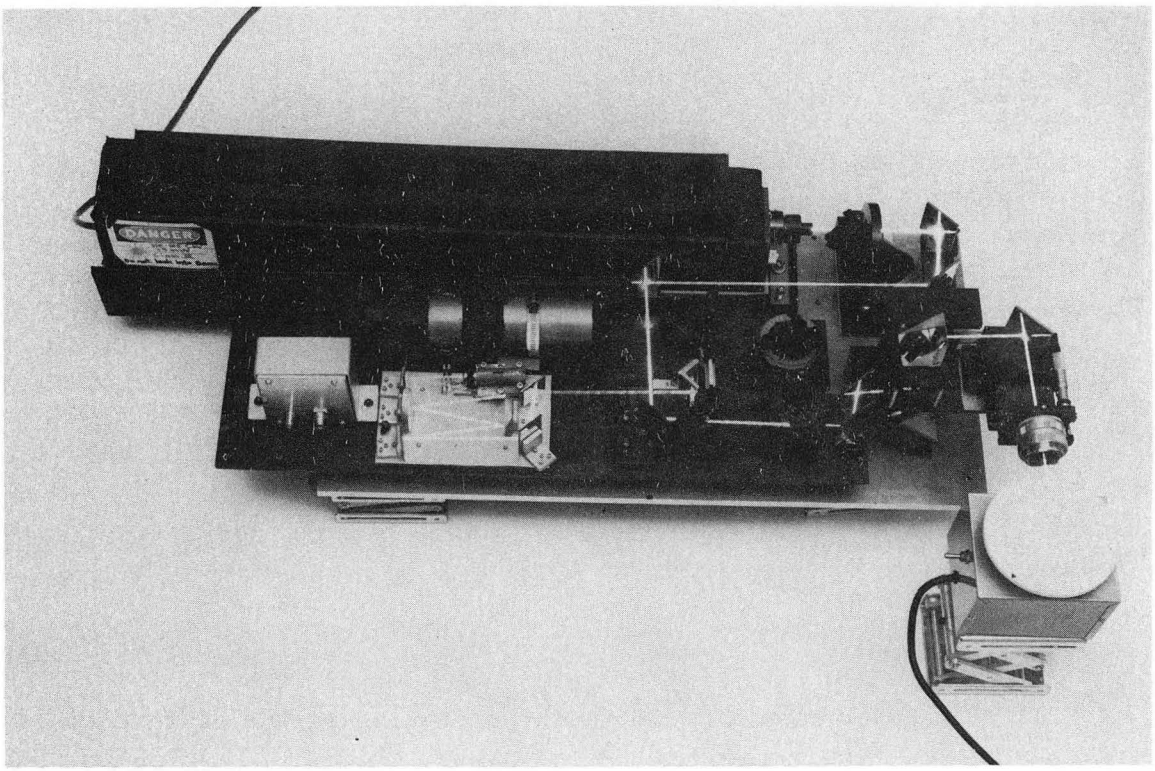

BBC 768-7310

Fig. 7A. Laser Doppler velocimeter operating in the reference mode.

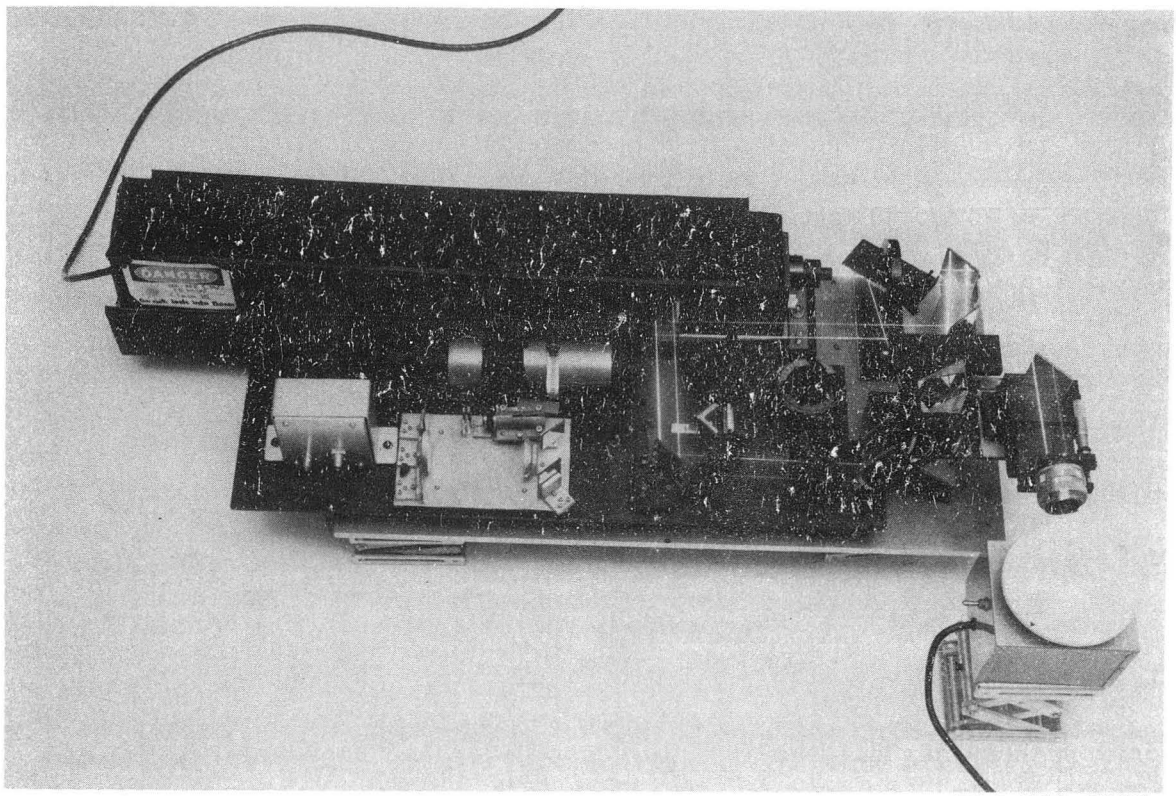

BBC 768-7307

Fig. 7B. Laser Doppler velocimeter operating in the differential mode.

wheels slide, but the platform rotated if pressure was put on one corner. Washers were placed between the grooved wheels and the socket walls, eliminating play and a number of lead bricks were placed under the refractometer to counterbalance the weight of the new and much heavier velocimeter. The additional weight of the velocimeter on the platform also stopped slippage along the rails running along the channel, and dampened vibration.

A crude and weak coarse vertical adjustment mechanism was removed from the platform, and a hinged plated was added. This plate would tilt the velocimeter base plate into a downward observation angle. The laser velocimeter baseplate was bolted to slotted holes in the hinged plate such that during experiments coarse adjustments of the velocimeter toward the channel could be made, and during the disassembly and cleaning of the flow channel, it could be backed away from the channel.

Although the hinged plate allowed observations angles from 0° (normal to cell walls) to 25°, the angle was set at only 15°. Larger angle could not be used otherwise the lens would not fit into the recess between the window and frame of the flow cell.

B. The Observing Lens

A large beam separation was necessary to produce small probe volumes which can be approximated as points in a velocity field. Large solid angles of signal collection are necessary for good signal to noise ratios. The above both require a large relative aperture.

Initially a one inch diameter achromat lens was used which allowed a good range of beam separation and a fair amount of mobility in the 3 in. deep by 3 in. high flow channel wall recess preceding the cell window. (photo from Beach[6] thesis) But such lenses are increasingly less corrected for chromatic, astigmatic, spherical aberration, coma, distortion and field curvature at their edges. More importantly the probe volume cannot be calculated. Generally only in reputable camera lenses can one assume that the beam diameter at the focal point is nearly diffraction limited and hence calculable. Projector lenses are not as critically corrected and corrected more for the central part (green) of the spectrum. (The laser beam was red)

Lenses made for cameras included various bulky rings for attachments and adjustments as focus and iris settings. The front lens was larger than the back lens (facing the film). Yet a bulky barrel would hinder lens movement in the channel recess. Even after much searching, the best lens[45] was still bulky, with a 5.27 cm barrel diameter and a front lens diameter (5.16 cm) much larger than the back (2.29 cm). Since the lens was set to view at infinity, rays diverging from the light scatterers should have been entering from the back lens. This meant that the smaller diameter lens faced the flow channel, and would reduce the amount signal collected by $(5.16/2.29)^2$. Also the mount blocked a portion of the back focal length (~ 1 1/4 in.) which was already shorter than the front focal length, thus further restricting the distance at which the lens could view the electrode surface.

C. The Laser Module

1. The Laser

The laser module included the laser, its mount and a depolarizer-spatial filter. The Jodon Model HN15 laser was a continuous wave, 15 milliwatt minimum, 632.8 nanometer helium neon laser with a regulated power supply for low output noise. Efforts to install the depolarizer-spatial filter indicated that the laserhousing's mounting bezel was over 20 degrees off axis, and also not centered with the output beam. The laser was returned to Jodon for realignment.[46] It returned centered and coaxial to within 1 degree.

The laser power supply was rated for a 115 VAC line input, but there were a number of repairs needed for blown capacitors, resistors and fuses. Even after such repairs and the lowering of the starter voltage, capacitors continued to arc, especially when a warm plasma tube was activated. (Warm tubes required higher starting voltages.) It was finally discovered that the circuits were designed more closely for a 105 VAC line voltage input, and that the laboratory 125 volt input lines overloaded the circuits. After resistors were added to the circuit to correct this, no further problems with the power supply occurred even when the plasma tube was refired while it was still warm.

2. The Depolarizer-spatial Filter

The depolarizer-spatial filter was used as to filter out the non-lasing frequencies and parasitic modes of the laser. (Light non-parallel to the filters axis was blocked.) The spatial filter could have also been used as a beam expander if the back lens (lens facing

the laser) had been replaced with one of a shorter focal length.

Although a more aberration free microscope objective could have been used as the back lens, a coated achromat was used instead. This made the design and mounting simpler. The front lens is similarly an achromat. The pinhole was a drilled 2 mil hole in a 2 mil thick 1/4 in. diameter copper disk. This was attached to a grooved edge disk, and mounted as explained later. (see Fig. 8)

In front of the objective lens was a multiple order quarter wave quartz retardation plate.[47] It was used to depolarize (circularly polarize) the linearly polarized laser output. Because the beams reflected from a number of coated aluminum mirrors and from the beamsplitter for the differential mode, they experienced changes in polarization with each reflection as given by the Fresnel equations.[48]

If two linearly polarized beams of the same state of polarization (such as the signal and reference beams of the reference mode or the two illuminating beams of the differential mode) travel through different paths and different optical components, there will be a relative shift in their polarizations. If the relative shift results in a 90 degree shift in polarization, there will be no interference. For shifts less than 90 degrees, only portions of the beams which are of the same intensity and of the same state of polarization interfer. This results in a loss of signal strength and an increase in background noise from the noninterferring portions of the beams falling on the phototube. When the beams are initially circularly polarized the effects of relative shifts in polarization are minimized. Here the worst case,

namely the loss of one polarization component and consequently half the intensity through a Brewsters angle reflection, will still permit the other component to interfer.

The depolarizer-spatial filter was attached to the laser bezel of the laser housing by six screws which were also used to center it. A small set screw was loosened in the innermost ring and the back lens pinhole tubes were removed. The back lens tube was threaded to mount onto a low power laser[49] for alignment of the pinhole. The slitted tube of the pinhole holder was pushed onto the backlens tube and held there by friction. A knurled ring with three concentric recessed tap screws was soldered to the front of the pinhole tube. These held the previously mentioned grooved edge aluminum disk containing the pinhole.

The focus of the lens was adjusted to the pinhole by sliding the slitted tube towards the lens, and centering the grooved disk by the three ring screws to yield a maximum brightness through the pinhole. When aligned the pinhole and backlens tubes were unscrewed from the low power laser and slipped back into its bezel mount. Prior to remounting the location of the laser output spot was marked on a black swiss velour paper screen. When the tube was remounted, the six screws on the bezel mount were adjusted until the diverging beam exiting the pinhole was of the maximum intensity attainable and centered with the laser spot marking.

Onto the adjusted tube and bezel mount was slipped the snuggly fitting cylindrical cap containing the front lens and depolarizer. To bring the front lens into focus, the mount was removed, and location of

Fig. 8. Spatial filter and depolarizer. The quarter wave plate converts linearly polarized laser output to circular polarization. The spatial filter blocks out light from other modes and nonlasing transitions.

0 0 0 0 4 6 0 8 0 5 7

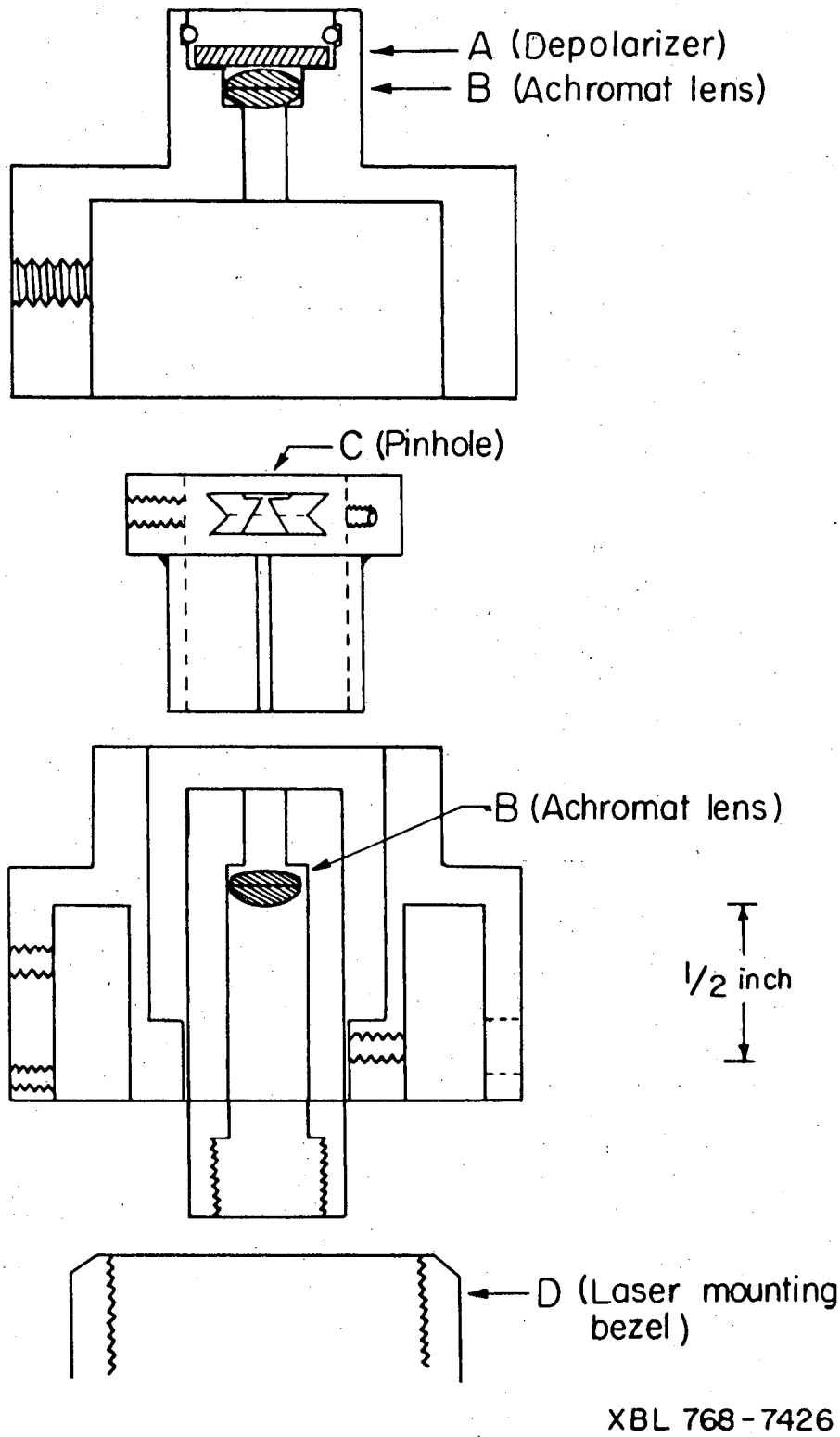

Fig. 8.

the expanded laser spot (1m radian divergence) on a screen at 18.5 ft. away was marked. The mount was replaced and positioned in the method mentioned earlier. The cylinder was then pushed inward until the image was a uniform intensity red disk, and showed no focal point along its projected path. Although the laser output had a maximum beam divergence of 1 mr, it was hoped that the telescope in addition to the filtering would reduce this. But instead the divergence is larger.

The cylinder was then rotated such that a polarizing filter showed no variations in intensity as it was rotated in the laser beam. This gave equal components in two orthogonal directions. Some refocusing was necessary with this adjustment. Finally the locking tap screw was tightened and the was thus cylinder secured.

3. The Laser Mount

The laser originally had four leveling feet, which provided a minimum separation between the base plate and laser of a half inch. From this gap air entered the perforated underside of the laser, and exited through a similar perforated top plate to provide air cooling to the plasma tube. The cooling was necessary to prevent thermally induced instabilities in the output (noise).

The straps were initially used to secure the laser to the base plate. But the pressure needed to firmly hold the laser in place warped the 32 inch long housing. This reduced the output by misaligning the mirrors. But more importantly, the stress on the plasma tube caused by the warping of the tube housing would have increased the likelihood of the tube cracking and leaking. If this occurred the tube

would cease to lase. Hence a light pressure was used to strap the laser, which resulted in frequent slippage and making frequent realignment necessary. The sinking of indentations in the base plate for the four leveler feet to prevent slippage was not feasible since this did not permit lateral adjustment of the laserhead.

The straps were removed in favor of a more rugged cradle. It was made of quarter inch thick right angle beams for strength. This also preserved the open structure needed for the air cooling of the plasma tube. The cradle was held to the laser housing using the threaded shafts which once held the leveling feet. Two 1/4 in. thick short plates were attached to the cradle and provided for leveling. The central bolt of the front plate was secured to the base plate, and acted as a pivot while two screws, one on either side of the center, and tapped into the plate, adjusted the height and tilt of the cradle front. Twelve inches from the rear of the cradle, where the cradle begins to extend beyond the baseplate, three holes, two tapped and one bored, were made in the baseplate. A crossbar on the cradle with a slotted hole and countersunk edges containing a sliding block "T" of aluminum with a 1/4 in. tapped hole fitted into the countersink and slot. The "T" block was pulled downward by the central bolt of the base plate, thus controlling height and pivoting. The two adjacent bolts pushed on the cradle frame and thus controlled tilt on the back end of the laser. Once the pivoting, tilt and height were adjusted, and the screws were tightened, no further slippage was observed.

The secured laser now allowed the building of a permanent light baffle which prevented stray light exiting the perforations of the

laser casing, from reaching the phototube and burying the low intensity signal.

Frequent realignment required removal of the previous baffle, requiring much time and causing damage from excessive dismantling. But now a permanent baffle was installed on the laser and also on the various modules. They were constructed of 16 ply cardboard and lined with strongly light absorbing swiss velour paper. (see Fig. 7)

D. The Translator Module

A system of precision translators[50] provided for the accurate scanning of the focal volume. A set of two horizontal and one vertical translator was mounted onto an interstage plate. To match channel height with that of the observing lens the vertical translator was mounted onto a block which was then bolted to the based plate. Onto one side of each plate was mounted a mirror or prism, and onto the opposite another translator. The observing lens was mounted as close to the level of and protruding as far as possible from the final translator to maximize lens mobility in the channel recess. The interstage plates mounted adjustably onto the movable portion of the translators, and as such allowed coarse vertical and forward (toward channel) adjustment. Coarse adjustment along the channel window was unnecessary since the lathe bed carrier upon which the velocimeter rested already traveled in that direction. Fine adjustments were on a 50 mm travel micrometers (.01 mm precision) pushing the spring loaded translators. All micrometers faced opposite to the channel for access during experiments.

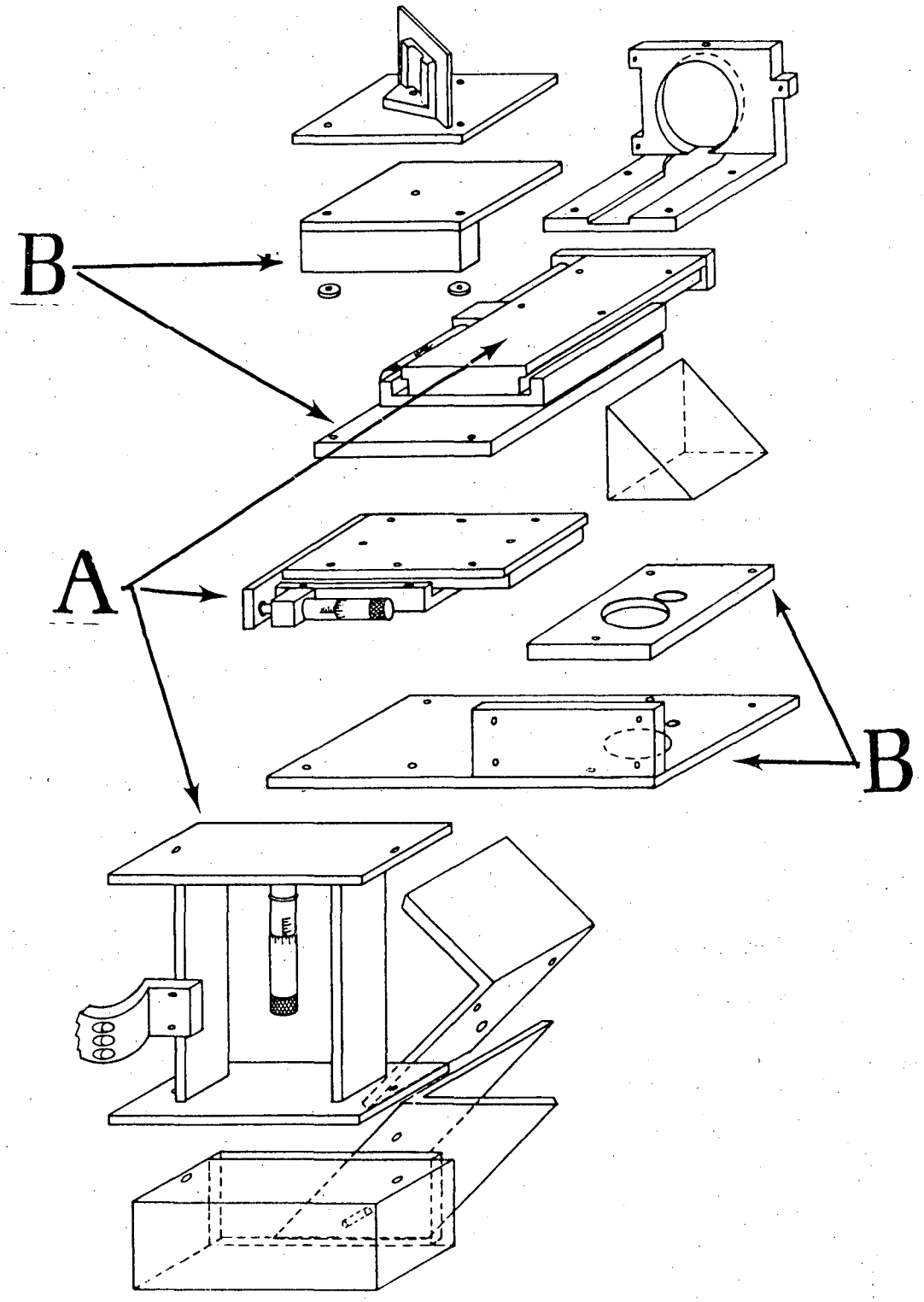

XBL 768-7427

Fig. 11. Exploded view of the translator module. The interstage platforms (B) and translators (A) are stacked so that the lens and the beams which illuminate the probe volume have three degrees of translational freedom in order to scan the velocity field in the flow cell.

The array of mirrors (Fig. 11) on the interstage platforms, were each mounted on a plate with one pull and three push screws for control of their rotation, height and tilt. Incident and signal beams entering the array parallel and coaxial with the observing lens axis remained parallel and coaxial as they traveled from the beam positioning module to the observing lens. Once the location of the focal point was established on the electrode its position after translation of the incident beam(s) can be calculated.

The last and most important design feature involved three of the above mentioned modules, the beam splitter, beam positioning, and path compensating modules. This gave us interchangeability of modes thus allowing measurement of the three velocity components, while remaining at the same probe volume location. Associated with this was also the desire to maintain a similar focal volume, or spatial resolution, as one shifted between reference and differential modes. To better understand the final selection of the present design it was necessary to also examine the limitations inherent in this device when operated in the reference and differential modes.

0 0 0 0 4 6 0 8 0 6 0

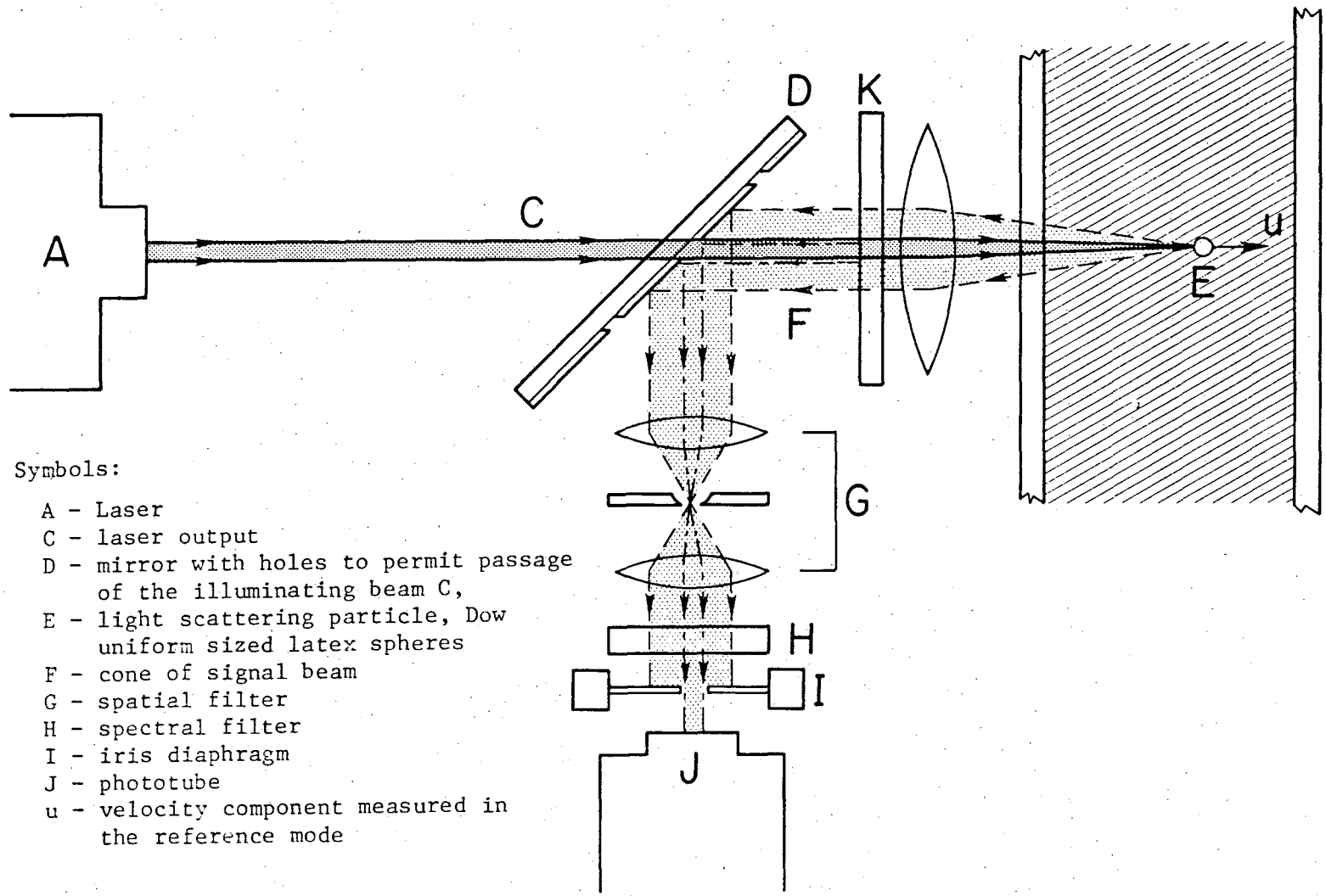

Symbols:

- A - Laser
- C - laser output
- D - mirror with holes to permit passage of the illuminating beam C,
- E - light scattering particle, Dow uniform sized latex spheres
- F - cone of signal beam
- G - spatial filter
- H - spectral filter
- I - iris diaphragm
- J - phototube
- u - velocity component measured in the reference mode

XBL 762-2197

Fig. 12. Simplified drawing of the reference mode as shown in Fig. 6A. The velocity parallel to the exis of the focusing lens is measured when operating in the reference mode.

IV. THE TWO MODES

A. The Reference Mode

1. Theory

When operating in the reference mode measurements are made of the velocity component along the optical axis of the observing lens. In a simplified drawing of this geometry, Fig. 12, the laser light is first divided into a low intensity reference signal (shown by the back reflected beam from plate K and mirror D) and a brighter beam that is focused into a flow cell. In the cell the flowing electrolyte is seeded with micron sized spheres of neutral bouyancy (latex spheres). Because these spheres are smaller than eddies and because of their neutral bouyancy they flow as part of the fluid.

When a latex sphere traverses the focal volume (E) it scatters light. But since the light scattering particles are moving the light frequency experiences a Doppler shift. The focusing lens then collects the backscattered signal and converts its spherical wavefront into a planar front. This planar wavefront is united with the planar reference beam wavefront. These superimposed signals are then sent through a spatial filter which excluded scattered light from particles outside of the probe volume. The superimposed beams interfer to give a Doppler beat whose frequency is converted by a phototube[52,53] into a current, is read by a spectrum analyzer,[54] and is displayed on a storage oscilloscope.[55]

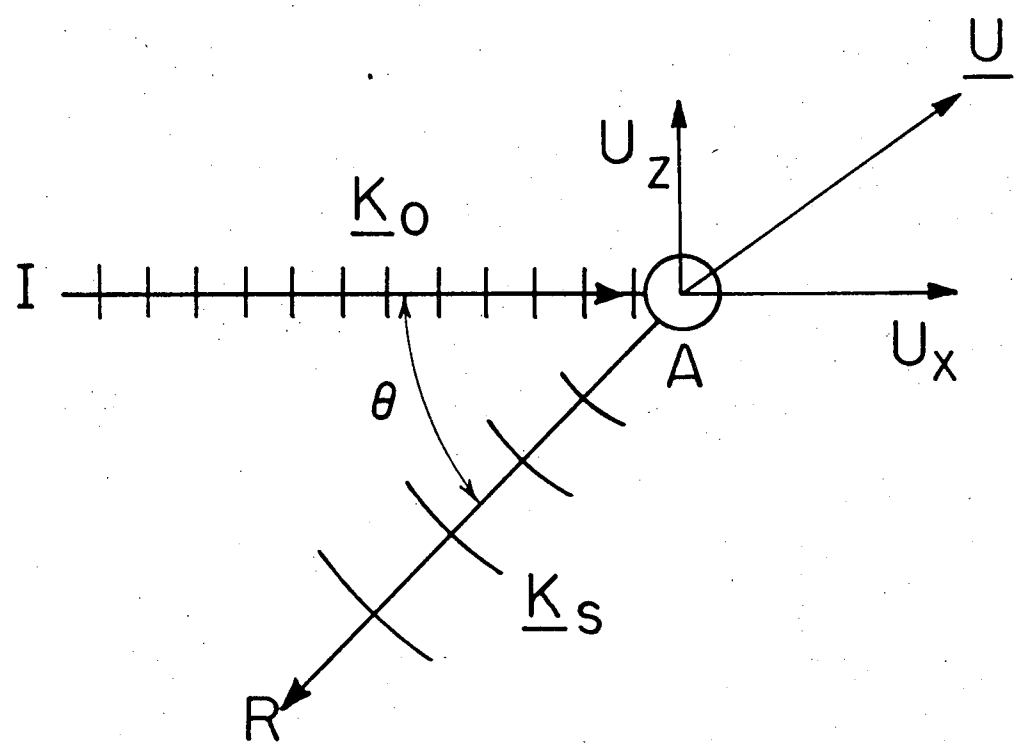

XBL 768-7430

Fig. 13. Light scattering from a moving particle.

Symbols:

I	incident wave, planar wave front
A	light scattering particle (micron sized)
R	the scattered wave, spherical wavefront
$\underline{U}$	the velocity vector of the moving particle, A
$\underline{K}_o$	the wavevector of the incident beam
$\underline{K}_s$	the wave vector of the scattered beam
$\underline{U}_z$ and U_x	the components of $\underline{U}$

The Doppler frequency is calculated below for light scattering from a particle with an arbitrary velocity vector $\underline{U}$ and at an observation angle θ, as shown in Fig. 13. The incident wave vector is represented by $\underline{K}_o$ and has a frequency of $\nu_o = \frac{c}{2\pi} |\underline{K}_o|$. A portion of this beam is taken as the reference source so that the reference beam can also be represented by $\underline{K}_o$. The incident beam $\underline{K}_o$ scatters from a light scattering center A, and the cone of light scattering at angle θ to the incident path is collected by the observing lens. This scattered beam is represented by the wave vector $\underline{K}_s$.

The incident beam is moving relative to the scattering particle so that the frequency of the light striking the moving particle experiences a Doppler shift, hence $\nu_{particle} = \nu_o - \frac{1}{2\pi} (\underline{K}_o \cdot \underline{U})$. The frequency of the light scattering from the moving particle also experiences a Doppler shift, hence its frequency is given by $\nu_s = -[\nu_{particle} - \frac{1}{2\pi} \underline{K}_s \cdot \underline{U}]$, where the minus sign arises from the 180 degree phase shift experienced after an external reflection. The above equation can be simplified to:

$$\nu_s = \nu_o + \frac{1}{2\pi} [\underline{K}_o - \underline{K}_s) \cdot \underline{U} \qquad (1)$$

and is the frequency of the signal collected by the observing lens. When the waves of the signal and the reference beams are superimposed they produce a beat frequency equal to the difference in the frequencies of the two interferring waves. The Doppler beat frequency is then:

$$\nu_{Doppler} = \frac{1}{2\pi} (\underline{K}_o - \underline{K}_s) \cdot \underline{U} \qquad (2)$$

Substituting the components of $\underline{K}_o$, $\underline{K}_s$ and $\underline{U}$ into Eq. (2) and simplifing terms, one obtains;

$$\nu_{Doppler} = \frac{c}{\lambda} (U_z \cdot \sin\theta + U_x(1 + \cos\theta))$$

where lambda and theta are taken to be in the fluid.

2. Signal Contrast

If the wavefront were not strictly planar an iris diaphragm would be needed to restrict the interference pattern to a single fringe. When the focus of the second lens of the spatial filter is not exactly at the pinhole, the beam either diverges or converges. The resulting signal wavefront is then spherical. Interference with the reference planar wavefront of the beam will now give a series of concentric annular fringes much like Newton's rings. When viewing several of these fringes, the current over the phototube will remain fairly constant since the Doppler beat would merely alternate the location the light and dark zones. Hence viewing of only one fringe is necessary for a good signal to noise ratio (sharp intensity contrast). This required aperture for a single fringe for a given beam divergence is shown in Fig. 14.

In order to produce a fringe the bright region of the fringe must be $\lambda/2$ out of phase with the dark region. When the focus of the second lens of the spatial filter is too close to the pinhole, the beam diverges. This divergent wavefront is spherical so the location of the first fringe can be calculated. In Fig. 14 the location of the first fringe, S, at the iris diaphragm of the phototube is calculated. To

Symbols:
A - Source of spherical wavefront
B - Wavefront at distance R from its source
C - Screen placed at distance R from the source
D - Distance from D to F is the distance over which the divergence of the signal beam is measured after it leaves the spatial filter.
E - The radius of the signal beam as it leaves the spatial filter (see Fig. 6A,K).

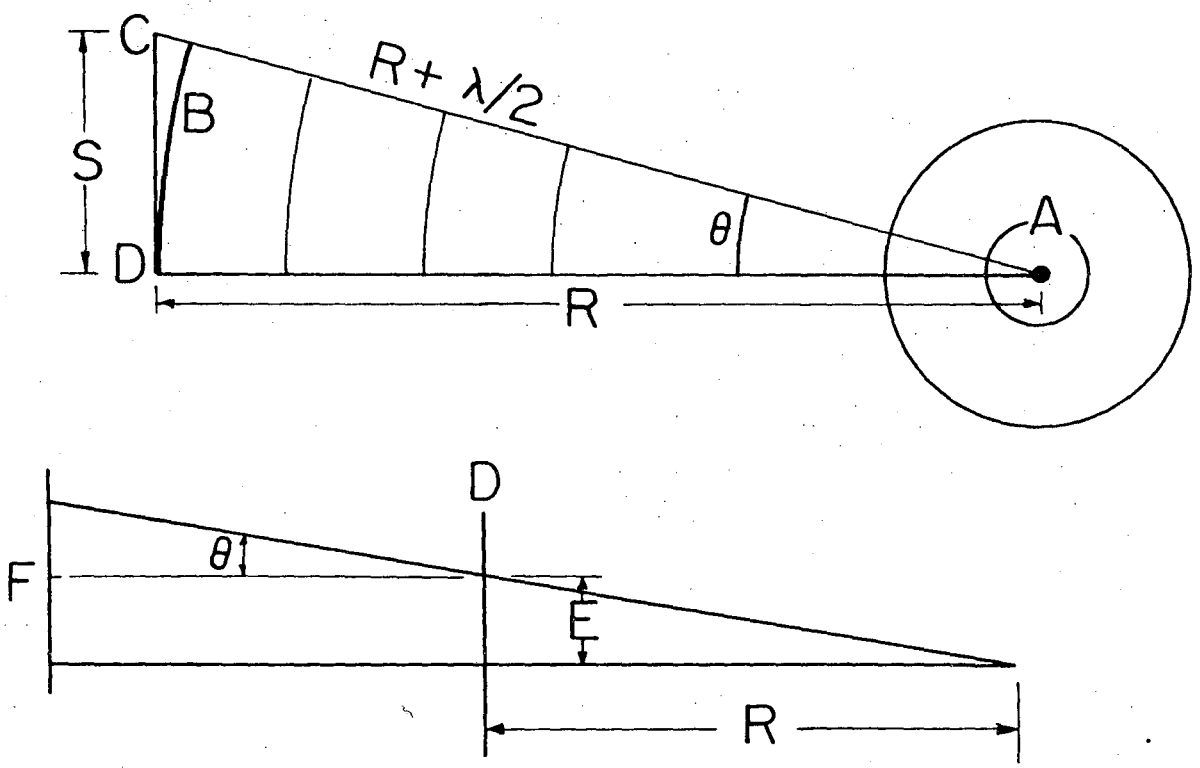

Experimental Determination of R

XBL 768-7431

Fig. 14. Location of the first fringe for a spherical wavefront (upper figure). The experimental determination of R (lower figure). When two waves are out of phase by half a wavelength, and a planar wavefront is brought to interfer with these two waves at a screen C, one wave will appear dark, while the other bright (constructive interference). In the figure the first fringe will appear at the distance S on the screen C. R is experimentally determined by measuring the divergence of the signal beam θ and extrapolating a line back from the spatial filter D, until it intersects the axis of the lens of the spatial filter.

obtain S as a function of R one must first rewrite θ as a function of R, hence:

$$\cos\theta = \frac{R}{R+\lambda/2} = \frac{1}{1+x}$$

where

$$x = \frac{\lambda}{2R} \ll 0$$

and since $x \ll 0$, then $\tan\theta = \sin\theta = \sqrt{1 - \cos^2\theta}$. Substituting for $\cos\theta = f(x)$, simplifying terms and taking the limit as $x \to 0$, one obtains $\tan\theta = \sqrt{2x}$, and examining triangle ACD of Fig. 14, one finds that $S = R \tan\theta$ or $S = \sqrt{\lambda R}$. For the present velocimeter R = 10 m, λ = 6328Å and so S = 2.5 cm.

The expanded reference beam diameter divergence is smaller than value of S. This value of S is larger than the maximum iris setting, hence the iris is used only to prevent excessive intensities from saturating the phototube.

It should be noted that the flatness of the cathode is not a necessary condition for good signal contrast. There is zero contrast when half the phototube is lit and the other half is darkened. Beats then merely alternate the location of the light and dark zones of the fringe pattern. If one compares the distance traveled by the Doppler beat envelope in a quarter cycle (for a 10 KHz beat, a quartercycle, it is .025 millisecond) to the wave velocity (10^{10} cm/sec), the surface roughness needed for a fringe is $(\frac{\lambda_{Doppler}}{4})(10^{10}$ cm/sec) = 2.5×10^{5} cm (4×10^{9} cycles/beat envelope). Hence the few millimeters of height variation on the photocathode can hardly have any effect.

3. Reference Beam Sources

i) Glass plate. From Fig. 16, a graph[43] of contrast ratio versus optical path difference for a 7 mW Jodon laser, one can see that a minimum acceptable contrast ratio of 0.8 corresponds to an optical path difference of 12.5 cm (the coherence length). The corresponding optical path difference for our 15 mW laser is longer than 12.5 cm because the coherence length is mildly dependent on the cavity length. The 7 mW laser (mode spacing C/2L = 260 MHz) had a cavity spacing of approximately 20 in., while our 15 mW laser (C/2L = 190 MHz) had a cavity spacing of about 30 in.

To avoid long path differences between the incident and signal beams, it would have been best to place the reference beam source just before the focusing lens. With the lens effective focal length of only 50 mm, the optical path difference between incident and signal would then be only 10.0 cm. The locating of a reference source here would also have reduced the number of components to align and eliminated the constructing of a path compensator module necessary to correct for large path differences.

Many users of reference mode devices have used particle with diameters less than the wavelength of the laser. In this case the E field of the light surrounds the particle, and for a dielectric particle, dipole radiation radiation is emitted (see Fig. 15). This is Rayleigh-Gans scattering, giving nearly equal back and forward scatter intensities.

0 0 0 0 4 6 0 8 0 6 4

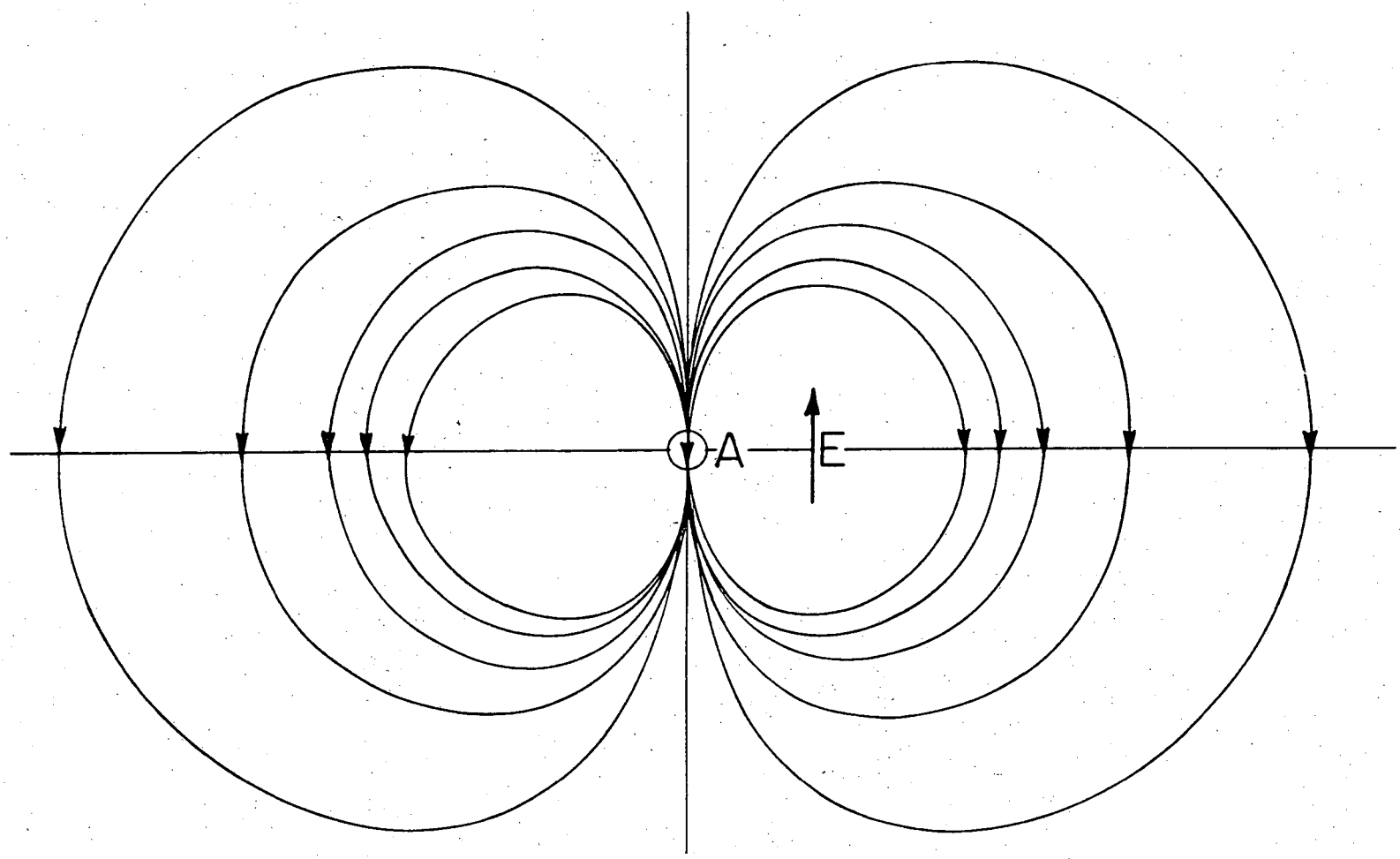

XBL 768-7432

Fig. 15. When the incident wavelength is much larger than the radius of the dielectric sphere, the light scattering from the particle is dipole radiation resulting from a dipole moment induced by the sinusoidally varying E field of the incident light. T is called Rayleigh-Gans scattering. (The particle shown in the Fig. A, is drawn much larger than in actual scale to E or to the lines of constant field.

A reference source which met the above requirements was a plate of glass with appropriate optical coatings, placed just before the illuminating beams enter the observing lens. Because scattering intensities proved to be much less than originally thought the use of a glass plate to generate the reference beam was not possible. A glass plate serving as the reference beam source would have been feasible only if the signal were at least .25% of the incident intensity and preferibly higher (1%). For signal intensities to 1% of the incident intensity, the front of the glass plate could have been coated with an antireflective MgF_2 coating (1% reflectance at normal incidence) and the back side could have been coated with a multiple dielectric coat to give a .25%[56] reflectance. If the signal were only .25% of the incident intensity both sides could have been coated with the .25% reflectivity coating. But below that level of intensity, no coats were found to match such signal intensities. A high reference to signal beam intensity ratio would have greatly decreased the SNR.

At the focal point of our velocimeter, the beam radius was 20 microns. Light scattering from a 2.02 micron diameter particle could have been .25% of the incident intensity only if the particle behaved as if it were a perfectly reflecting flat front surface mirror. But reflectivities were much less.[83] Larger particles which reflect more light were not feasible since the 2.02 micron latex particles already exhibited a slight tendency to settle, and larger particles would settle even more rapidly. Hence such settling particles could not have been used to reproduce the motion of the fluid. But for operation in

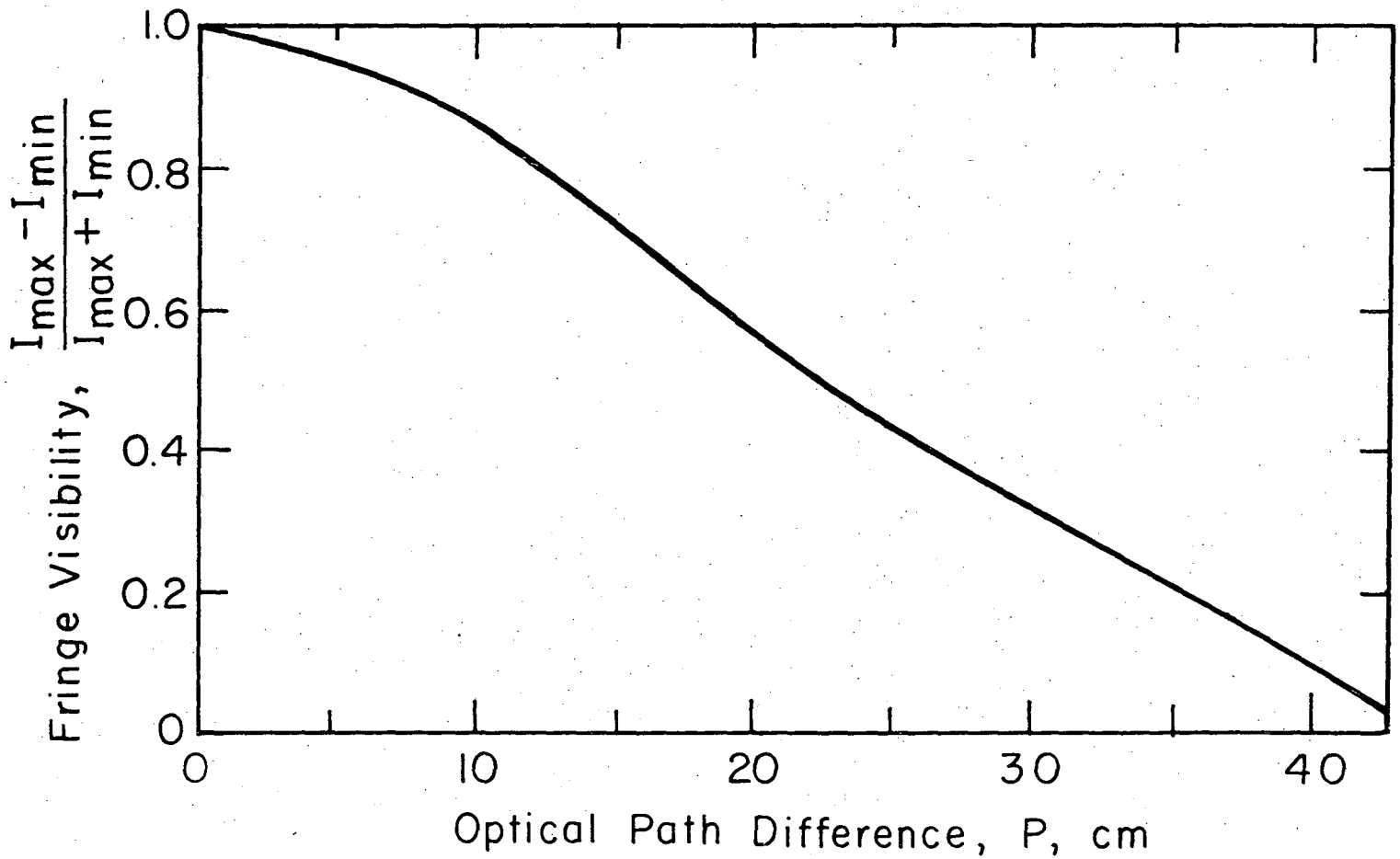

XBL 768-7433

Fig. 16. Effect of optical path difference on the fringe visibility for a 7 mW He-Ne laser. The coherence length is usually taken at a high value of fringe visibility (i.e. 0.8) just before the slope of the curve begins to more sharply decline.

Fig. 17A & B. Scattering intensity diagram[81] for nonabsorbing spheres scattering by geometric and diffraction mechanisms.

For latex spheres in water the ratio of refractive indices x, is 1.33.

A - scattering diagram for .4 micron spheres ($m=r_p 2\pi/\lambda=2$)

B - scattering diagram for 1. micron spheres ($m=5$)

In comparing Figs. A to B one can see that a change in the ratio of the radii of 2.5 results in a change of two orders in magnitude in the scattering intensity for forward scatter. For scattering by dielectric spheres, the backscatter intensity is very small, for $m=2$, $i_2=1.6$, while for $m=5$, $i_2=.044$. i_2 is the intensity function of the light oscillating normal to the incident axis and in the plane of the page. i_1 is the intensity function of the light oscillating normal to the incident axis (A), and normal to the plane of the page.

Note: i_1 and i_2 are also available in tabulated form[83]. The power scattered by spheres in a volume is given by P:

$$P = \frac{\lambda^2 i(x,m,\theta)}{4\pi^2} \Omega_s P_d N_d$$

where

$$x = r_p 2\pi/\lambda$$

P_d is the incident power of the laser = $P_{laser}/(\pi r^2)$

r is the radius of the laser beam

N_d is the number of scattering particles in the volume

λ is wavelength of the incident light

θ is the direction of the scattering

Ω_s is the solid angle of observation

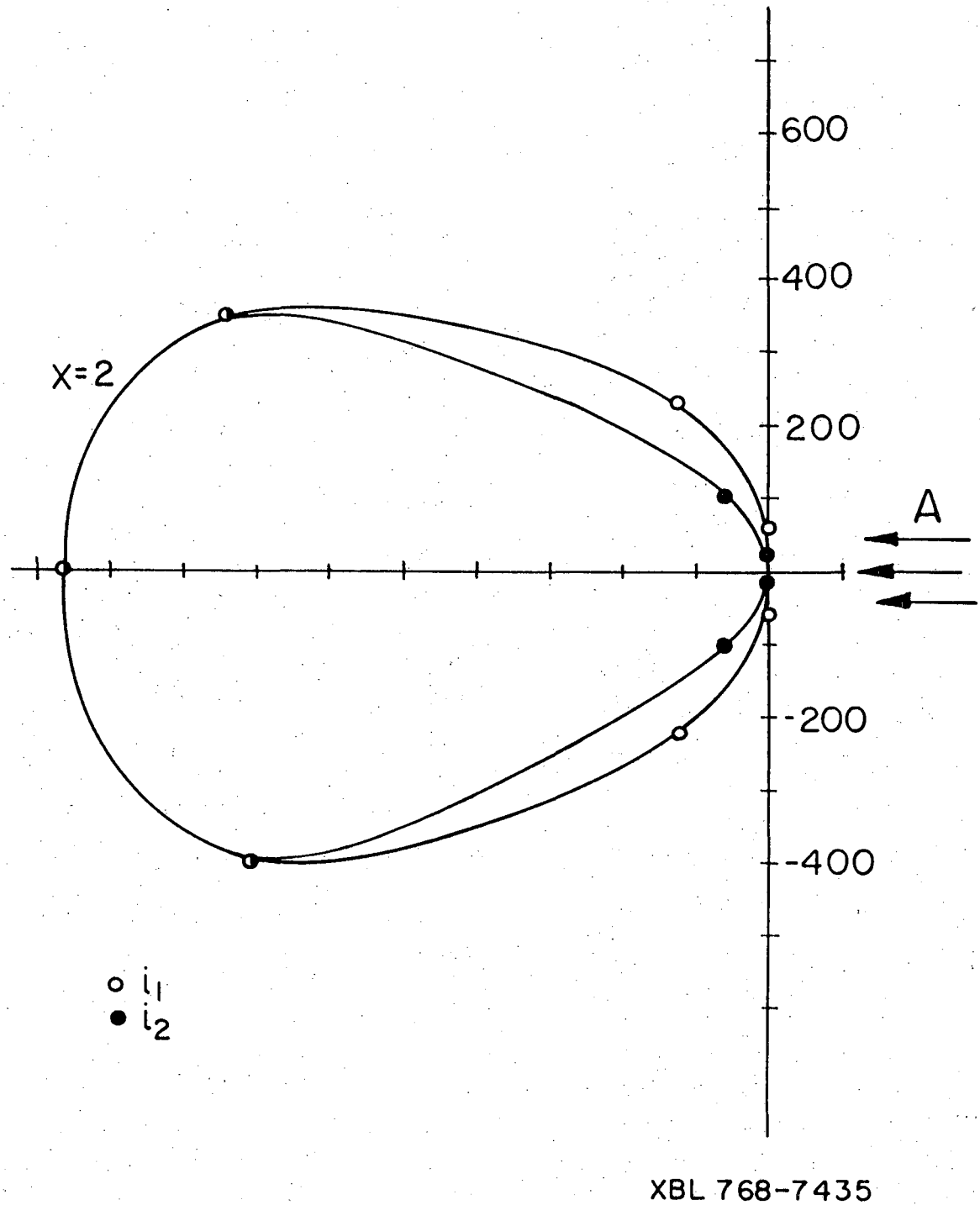

Fig. 17 A

the differential mode, particles with diameters greater than the laser wavelength are necessary to get acceptable SNR's (see next section). Such particles do not scatter by the dipole mechanism but rather by geometric and diffraction scattering or by an intermediate mechanism. These scattering regimes give much lower backscatter than forward scatter intensities. (Fig. 17)

ii) Path compensation. The laser light is usually associated with excellent monochromaticity and an exceptional coherence length (meters). Therefore it would not have been necessary to compensate path lengths. One could then place a beam expander and neutral density filter at N in Fig. 6 as the reference source. But holographic[57] work has however shown that the very coherence length very short (centimeters). (Fig. 16) This length can be extended to meters. But it would require the filtering of parasitic frequencies near 6328Å with either a Michelson interferometric filter or a Fabry-Perot Etalon installed in the laser at an intercavity location. These devices prevent by destructive interference the lasing of parasitic frequencies thus allowing greater amplification of an extremely narrow band. (This implies that a filter can also be placed outside but with large power losses.)

Low power lasers are not equipped with intercavity access. The lowest power HeNe laser found with an intercavity experimental chamber is Jodon's 50 mW laser. But Lasers of such power are not only more costly but also much more of a health hazard. Even with an intercavity chamber etalons and interferometers are very sensitive to temperature variations and mechanical vibrations. With neither the

Fig. 19. The coherence length (monochromaticity) of a laser can be increased by placing a Michelson interferometer filter in the laser cavity. Parasitic frequencies near the main lasing frequency of the laser cavity can also lase. These frequencies like the main frequency are also amplified with each pass through the plasma tube. As a result the gain of the main frequency is reduced. Since the output of various frequencies are coaxial, the fringes of the parasitic frequencies randomly overlap onto the interference pattern of the main frequency and thus decrease fringe visibility by increasing the background radiation.

When the Michelson interferometer is placed in the laser cavity and adjusted to create a bright central spot pattern for only the main frequency, the parasitic frequencies can never build up in the laser cavity. The Michelson interferometer consists of two semitransparent and two opaque mirrors. A portion of the intercavity beam B, travels through both of the semitransparent mirrors E, while another portion travels through an extrapath length C, before it is reunited with the beam B at location D. By adjusting the path length of C, frequencies near the main frequency will be out of phase with those of beam B, hence the parasitic frequencies destructively interfer at D. At the main frequency the beams reunite in phase at D, and hence they are unattenuated (constructively interfer). The main frequency passes back and forth between the cavity mirrors (E and F), and is now the only frequency having a very high gain (there are also no competing frequencies) through amplification by stimulted emission of the excited atoms in the plasma tube A. With the filter in place, the parasitic frequencies which are amplified in the plasma tube are extinguished (destructive interference) in the interferometer, so that there is no net gain for these frequencies.

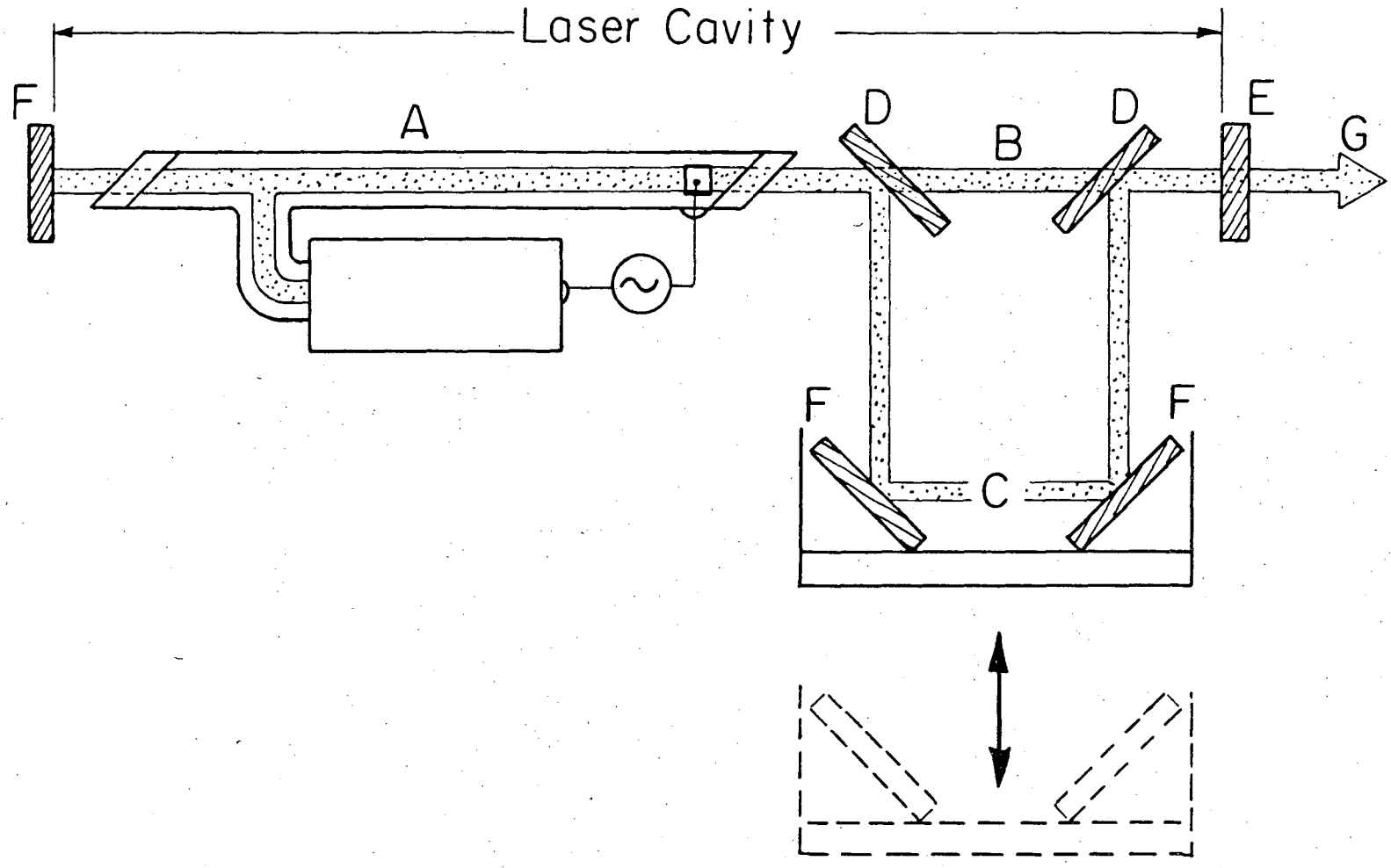

XBL 768-7437

Fig. 19.

simple glass plate nor the extended coherence length possible it was necessary to install a path compensators.

Our earlier reluctance to installing the compensator stemmed not only from the long path correction (63.44) but also from the increase in the density of components, mainly mirrors. Because of the long path and the small space available on the velocimeter platform, six mirrors with appropriate tilt platforms as shown in Fig. 46 were used. (refer to Fig. 1 for location of compensator) Alignment was no problem, but mirror distortions were compounded by the large number of reflections. There are two factors assumed to contribute to the size of the reference mode probe volume. These are the spatial filter, and the intensity variation of the focal zone.

4. The Probe Volume:

Even for a perfectly corrected lens light still cannot be focused into a infinitely small focal point as expected in geometrical optics. Instead one obtains a diffraction limited diameter called the Airy disk. This also implies a certain beam waist profile in the focal zone which varies from linearity. Since the author has used $I/I_o = 1/e^2$ as the edges of the Gaussian laser beam, the same limits should be used to determine the edge of the focal zone. This zone should be where the ratio of the beam edge intensity I, z_o the beam axis intensity, I_o is $1/e^2$. In a study of laser beam focal waists by perturbations on a applied electrical field[58] the focal region showed a parabolic profile as given below:

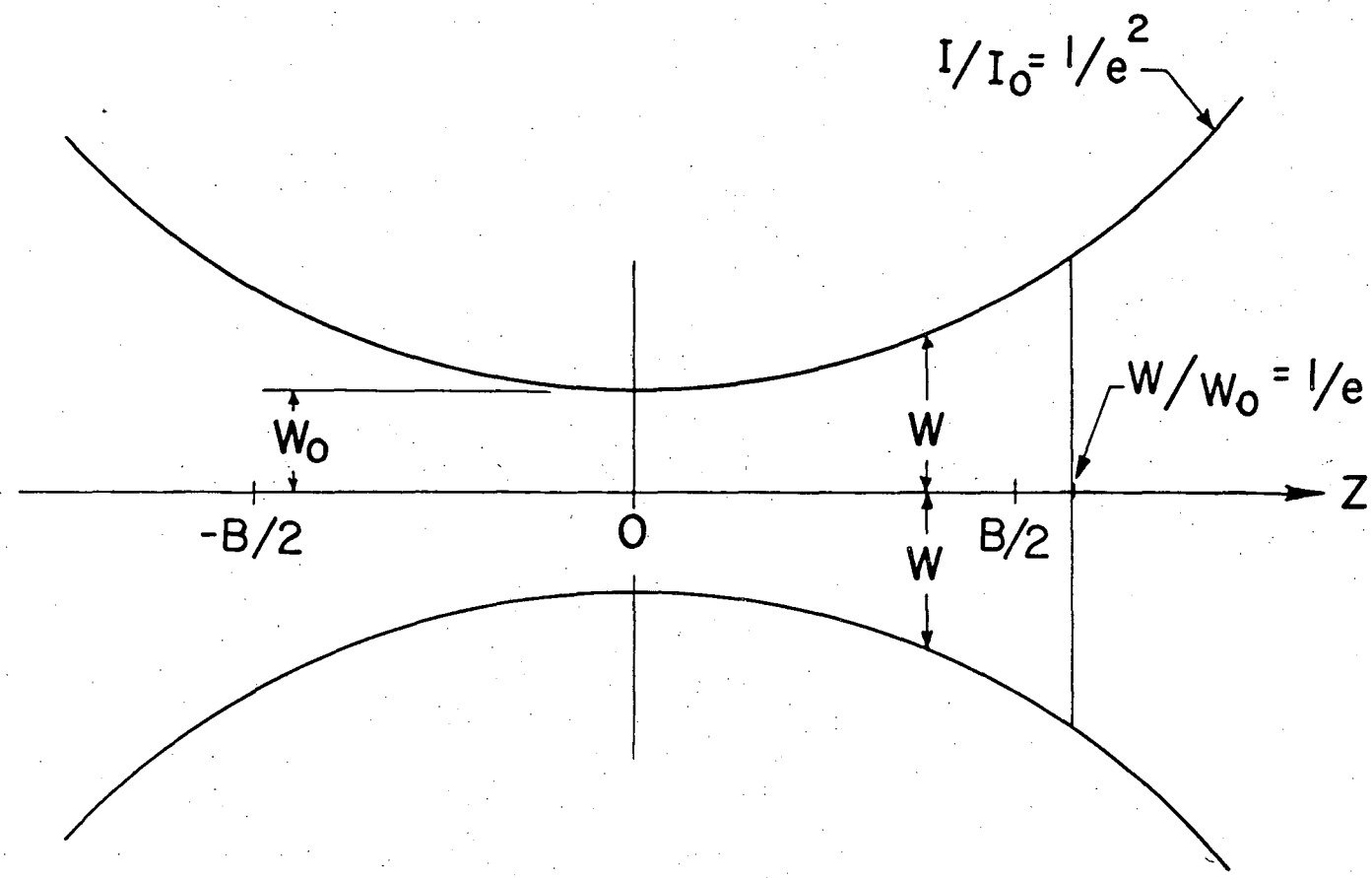

XBL 768-7438

Fig. 20. Reference mode probe volume. Experimental[58] measurements have shown that the focal region of a Gaussian laser beam has a parabolic profile. At B/2 the intensity of the beam along the z axis decreases by $\sqrt{2}$. W is the edge of the Gaussian beam. The intensity at W is $1/e^2$ less than the intensity at the z axis.

For the variables as given in Fig. 20

$$b = (4f_1^2)/(k^w w_1^2) \tag{9}$$

and

$$w_o = (b/k^w)^{1/2} \quad \text{(radius of Airy disk)} \tag{10}$$

Thus the Gaussian envelope of the focused beam (where the intensity at the z-axis is $1/e^2$ larger than at radius w) is given by

$$w = w_o(1 + (2z/b)^2) \tag{11}$$

For the velocimeter, b = 1.39 mm, w_o = 10.8 microns and w_1 = .85 mm. So in order for the intensity along the the $\hat{z}$ to decrease by $1/e^2$ from the focal point (w_o), w_o/w must be 1/e (the area has expanded by $(w_o/w)^2$). Thus for the velocimeter location along the z axis where $w_o/w = 1/e$ occurs at z = .9 mm. The author assumed that signal originating < 0.9 mm would be about an order of magnitude brighter than signals from outside the region, so that signal from z > 0.9 mm would be buried under the stronger signals.

The value of b/2 (where the intensity along the z-axis falls by a factor of 4) is fairly large and a smaller value would be necessary for high spatial resolution. From Eqs. (9) and (10) one can see that expansion of the beam diameter would not only decrease the beam waist but that the intensity would decrease more rapidly as one moved away from the focal point (smaller b). Improvement in spatial resolution, z, is proportional to w_1^2, $z = w_1^2 (k^w/f_1) \sqrt{(w/w_o)-1}$.

In Fig. 33, the beamsplitter module, one can see that a beam expander could be easily fitted into the hole (E) provided in the rotating mount to allow for operation in the reference mode. But beam

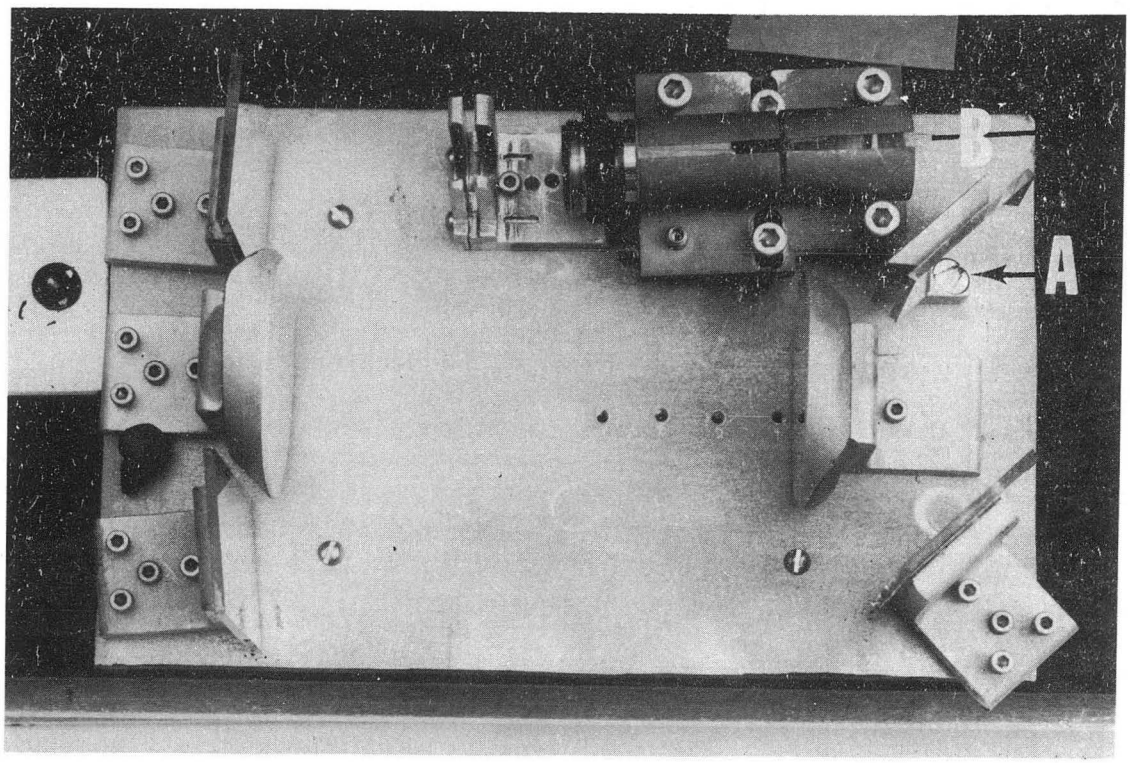

CBB 768-7315

Fig. 46. Path compensator. The reference beam produced at the glass plate N of Fig. 6A, enters the path compensator at A. The beam is reflected through a series of six first surface mirrors (flat to $\lambda/10$), passes through a neutral density filter and through a beam expander. The beam exists at point B and returns to the glass Plate N'. The overall path traveled by the beam is 60.5 cm.

expansion poses another problem.

At present the five hole mask (mirror D of Fig. 6) must be slightly off 45° so that the center of the light cone from the returning signal does not exit through the central hole. If it did, about 4% of this light resulting from a glass interface reflection would finally enter the phototube. But this signal also suffers from low backscattering and the small opening of the iris. Beam expansion would increase the hole size in the mask and thus make it unlikely that light be reflected from an area at the edge of the hole, and into the spatial filter (alignment problems).

The other determining factor of the probe volume is the spatial filter. As Fig. 21 shows, a certain aperture size R will restrict the distance away form the focal plane where light can be gathered. The region resulting from the aperture is a biconical solid (see Appendix I).

$$R = \left(\frac{f'd}{f^2}\right) \Delta f = .03\ \Delta f \qquad (12)$$

At present, a 50 micron diameter aperture will give the flow channel a $\Delta f = .23$ mm. Since $\Delta f < b$, Δf determines the size of the probe volumes. This would give an uncertainty range equal to the thickness of the boundary layer phenomena.

To reduce the spatial filter such that $\Delta f = 60$ microns would have required a 2 micron pinhole which is only a theoretical value, since this is less than the Airy disk of lenses involved and would block most of the signal. Alignment and stability problems would be very difficult.

Fig. 21. Axial dimension of reference mode probe volume as determined by the spatial filter, Δf

Symbols:

d	Radius of focusing lens
f	Focal length of focusing lens
f'	Focal length of first lens of spatial filter
h	Distance between the axis of the focusing lens at the focal plane to the location of the ray emanating from a distance of $f+\Delta f$ along the focusing lens axis
H	Radius of spatial filter lens
L	Distance along the lens axis where the ray mentioned in h intersects the lens axis while in the spatial filter
P_o	Distance between focusing and spatial filter lenses
θ_1	$\tan\theta_1 = d/f$
R	Radius of pinhole
$\phi_{c,d}$	Angle of slope of the ray described in h
ω	Slope of ray described in h as it is focused by the spatial filter lens

0 0 1 0 4 6 0 8 0 6 9

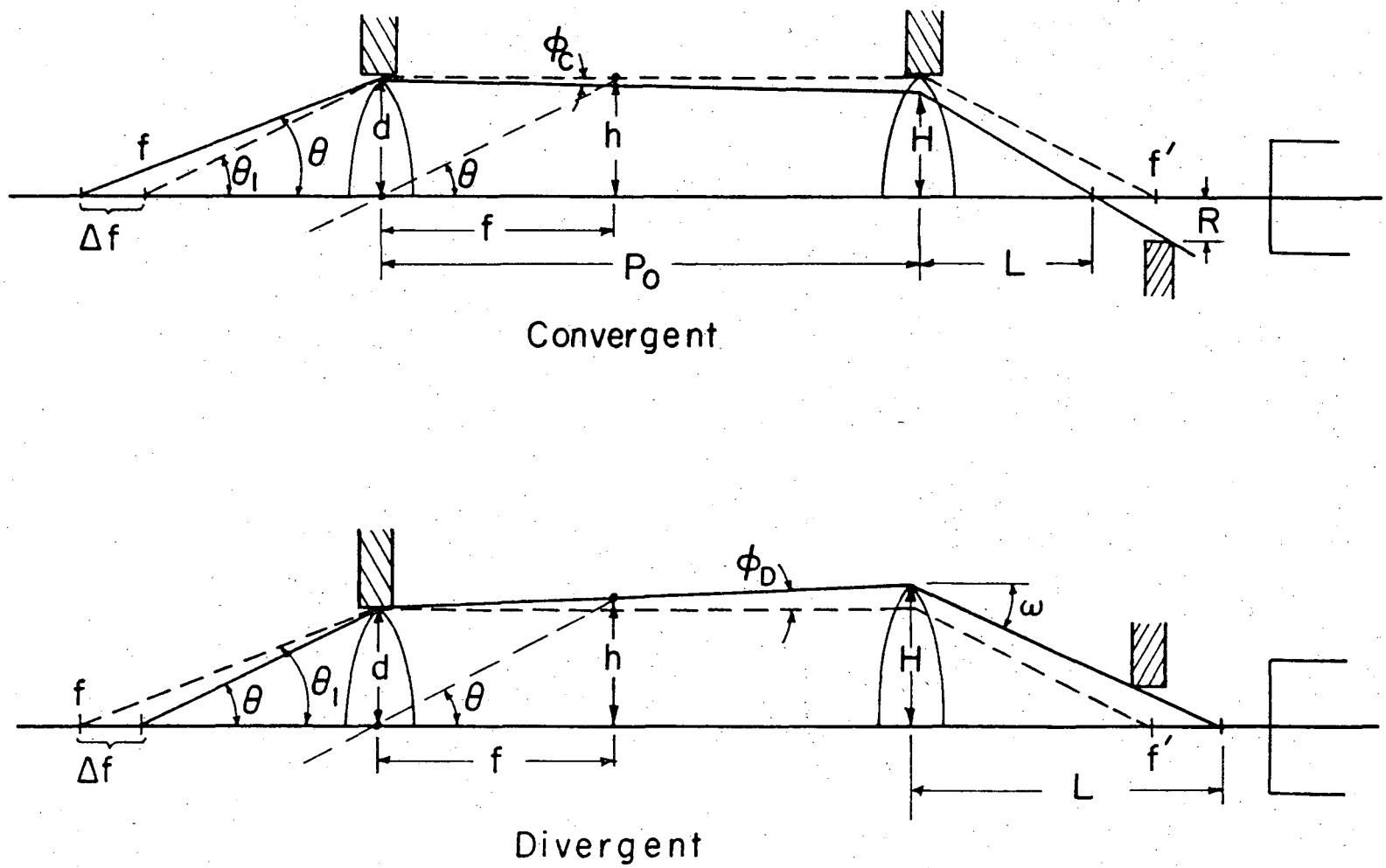

XBL 768-7439

Fig. 21.

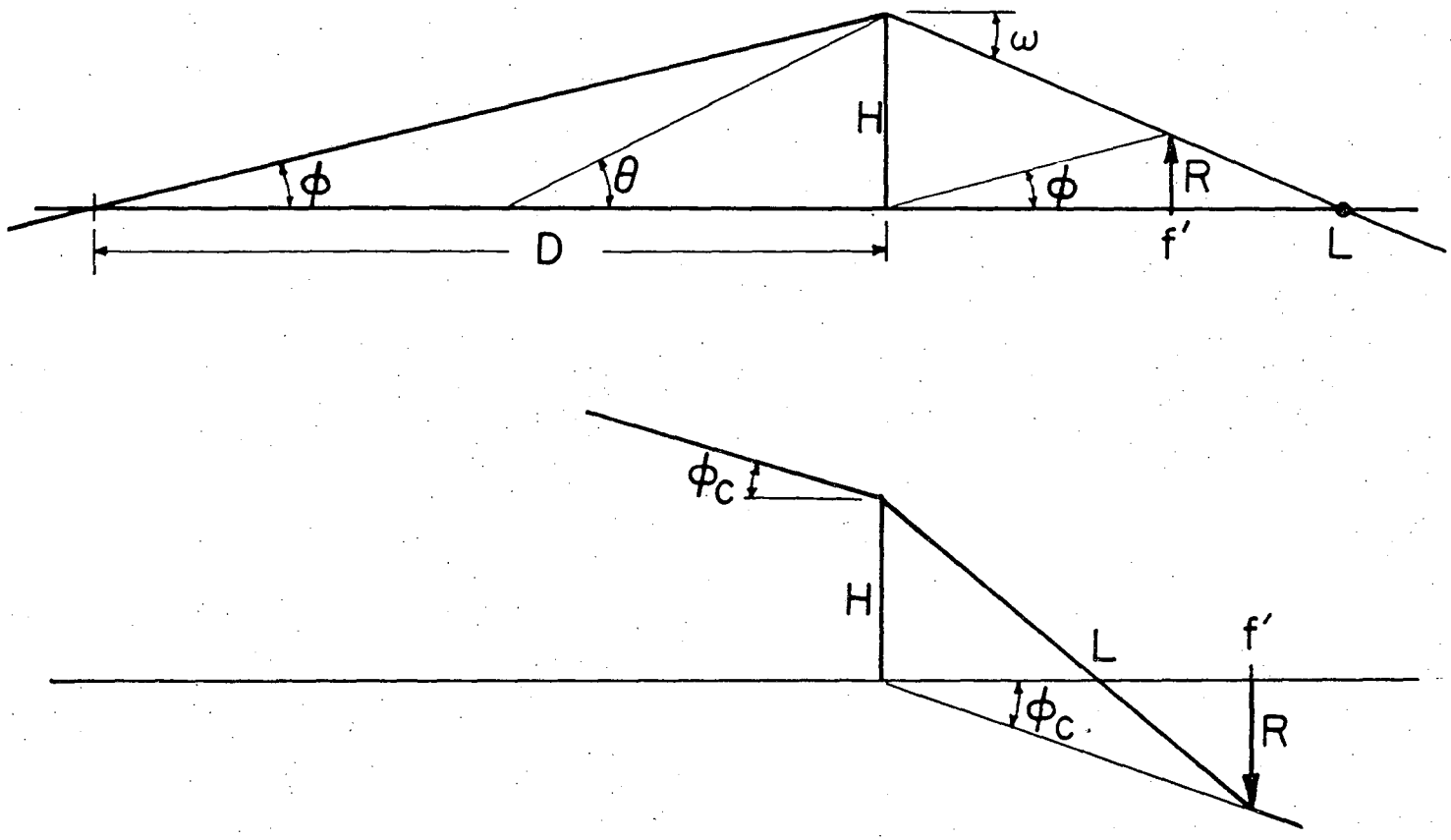

XBL 768-7440

Fig. 21 (Cont'd).

0 0 3 0 4 6 0 8 0 7 0

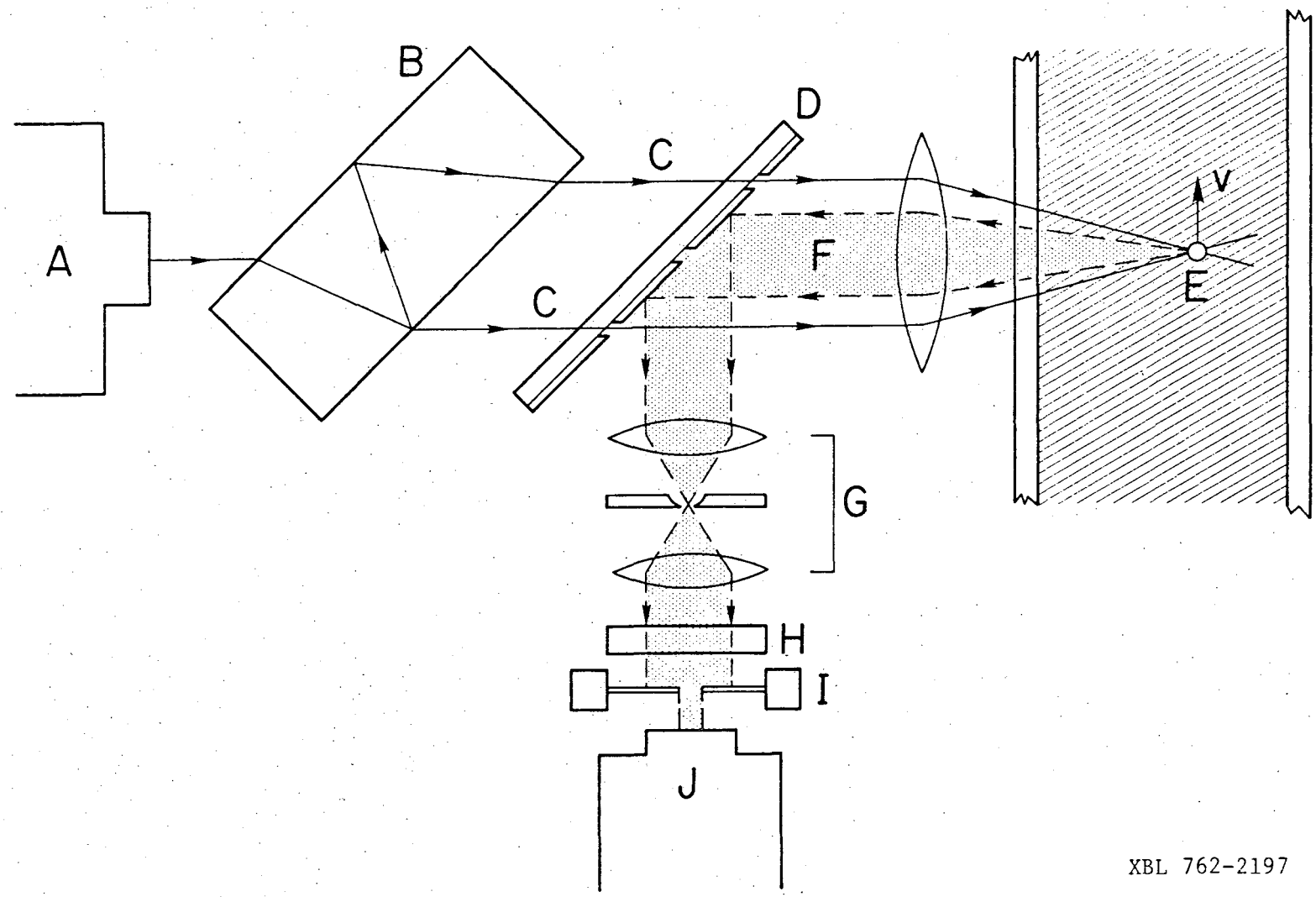

Fig. 22. Simplified scheme of the differential mode. The velocity component perpendicular to the axis of the focusing lens and in the plane of the illuminating beams is measured in the differential mode.

B. Differential Mode

1. Theory

A simplified representation of the optics is shown in Fig. 22. Laser light is split into two equal intensity beams of a known separation. The beams are brought to focus inside the same flow channel as used in the reference mode. At the focus the beams intersect and form an interference fringe pattern.[60] Varying scatter intensities of particles traversing this light and dark pattern will then give an intensity modulation, whose frequency is linearly proportional to the particle's velocity. This signal returns through the observing lens, reflects from mirror D into the spatial filter and finally enters the phototube. A similar analysis[59] using physical optics gives the same resulting Doppler frequency. The geometry of the differential mode, and a mathematical representation of the system by wave vectors are shown in Fig. 23.

The differential mode consists of two signal beams, one produced from each of the two incident beams scattering from a particle. The frequency of each of the signals is derived in the manner of Eq. (1). The frequency of the signal beam arising from the scattering of beam 1 is then:

$$\nu_{1s} = \nu_o + \frac{1}{2\pi}(\underline{K}_1 \cdot \underline{V}) - \frac{1}{2\pi}(\underline{K}_s \cdot \underline{V}) = \nu_o + \frac{1}{2\pi}(\underline{K}_1 - \underline{K}_s) \cdot \underline{V}$$

Similarly the signal beam arising from the scattering of beam 2 is:

$$\nu_{2s} = \nu_o + \frac{1}{2\pi}(\underline{K}_2 \cdot \underline{V}) - \frac{1}{2\pi}(\underline{K}_s \cdot \underline{V}) = \nu_o + \frac{1}{2\pi}(\underline{K}_2 - \underline{K}_s) \cdot \underline{V}$$

Fig. 23. Analysis of the differential mode

A	beamsplitter
B	mirror
C	focusing lens
D	phototube
E	moving light scattering particle
$\underline{K}_1$	wavevector of the incident beam 1
$\underline{K}_2$	wavevector of incident beam 2,
$\underline{K}_s$	wavevector of signal beam
$\underline{V}$	velocity of particle E
V_z	z component of $\underline{V}$
V_x	x component of $\underline{V}$

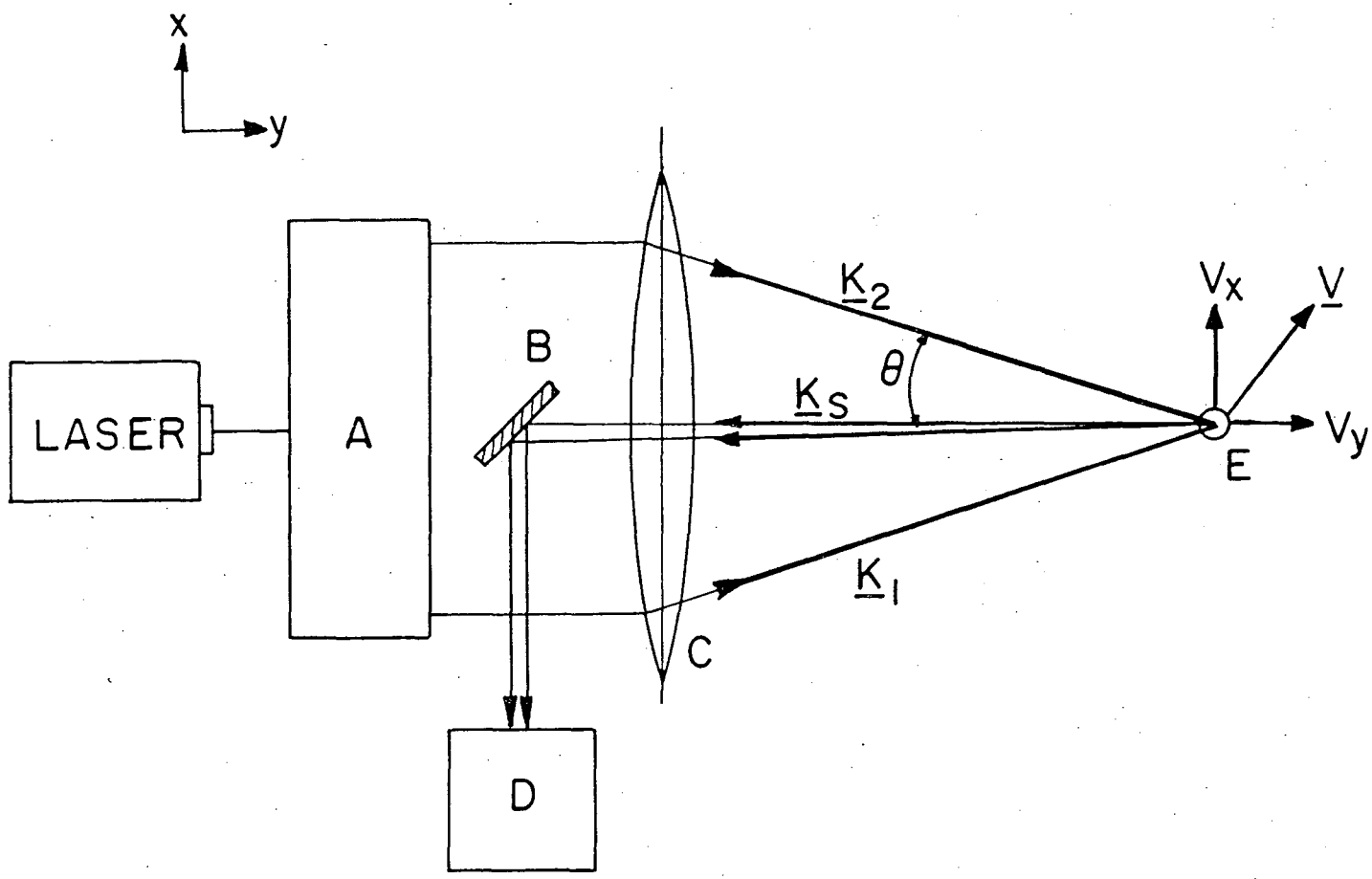

XBL768-7441

Fig. 23.

The superposition of the two signal beams produces the Doppler beat frequency whose frequency is the difference between the two signal beam frequencies. This Doppler beat frequency is:

$$\nu_{Doppler} = \frac{1}{2\pi} (\underline{K}_1 - \underline{K}_2) \cdot \underline{V} \tag{13}$$

Substituting in the components of $\underline{K}_1$, $\underline{K}_2$ and $\underline{V}$ into the above equation simplifying and collecting terms one obtains:

$$\nu_{Doppler} = \frac{2V_x}{\lambda} \sin(\theta/2) \tag{14}$$

Note that this gives one only the x component of the velocity.

From the above section one can see that a measurement in the differential mode has several distinct advantages over that of one in the reference mode. From examining the above equation, the signal is seen to be independent of the viewing angle. Contrast is high since the optical path differences are small because the beams travel as a parallel pair through most of the optical components. And the parallel beams can be rotated by 90 degrees to give a second velocity component. With the differential mode a first approximation of the optimum scatter size and concentration can also be calculated beforehand. Perhaps because of these advantages, the differential mode has had the most innovations and has been analysed more thoroughly.

2. Beamsplitters

In order to operate in the differential mode a source of two parallel equal intensity beams are needed. Since the beams should be spatially and temporally coherent it is preferable to use a single

Fig. 24A. Beamsplitter[42] assembly the output beams B, equidistant from the axis of the incident beam A. The beamsplitter assembly can be rotated by 90 degrees to obtain the velocity component which is perpendicular to U and to the axis of lens E.

Fig. 24B. Output beams B from this beamsplitter[24] are not equidistant to the incident beam A. It cannot be rotated to make measurements on another velocity component.

A laser beam
B location of exiting output beams
C beamsplitter coating giving match transmitted and reflected intensities
D opaque aluminum mirrors
E focusing lens
F probe volume
u velocity component measured by the velocimeter

0 0 1 0 4 6 0 8 0 7 3

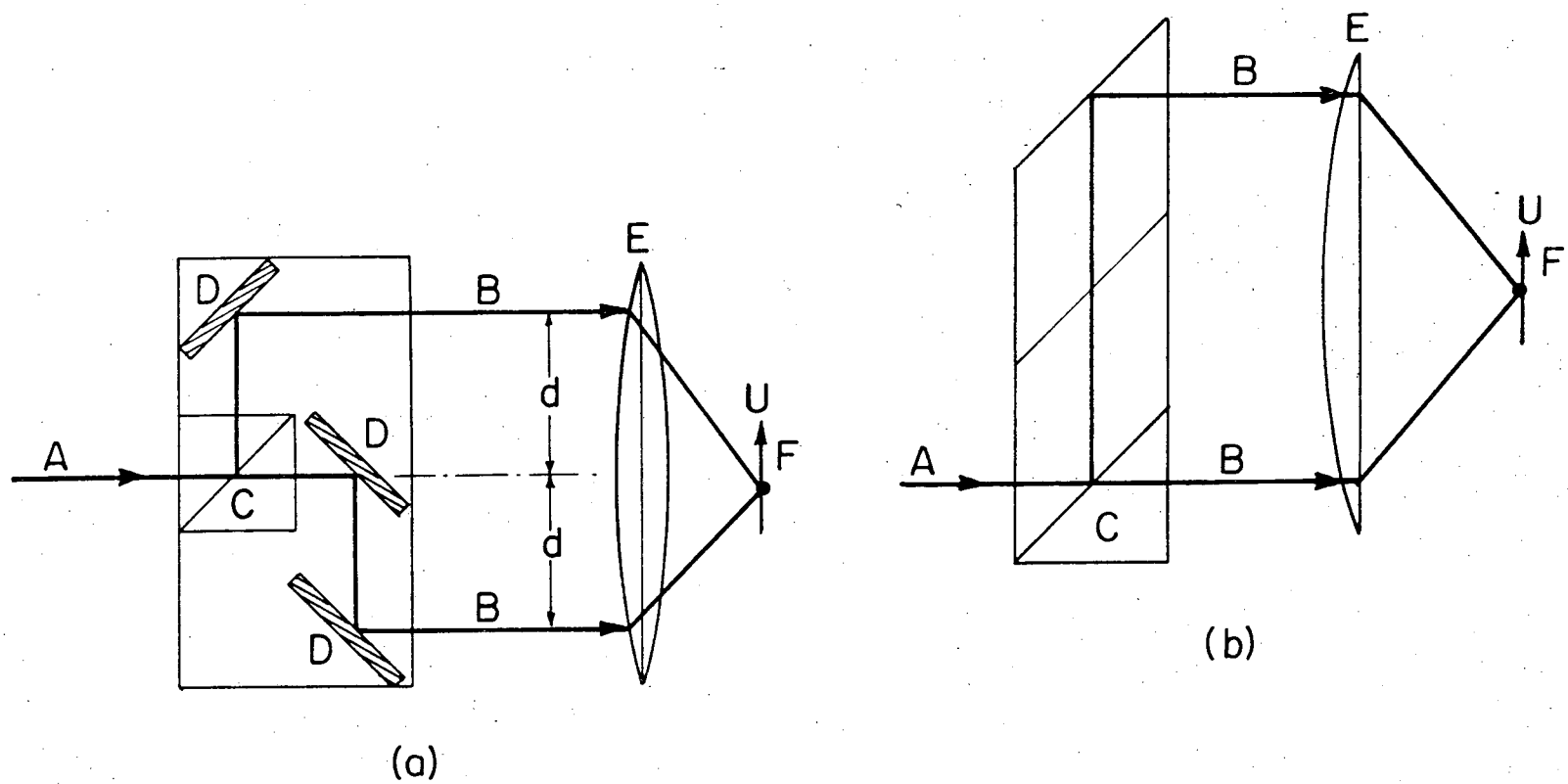

XBL 768-7442

Fig. 24.

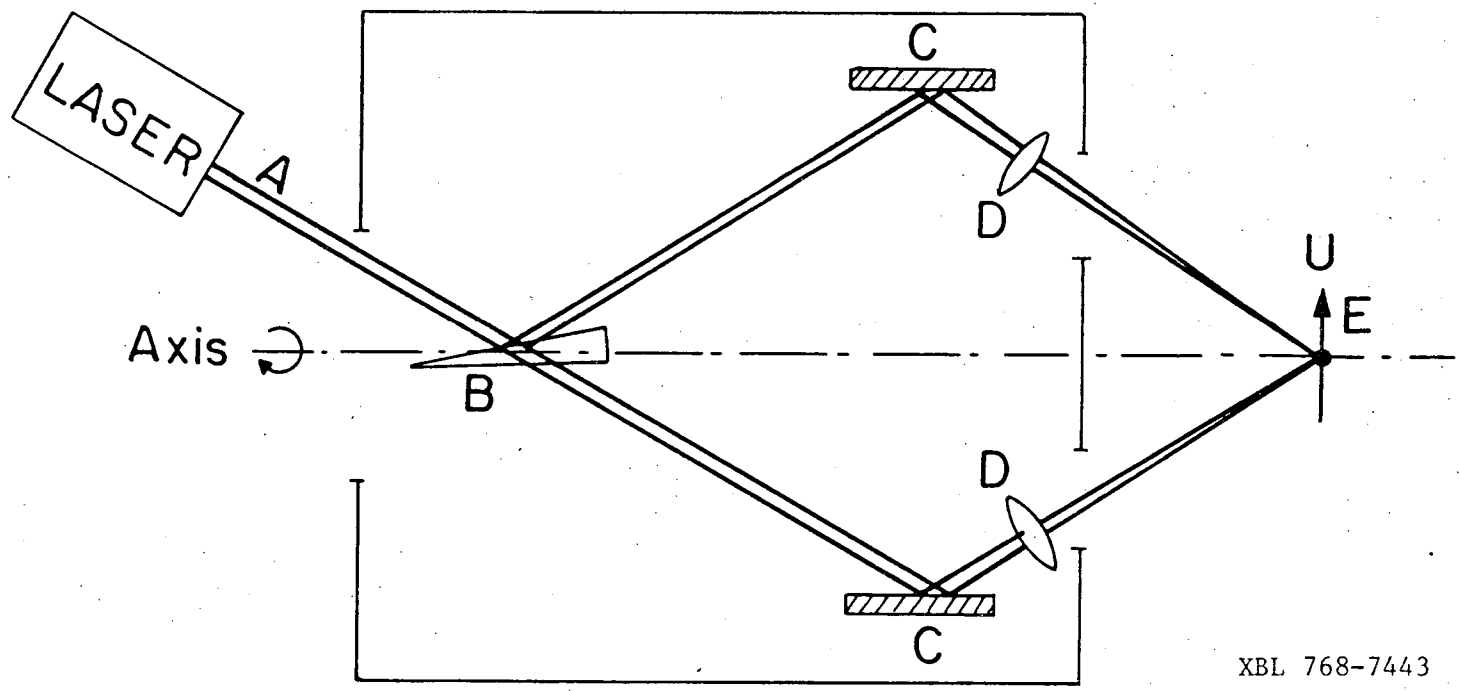

Fig. 25. Beamsplitter with adjustable ratio of beam intensities. The ratio of beam intensities is determined by the angle of incidence at which the source beam (A) strikes the glass wedge (B). The ratio of beam intensities can be calculated from Fresnels equations. The use of separate focusing lenses for each of the output beams ensures that the profile of the focal region is more closely cylindrical than that of two output beams focused by a single lens. But the use of two focusing lenses requires careful aligning to assure that the beams intersect at their focal regions. The beamsplitter assembly is not rotatable.

source and to split the beam. A number of devices for beamsplitting have been used, some geometrically splitting the beam and others splitting the intensity.

These have included various systems of mirrors and standard beam-splitting plates or prisms[42,61,64] and arrays of refracting plates.[12] In order to obtain the three velocity components it is necessary to operate in the reference mode and differential mode. Limited resources prevented the use of a laser with a two colored output and two channel optics. So in order to obtain the two velocity components from operation in the differential mode a rotatable beamsplitter was used. The beamsplitter also had to slide out of the beam's path while operating in the reference mode, yet it would have to return precisely to its original location for future differential measurements. Otherwise the axial symmetry upon rotation would be lost and the accuracy of the probe location reduced.

Mirror systems require precise alignment for parallel beams and accurately positioning for axial symmetry. Mirror mounts usually consist of two snuggly fitting concentric cylinders. The outer cylinder is usually mounted onto a laser with the optics in the inner one. The problems of precise alignment for each mirror and the splitter plate and the need to put this splitter onto a slide mount discouraged the use of such systems.

Parallel plates do not present as severe an alignment problem as the mirror systems, but are very bulky since the amount of splitting per plate is small and the air space is large (see Fig. 26). This is rather unfortunate since the optics are already crowded and such a

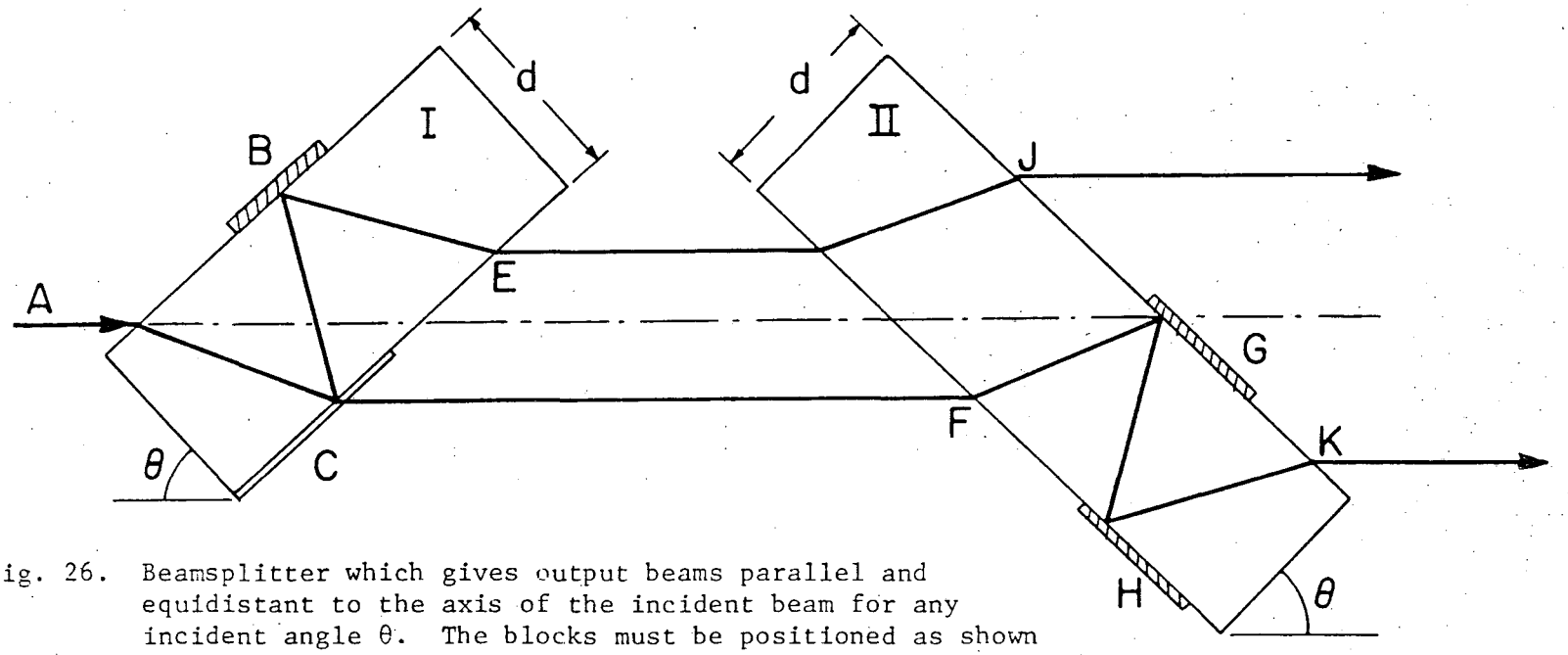

XBL 768-7444

Fig. 26. Beamsplitter which gives output beams parallel and equidistant to the axis of the incident beam for any incident angle θ. The blocks must be positioned as shown in the figure and must also be of the same thickness.

Symbols:
- A incident beam
- B opaque mirror coating on block I
- C semitransparent coating (beamsplitter coating)
- D and I are not shown to avoid confusion with other letters.
- E output beam from block I, and input beam to block II
- F second output beam from block I and input beam to block II
- G and H opaque aluminum mirrors
- d thickness of glass blocks

device would not fit into the available space.

There are two types of beamsplitters which produce beams parallel and axisymmetric to the incident beam, the geometrical splitter and the amplitude splitter.

3. The Geometric (wave) Splitter:[72]

a. Theory and construction. A light beam centered on the axis (Fig. 28) after striking the corner of prism L is physically split into two circular halves. Because the two beams are mirror images, only the path of one of them the upper one shall be calculated. This beam enters the lower half of the cube and is refracted upward through the prism to the opposite wall where it is refracted in the reverse direction. It exits vertically displaced and parallel to the incident direction. The two prisms (I and II) which form the beamsplitter and the path taken by the light beam through them is shown in Fig. 28. In prism I, the beam incident on the lower half of the prism at A, is refracted as it enters the prism. The angle of refraction ϕ, is given by Snells Law:

$$\phi = \sin^{-1}\left(\frac{n_{air}}{n_{glass}}\right)\sin\theta \quad . \tag{15}$$

Since the angles ϕ and γ form a 45 degree angle, then $\gamma = 45° - \phi$. The amount that the beam is displaced by prism I is

$$H = K \cos\theta \cdot \tan\gamma \tag{16}$$

The beam at B now enters prism II. From geometric considerations:

$$L/(F-L) = \tan\gamma, \tag{17}$$

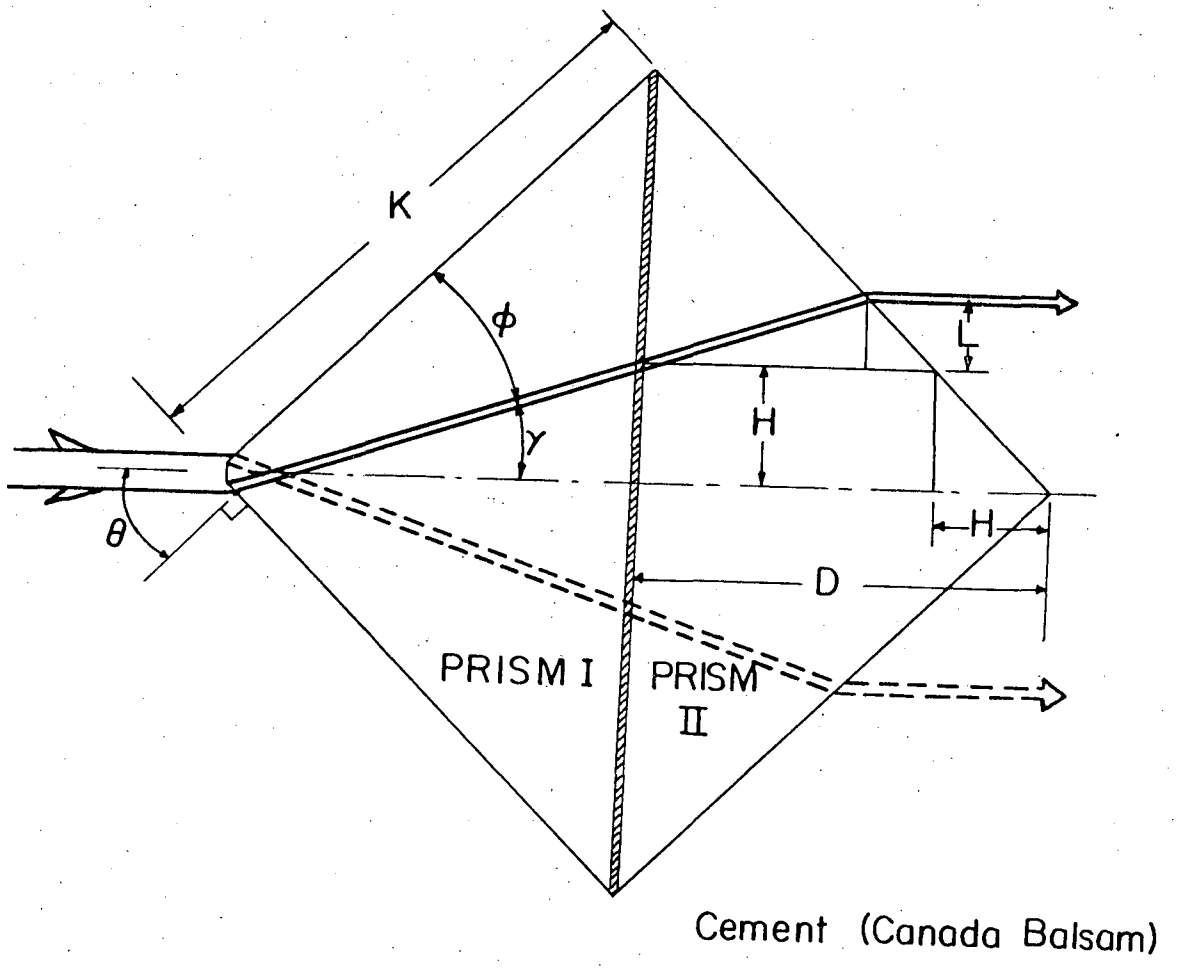

XBL 768-7445

Fig. 28. The geometric beamsplitter assembly consists of two right angle prisms cemented together as shown in the figure. A beam striking the corner of prism I is split into two beams with semicircular crossections. The portion of the beam striking the prism above the corner at A, is deflected upward. When the beams reach walls of prism II, they undergo a reversal in refraction and exit the beamsplitter parallel to the incident axis, but vertically displaced. This beamsplitter can be rotated about the axis of the incident beam in order to rotate the two output beams about the incident axis.

hence the contribution of prism II to the displacement of the output beam is:

$$L = F \tan\gamma/(1 = \tan\gamma) \ . \tag{18}$$

At C the beam undergoes a refraction reversing the effect at A. Since the surface of the cube at C is parallel to the incident surface at A, the beam exits parallel to the direction of the incident beam. The total displacement of each beam is L + H, so that the total separation between the two output beams is:

$$S = 2(L+H) \tag{19}$$

The device when mounted into rotating concentric cylinders and onto a rail assembly (Fig. 27) fulfills its specifications and yet is inexpensive and elegantly simply. It was the first type of beam-splitter tested.

The cube was made from a right angle prism. Commercially available prisms usually had blunt ground edges (e.g. Ealing Inc. prisms had .5 mm wide edges). The blunted edge blocked a major portion of the 1.7 mm diameter laser beam. An acceptable prism with a .12 mm edge width was finally obtained for fabricating the beamsplitter. To minimize external and reflective losses an antireflective (1% reflectance) coat was deposited on the faces. To minimize internal reflective losses, the prism halves were cemented with Canada Balsam whose index of refraction closely matched that of the glass. The effects of ramped edge (Fig. 29) of the prism where one end of the prism is larger than the other but with no effect on the precision of the right angle edge,

Fig. 30. The ramped effect. When all the triangles formed by taking cross sections along the prism are congruent triangles (i.e. triangles ABC, DEF and HIJ are congruent), but the sides of the triangles become smaller as the cross sections are taken from points A to H. This inaccuracy in the polishing of a prism is the ramped effect.

Ramped effect can be partially corrected by cutting the prism at its center (dotted lines) and folding it over as shown. The Cemented prism thus has parallel edges so that a beam K traversing the cube exits at L with only a slight deflection. Compare this with the deflection of beam B' of Fig. 30A.

Beamsplitter made from a ramped effect prism, without the correction of Fig. 30.

0 0 0 0 4 6 0 8 0 7 7

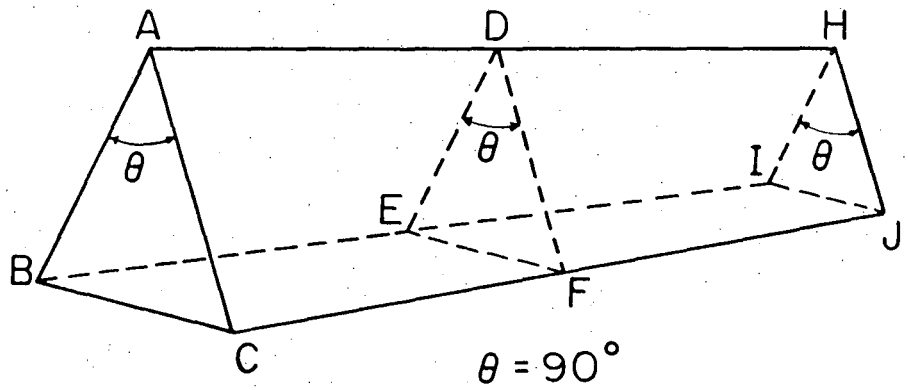

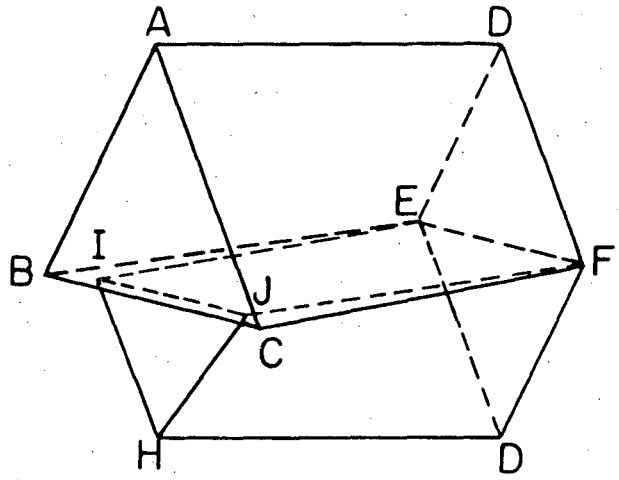

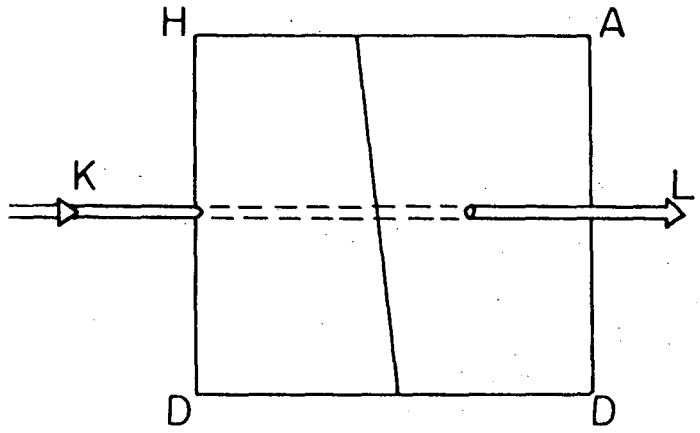

XBL 768-7446

Fig. 30.

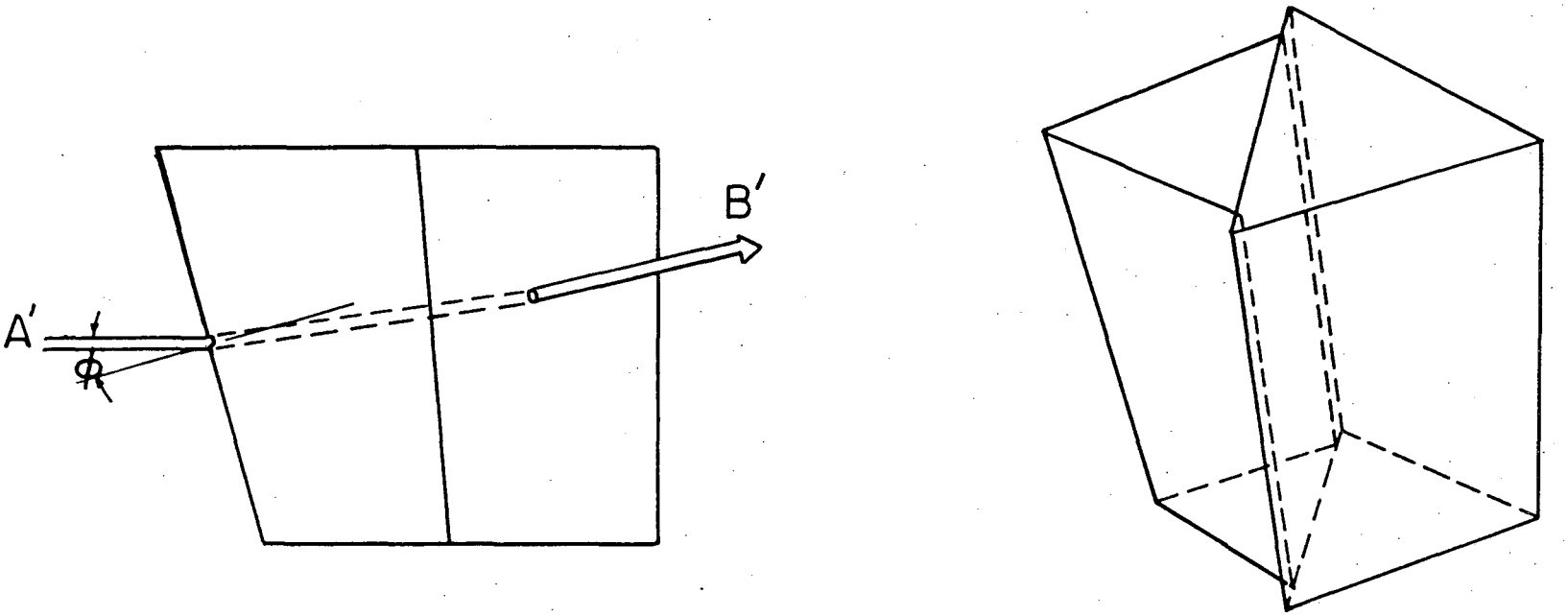

XBL 768-7447

Fig. 30 (Cont'd).

would have bent the output beams so that they were no longer parallel with the incident beam. This ramp effect was partially corrected by cutting a single prism in half and folding it over as shown in Fig. 30.

Alignment of the finished cube and cylindrical housing was done by first marking the projection of the incident beam at 3 meters away and then mounting the cube with a low melting mounting wax. With the splitter mounted and the wax still soft the cube was positioned such that projections of the resulting two beams remained equidistant from the central incident mark. This was repeated at various angles of rotation to assure axial symmetry.

This device had a number of shortcomings and so it was not the final design used. The prism despite of its .12 mm bluntness which was physically only 1% of the beam, still suffered from other defects. Associated with this edge is a larger inaccuracy in angle than the 2' (90°±2') given for the bulk. This inaccuracy is due to the thin edge that lacks the mechanical support of the bulk during grinding, so that it deforms during polishing and relaxes back after pressure is removed. But it is exactly at this edge that one desires the greatest accuracy.

2. Mount

Figure 27 shows the geometric beamsplitter (glass cube) mounted in the inner cylinder of two concentric close fitting cylinders (a rotatable mount). The outer cylinder was mounted onto a cross shaped half inch thick aluminum plate. The cross shaped plate rested on a 1-1/2 in. thick aluminum block with a pair of bolts fastened on either end

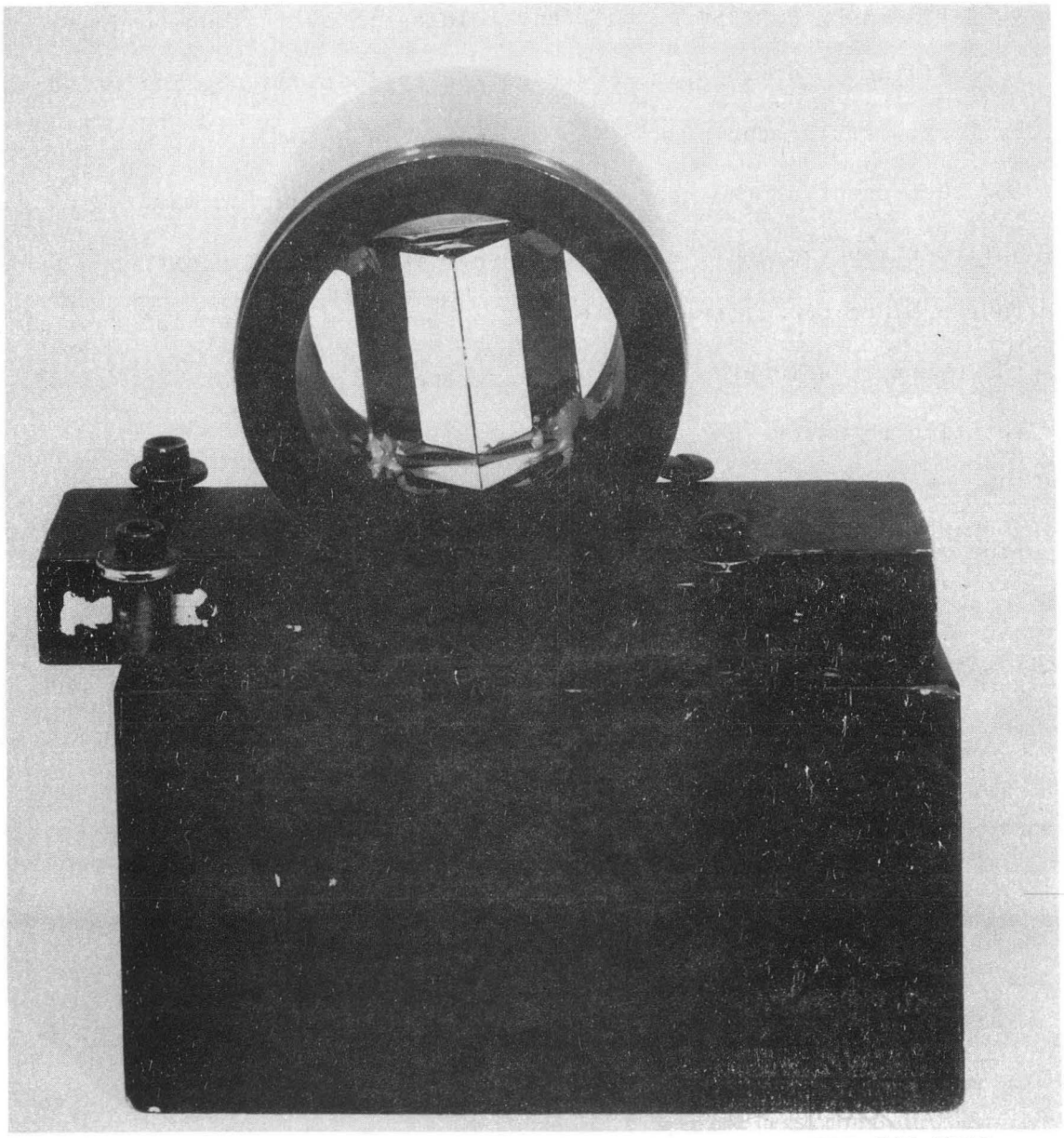

BBC 768-7313

Fig. 27. Geometric beamsplitter module. The geometric beamsplitter is mounted in its rotating and sliding mounts.

of the plate. The bolts were close enough to the plate so that washers on the heads of the bolts which protruded over the plate held the plate tightly against the block. The four bolts were also positioned so that the cross could travel only a certain distance between the two pairs of bolts before its arms struck a pair of bolts. At one end of its travel the beamsplitter was aligned with the laser beams and at the other the rotating mount slid out of the path of the laser beam. The bolts were sheathed in Tygon tubing and were tapped into the block, flush against the plate. This prevented the plate from wobbling. The plate and block assembly served as a sliding mount for the beamsplitter and when the cube slid out of the path of the laser beam, the velocimeter could be operated in the reference mode.

c. Shortcomings. The stability of the sliding mount was critical. It would have had to maintain the incident beam centered at the edge of the cube in order to give identical output beams, since only overlapping portions of the beams interfer. The reliability of the prism returning to its original location after having moved and returned along its rail was not particularly satisfactory for the cube beamsplitter module. Centering the beam on the prism edge and adjusting the prism angle was very tedious and would have had to be repeated if the laser had shifted even slightly. With straps used to secure the laser, this kind of beamsplitter was not advisable because of frequent slippage of the laser.

There were two stronger reasons to reject this geometric splitter. A prism which would give the 2.2 cm separation required for the desired

spatial resolution would not only have been very bulky, but since large prisms have very blunt edges a costly and timely custom made cube would have had to have been ordered.

The other reason was the loss in scatter intensity. Figure 48 shows the intersection volume resulting from two truncated Gaussian beams. If the beams had not been truncated the dotted figure, an ellipsoid but with only half the energy density, would have been the probe volume. The probe volume is fairly small, about 30% of the ellipsoid [see Appendix III), which should provide high spatial resolution (small probe volumes). But most of the region of high fringe density and contrast (core of the ellipsoid) is sacrificed. The region where there are fewer than 3 or 4 fringes should also be lost since the spectrum analyzer probably does not have sufficient resolution to resolve such short wavetrains. Hence one is left mainly with dimmer edge portions of the ellipsoid and a wedge region of dimmer and fewer fringes, resulting in both weaker and fewer detectable signals. Figure 39 illustrates this probe volume.

4. Amplitude Beamsplitter[28]

a. Theory. The shortcomings of the previous beamsplitter led finally to the construction of an amplitude splitting block as shown in Fig. 29. Earlier reluctance to use this design stemmed from both unsuccessful less precise prototypes and the much greater complexity, cost and very slow delivery schedules typical of custom-made components.

Before describing the design of the block, pertinent calculations should be presented for the unique angle of symmetric splitting and

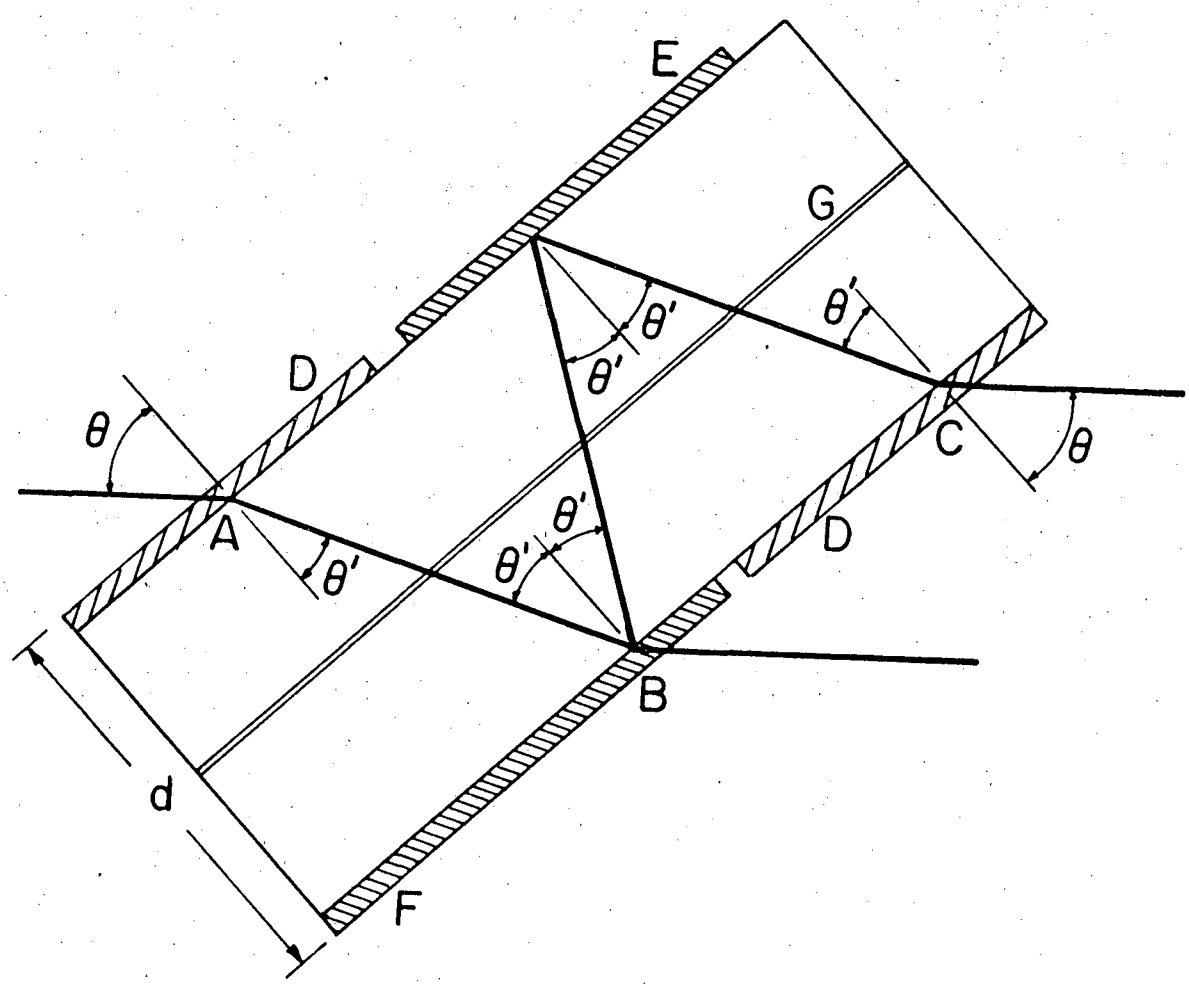

XBL 768-7448

Fig. 29. Amplitude beamsplitter is a rectangular block of glass with appropriate vacuum deposited optical coatings. The size of the block is much smaller than the one shown in Fig. 26. But there is only one angle of incidence which produces output beams which are equidistant to the incident axis. When the block is rotated the output beams will rotate about the incident axis.

Symbols:
- A incident beam
- B location where transmitted output beam exits semi-transparent coat
- C location where internally reflected beam exits block
- D antireflective coating
- E opaque aluminum mirror
- F semitransparent coating-beamsplitter coating which gives equal transmitted and reflected beam intensities.
- G Canada balsam used to cement together the glass plates which form the block
- d thickness of glass block
- θ angle of incidence
- θ' internal angle of incidence

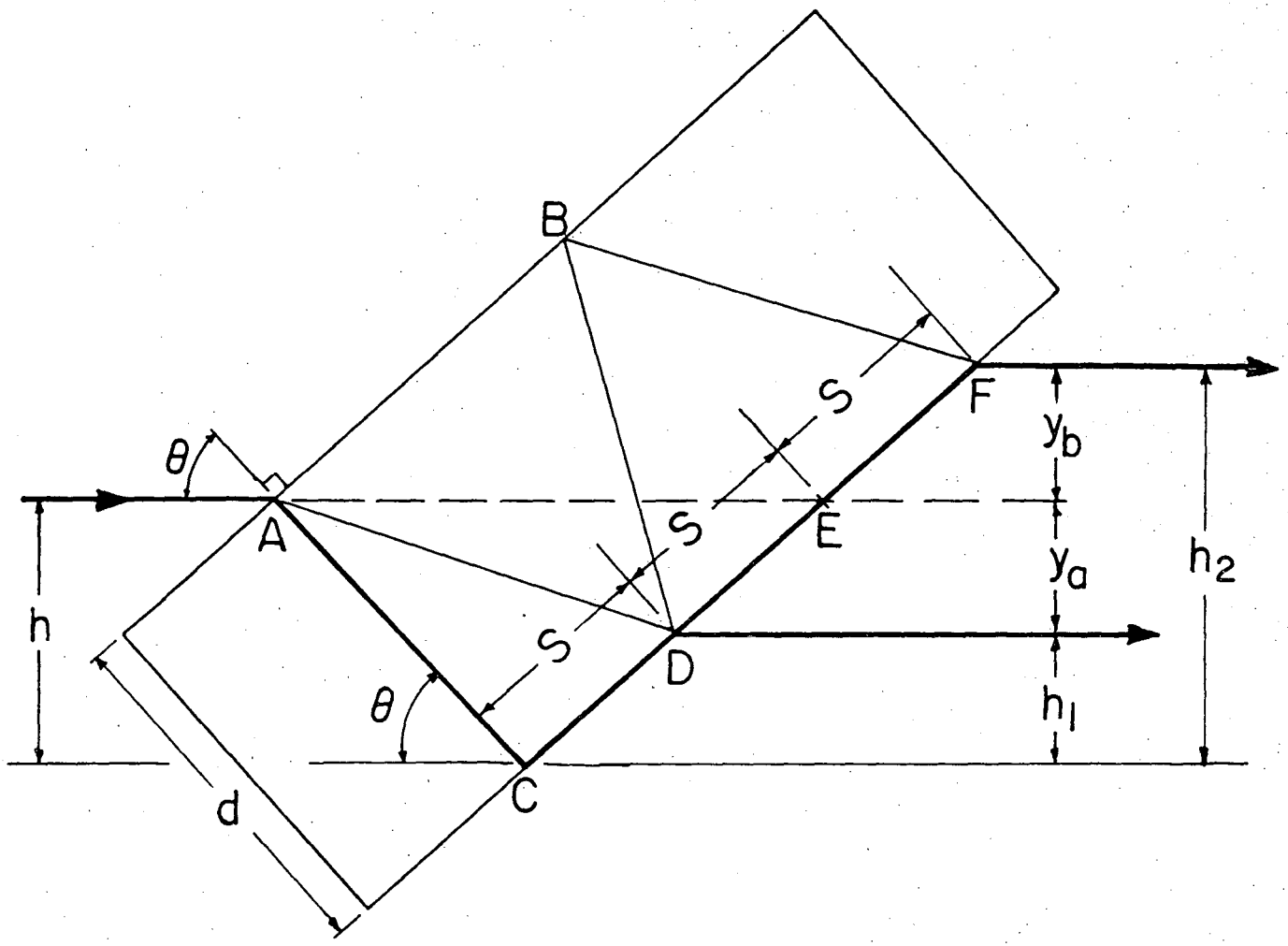

XBL 768-7449

Fig. 31. Simplified form for the mathematical analysis of Fig. 29.

for beam splitting; distance dependence on various geometric and physical factors. The beamsplitting block of Fig. 29 has been simplified for mathematical treatment in Fig. 31. At A of Fig. 31, the source beam strikes the glass surface at the incident angle θ. From Snell's Law one can calculate the angle of refraction θ' as the light enters the prism $\theta' = \sin^{-1}\left(\frac{n_{air}}{n_{glass}} \sin\theta\right)$. Because the internally reflected beam ADBF reflects between two parallel faces and because the angle of reflection must be equal to the angle of incidence, angles $2\angle CAD = 2\angle BFG = \angle ADB = \angle DBF = 2\theta'$ (see Fig. 29). Since the triangles containing these angles are equal, CD=DF=EF=S. From geometric arguments

$$S = d \tan\theta' \tag{17}$$

$$h = d \sin\theta \tag{18}$$

and

$$h_1 = S \sin(90-\theta), \quad h_2 = 3h_1$$

Thus one can now calculate the amount that each of the two output beams has been shifted from the incident beam, namely;

$$y_a = h_2 - h \tag{19}$$

and

$$y_b = h - h_1 \tag{20}$$

By taking the derivative of the difference $y_a - y_b$ and setting it equal to zero, one should get the angle of symmetric splitting. Because of mathematical consideration (there is no solution for $\frac{d}{d\theta}(y_a - y_b) = 0$), $\frac{d}{d\theta}(y_a - y_b)^2 = 0$ must be used. A computer solution for this angle is

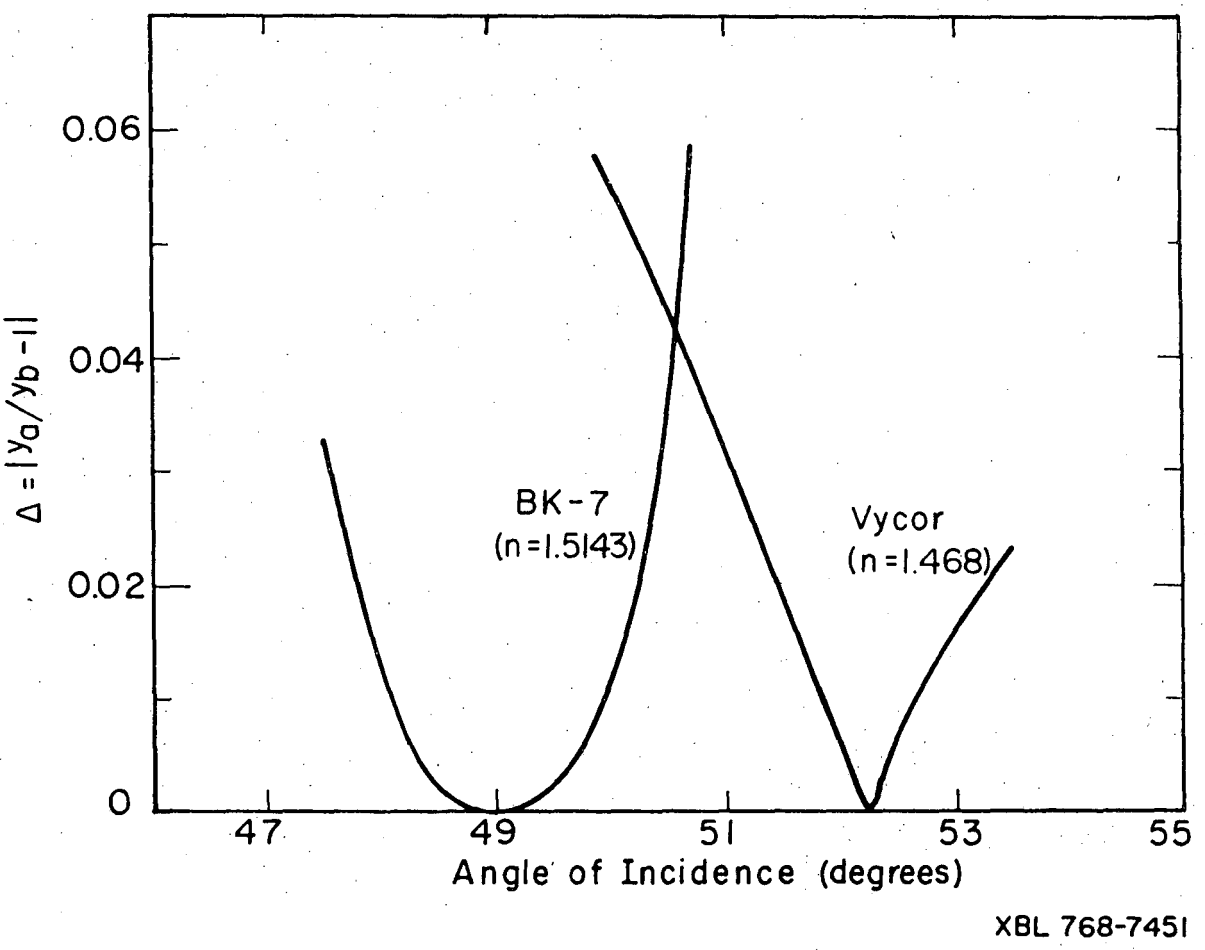

Fig. 34. Sensitivity of the angle of incidence to Λ, the ratio (y_a/y_b-1), (see Fig. 29).

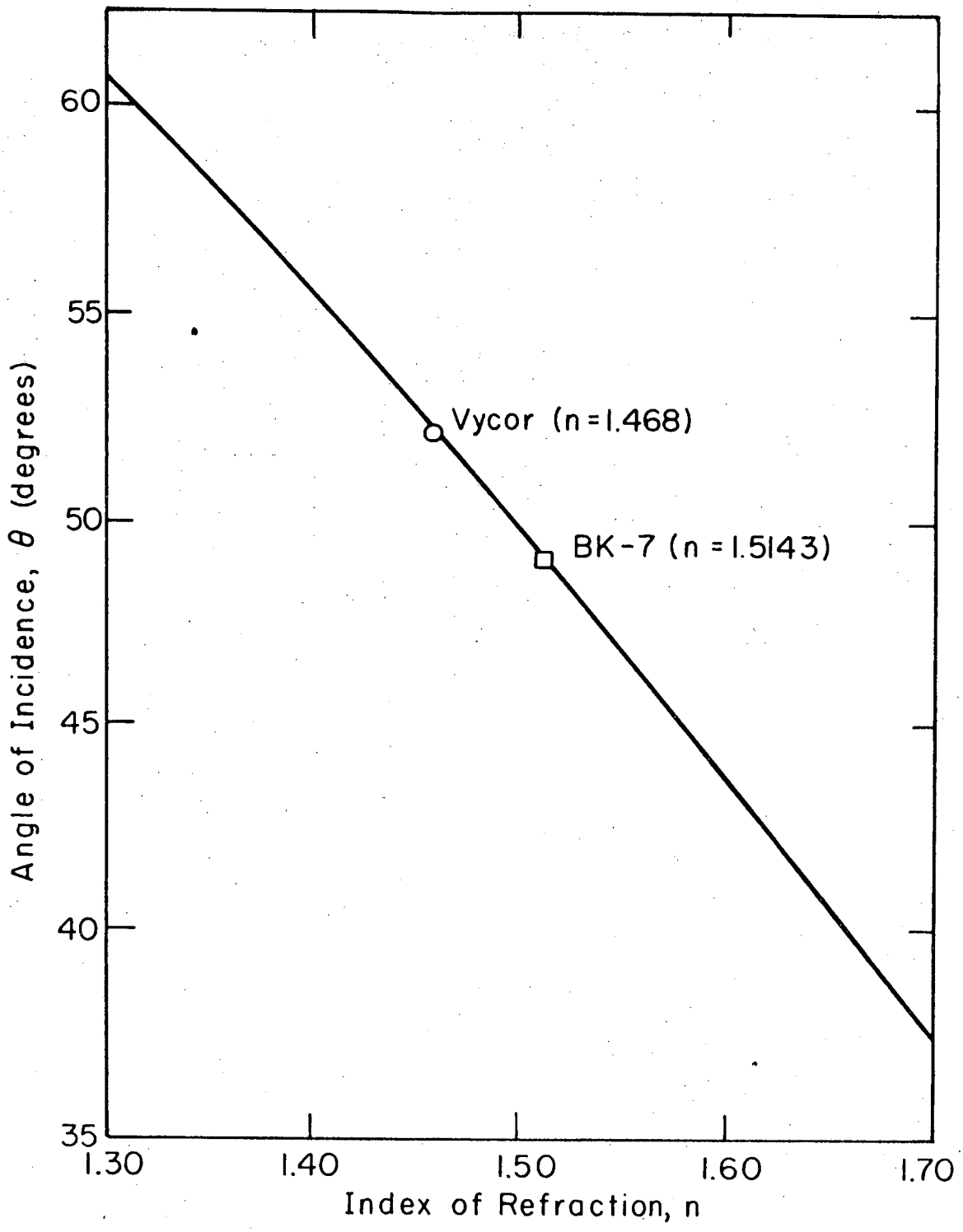

XBL 768-7452

Fig. 35. Axisymmetric angle of incidence θ plotted against the index of refraction, n, of the beamsplitter block. There is a unique angle of incidence for the amplitude beamsplitter shown in Fig. 29 at which the output beams are split equidistant to the axis of the incident beam.

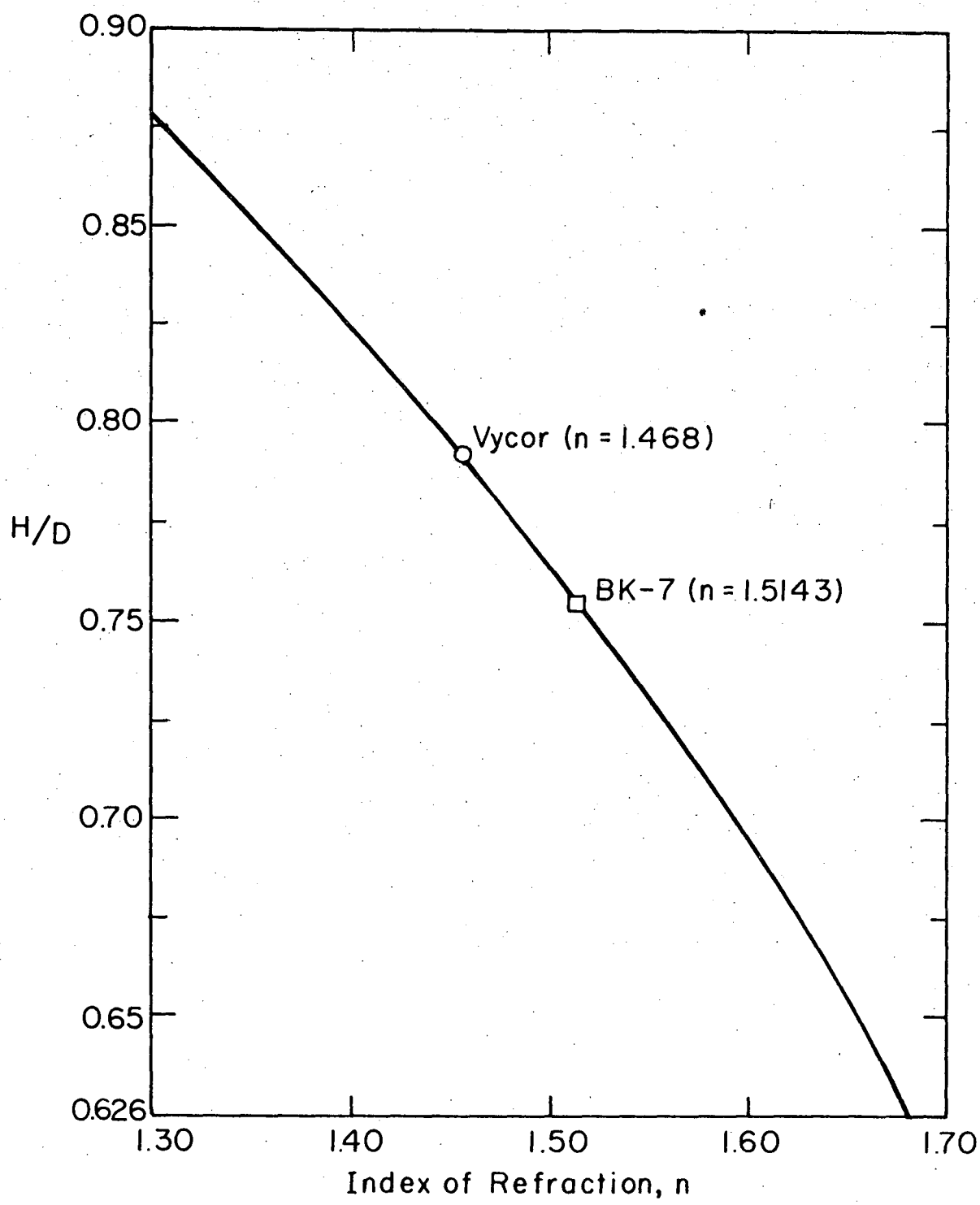

XBL 768-7453

Fig. 36. Ratio of the distance that the output beams are separated ($y_a+y_b=H$, Fig. 29) to the block thickness D, plotted against the index of refraction, n, of the beamsplitter block. The ratio H/D is evaluated at the incident angle which gives symmetrically split output beams (see Fig. 35).

shown in Appendix III.

Figure 34 shows the strong dependence of the angle of incidence on the required for symmetric beamsplitting. Figures 35 and 36 shows the splitting distance at this angle as a function of the index of refraction and angle of incidence. Note that the splitting is linearly dependent on the block thickness.

b. Construction. Prototypes of cemented stacks of thick flat glass plates cut from mirror stock indicated several problems as well as confirming preliminary calculations. Despite the apparent thickness and flatness of the glass, after cementing with either a very slow cure epoxy (6 days) or Canada balsam, the exiting beams were always skewed and usually convergent. Faster curing epoxies would cure first at the edges and reticulate (it forms a fishbone pattern of voids) in the center. The extent of parallism of the two output beams emanating from the beamsplitter block depended on the angle at which the block was rotated. Beams which initially had a 2 centimeter spacing and which were vertically aligned when they were near the beamsplitter block, became horizontally aligned and were spaced only 1.5 centimeters apart after the beams had travelled three meters. At one angle of rotation, the location of the beams on a screen three meters away were observed to overlap. The curvature of the surfaces of the blocks were checked against an optical flat and showed a curvature of 10 fringes/inch. The curvature necessary to have caused the degree of skewness as experimentally observed would have had to have been much greater. This would indicate that preferential curing of the cement at the edge (contraction) warped the blocks. Various optical coatings were needed for this device. Calculations for the unique angle at which symmetric

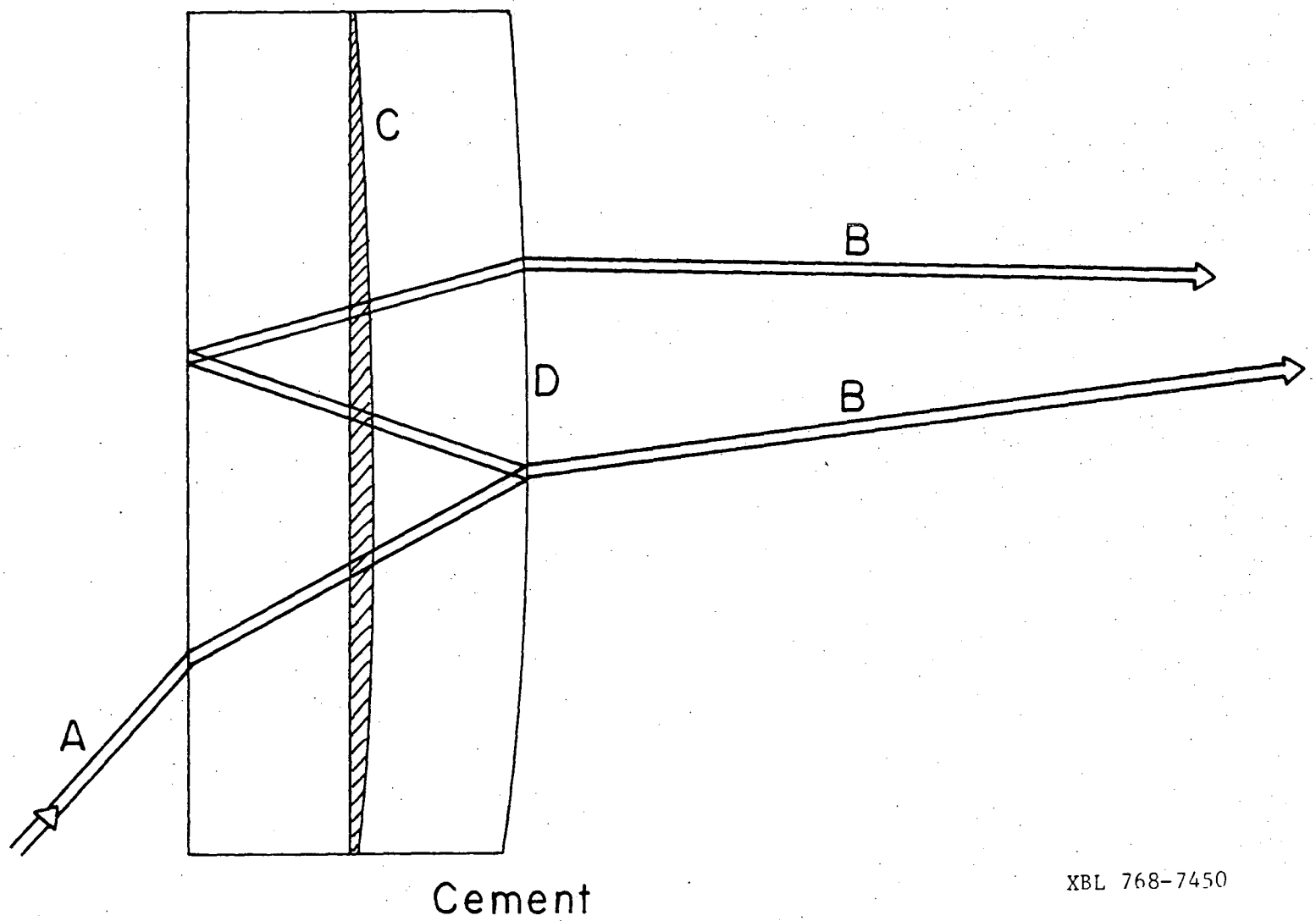

XBL 768-7450

Fig. 32. Possible cause for the skewing of beamsplitter beams may be the accumulation of cement between the plates forming the block. When a large amount of cementC, accumulates between the two plates forming the beamsplitter (Fig. 29) the plates warp.

splitting occured showed that the incident angle was close to that for total reflection. This made an antireflective coat necessary at the incident surface. Another antireflective coat was placed on the surface where the internally reflected output beam exited the block (see Fig. 29). The aluminum coatings in the figure were more troublesome because of dust particles in the vacuum depositing shops. The opaque aluminum mirror had to be deposited, cleaned and given a second coat to produce a pinhole free mirror. When the aluminum semitransparent mirror was deposited, the prism was positioned at the desired angle of incidence and the external reflection was monitored during slow vacuum deposition. The standard 38% transmittance, 38% reflectance was observed on the air-metal surface. But when the beam was sent through the prism from the antireflective coating side two equal output beams were not achieved. The transmitted beam was considerably brighter. It was first thought the greenish glass of the prism strongly attenuated the internally reflected beam, since its path was three times longer than the transmitted beam. But prisms later made with clear glass showed the same behavior. Various schemes described in the next section were tried to correct this problem.

In the final design two 5/8 × 3 × 7/8 inch blocks of optical quality schlieren free Vycor[74] (n=1.567) were cemented with Canada balsam to give a 1.25 inch thick block with a beam separation of about 2 centimeters. Various vacuum coats were adjusted to an incident angle of 52°, trials were made to compensate for equal intensity beams by removing the deposited semimirror on the prototype and using a semimirror

of variable transmittance (thin aluminum wedge coated onto a glass substrate) to ascertain the coating thickness needed for an actual even intensity split. These plates were held in place either by Canada balsam or silicone oil (index of refraction matched with glass). But they still proved unsatisfactory because the making of such aluminum slides was a timely trial and error process. Moreover thin slides or coverslips often deformed and were themselves rarely flat. 1.2 millimeter thick slides were also tried but proved even worse than the coverslips since the thinner coverslips could at least be made to compensate for surface curvature by distorting them with shims (.001 in. brass) tucked between the slip and the slide at appropriate locations. The aluminum coats were very easily damaged by abrasion. Uncoated mirrors with correct transmittance and reflectance ratios changed their ratio when the coat was abraded and even more drastically when coated with a hard protective MgF_2 coat. In many of these coated mirrors, the aluminum coat became a gray underlayer after deposition of the dielectric. Besides the above problems, thick cements did not permit manipulations of the slides, while thinned cements or oil either caused the slides to slip or upon drying changed their surface curvatures. Hence precoated slides did not work.

It was not until a ratio recording spectrophotometer[75] became available that the next step could be taken. This was to coat the block with its other three coatings, cement it and mount it. Then the incident beam was passed throught the window of the vacuum deposition chamber and the outputs monitored at an opposite port. The resulting

two output beams went to fiber optics collectors, which placed the beams on fixed location of their corresponding phototubes, giving very reproducible intensity measurements. The fiber optics not only required the centering of the light beams but also that the laser beams entered normal to its face. (A ring of light exited onto the phototube if the collecting lens of the fiber is off parallel with the beam by as little as 7°.) When the intensities were monitored on the ratio recording spectrophotometer, deposits gave matched transmitted and reflected output beams.

After the coatings were deposited the blocks were tested. The Vycor plates gave skewed beams (a 30° rotation of beams at 8 meters away). But before cementing, dusted stacked blocks showed less skewness (10° at most). Apparently the application of the balsam distorted the plates. After the assembled block was annealed at 300°F for half an hour, more heat or time would have caused the decomposition of the balsam as noted by its yellowing, the weight of the glass plates squeezed out the excess less viscous hot balsam. The glass plates then relaxed back into their original flatness. Another hour was allowed for slow cooling to insure uniform stress.

Even though optical epoxies were mechanically more stable, and would never dry out like balsam they could not be used. They either cured too quickly and reticulated under heat, or would require 6 days to cure, and still not ensure flatness or low stress. But balsam was sensitive to solvents (cleaning solutions for the optics) and oxidized in air, and thus the plates would slowly yellow and separate.

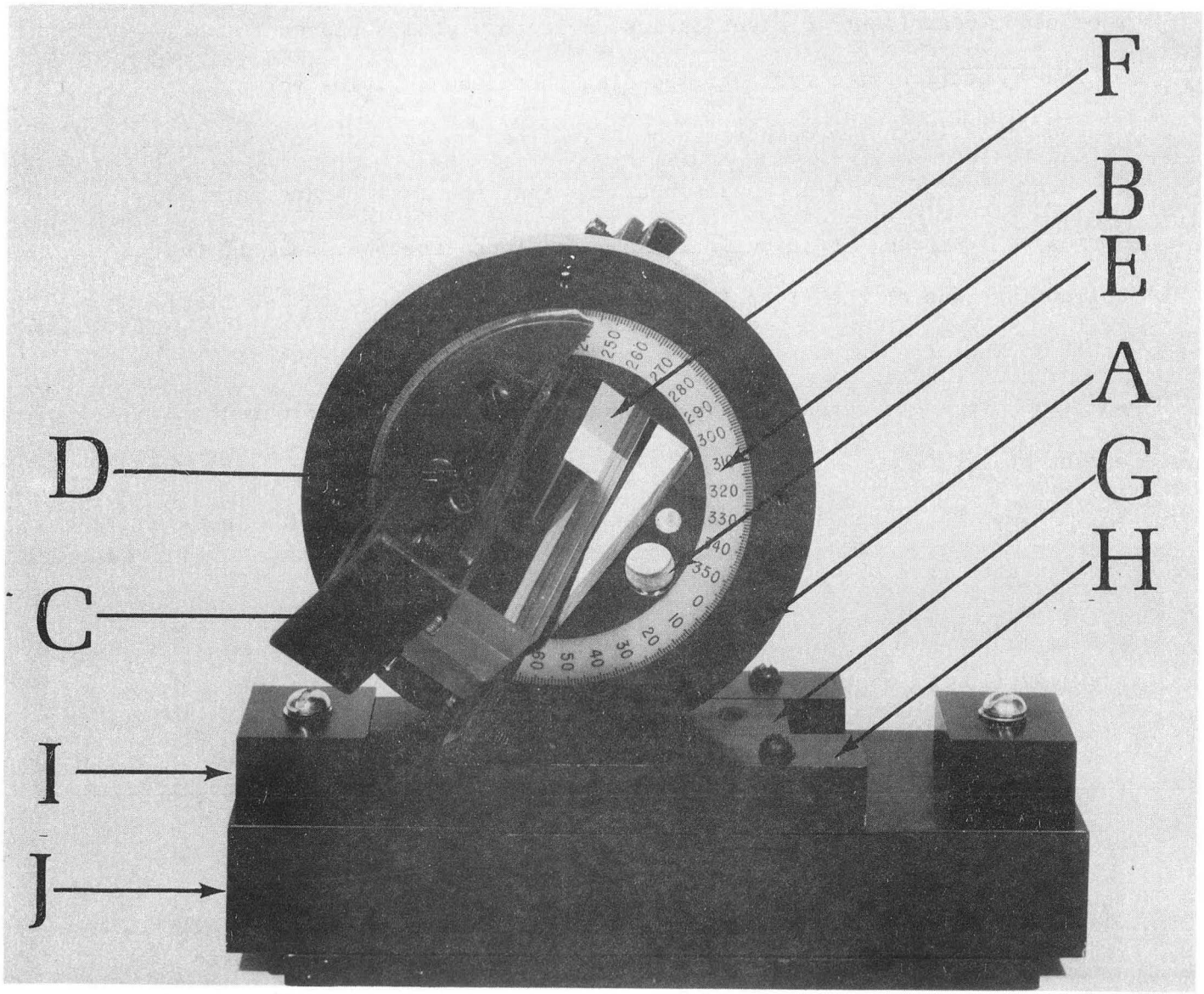

BBC 768-7311

Fig. 37. Beamsplitter module, the amplitude beamsplitter is mounted in its rotating and sliding mounts.

A the outer ring of the rotating mount
B the inner ring of the rotating mount
C the plate onto which is mounted the beamsplitter
D the platform onto which is mounted the plate C
E a hole bored into the inner ring to permit the laser beam to bypass the the beamsplitter module for operation in the reference mode
F the beamsplitter prism
G the dovetailed bar onto which is mounted the rotating mount
H metal bars forming a slot into which the dovetailed bar can fit tightly but can also slide along the slot.
I metal pieces limiting the travel of the sliding mount
J base of the beamsplitter module.

To prevent this an epoxy was applied to the edges to seal the balsam from air.

A block of borosilicate crown glass (BK-7) was finally installed into the splitter assembly instead of the above mentioned Vycor. This was done after Tinsley Laboratories[76] had made a gift of an exceptially polished spacecraft window scrap with a one twentieth of a wavelength per inch flatness and parallel in thickness to within 0.7 second of arc/4 inches. The glass had a yellowish tint but it was not assumed to absorb much light in the red range. The block assembled from this glass showed only minor skewness.

C. The Beamsplitter Mount

The design used for the rotating and sliding mount of the geometric beamsplitter could not be used for the amplitude beamsplitter. The prism of the amplitude splitter required a greater degree of precision in alignment of its incident angle, and was also much larger than the glass cube. The mount designed for the amplitude splitter is shown in Fig. 37.

The rotating mount of the prism was made from two half inch thick aluminum rings which were machined with very close tolerance so that the smaller ring(B) would fit securely and concentrically into the larger outer one (A). So that the angle of rotation could be read as 1/4 inch wide annular dial with a 360 degree scale was embedded into the edge of the inner ring. A rectangular hole was milled in the center of the inner ring. A platform for the mounting of the prism passed through the rectangular hole and was bolted onto the inner ring at an angle such

that the prism when installed would be positioned at the desired angle of incidence. Onto the platform was mounted the plate (C) which held the beamsplitter prism. This plate was held to the platform by two screws, one centered at the edge at both ends of the plate. One screw served as a pivot, while the other fitted into a slotted hole. This slotted hole permitted a ± 10° play in the angle of incidence which was necessary for the final alignment of the prism. This ± 10 degrees of adjustment was also need when another beamsplitter made from a different type of glass was used since a different incident angle would now be required to give output beams which would be equidistant from the incident axis (see Fig. 34). At each corner of the plate a screw from the plate pushed against the platform which provided the plate and hence the prism with height and tilt control.

The rotating mount was much larger than the cylindrical mount of the geometric splitter, so that it required a larger clearance space in order to move out of the path of the laser beam. But the high density of components in the vicinity did not allow for the needed clearance space. To permit operation in the reference mode, a 1/4 inch diameter hole was bored into the inner ring. Hence the rotating mount was slid only 1-1/4 inch before the laser beam exited through the hole (E).

The sliding mount was also more rigid than that of Fig. 27. The outer ring (A) was securely bolted onto the dovetailed bar of aluminum (G). A bar of complementary geometry fitted tightly against either side of the dovetailed bar. These bars were bolted onto a

0 0 0 0 4 6 0 8 0 8 7

1-1/4 inch thick aluminum block forming a slot into which the dovetailed bar with its rotating mount could slide and yet not wobble. Two square end pieces limited the lateral movement of the rotating mount. The prism with its rotating and sliding mount formed the beamsplitter module, and was bolted onto the velocimeter's baseplate as shown in Fig. 6.

D. Advantages

This new splitter shows a number of desirable features. From studying Fig. 37 (mounted splitter) and Fig. 28 (glass cube) one can see that there is no fixed location for the incident beam to give equal splitting. Hence the prism with its large incident receiving area may be moved into and out of the beam, or rotated without misalignment.

Another advantage is the large increase in the number fringes[60,77] resulting in a longer residence time in the intersection volume. This longer residence time coupled with a large increase in fringes in the brightest section of the ellipsoidal probe volume should give much stronger and longer signals. Hence this should improve the SNR.

This author feels though that the residence time of the particles in the probe volume is more important than the intensity arguments. The cube splitter beams are about twice as bright as the prism beams. The prism splitter suffers from a number of losses in intensity. These include at least a 24 percent loss at the aluminum semimirror (a high efficiency dielectric coating would reduce this to about one percent, but would be extremely expensive[78]), attenuation thorough the glass which should be minor, and more importantly losses at the incident

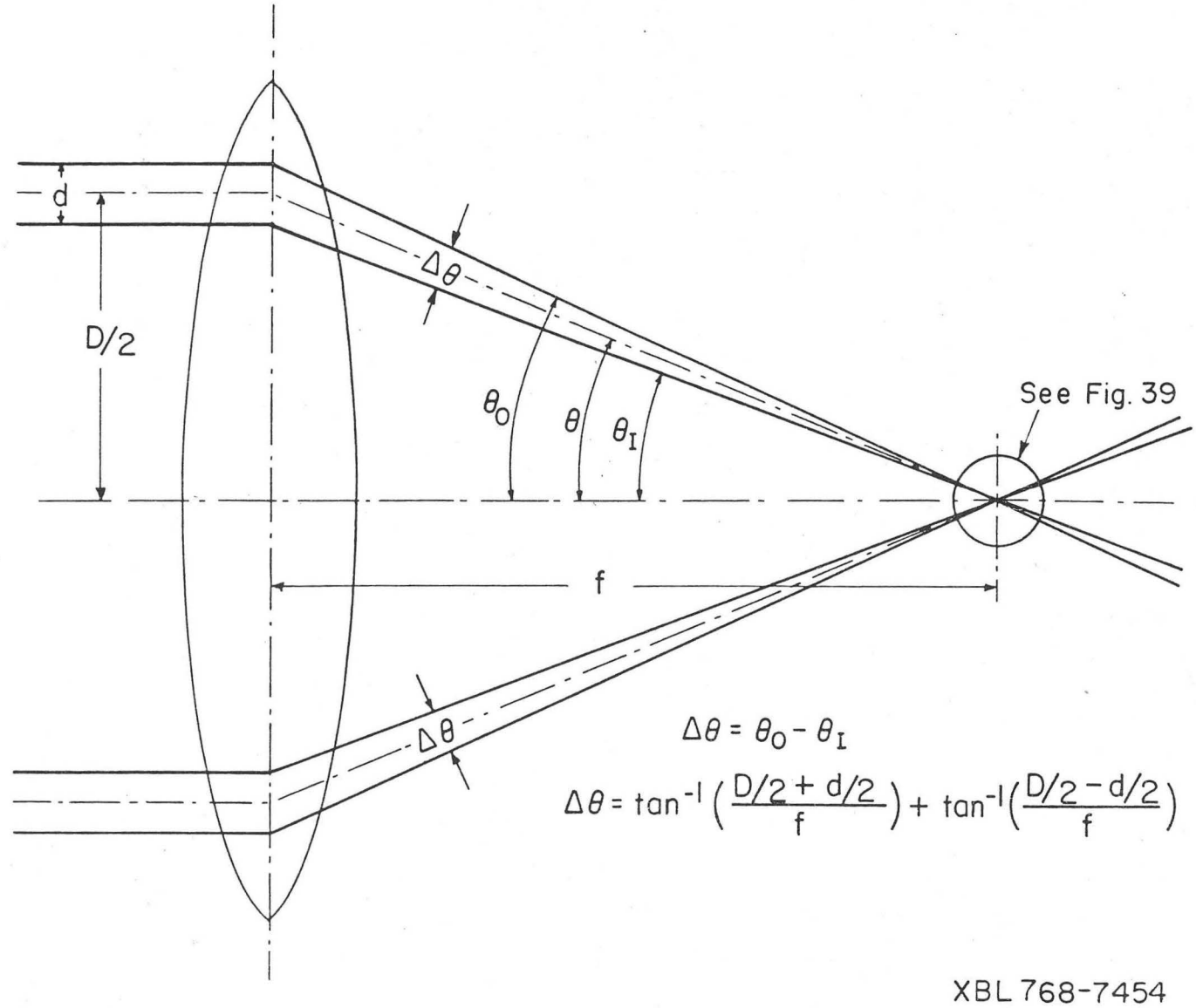

Fig. 38. Definition of $\Delta\theta$, the angular width of the focused laser beam.

0 0 0 0 4 6 0 8 0 8 8

Fig. 39. Intersection of two intersecting laser beams with Gaussian intensity distributions (note the I vs r curves) form a lozenged shaped volume. This volume can be approximated as an ellipsoid (dotted figure). The ellipsoidal volume ignores the small and dim corner regions.

Symbols:

D_f fringe spacing

Δy length of the y axis of the ellipse

Δx length of the x axis of the ellipse

θ 2θ is the angular separation of the two intersecting beams

U is a scattering particle which is traversing the light and dark fringes.

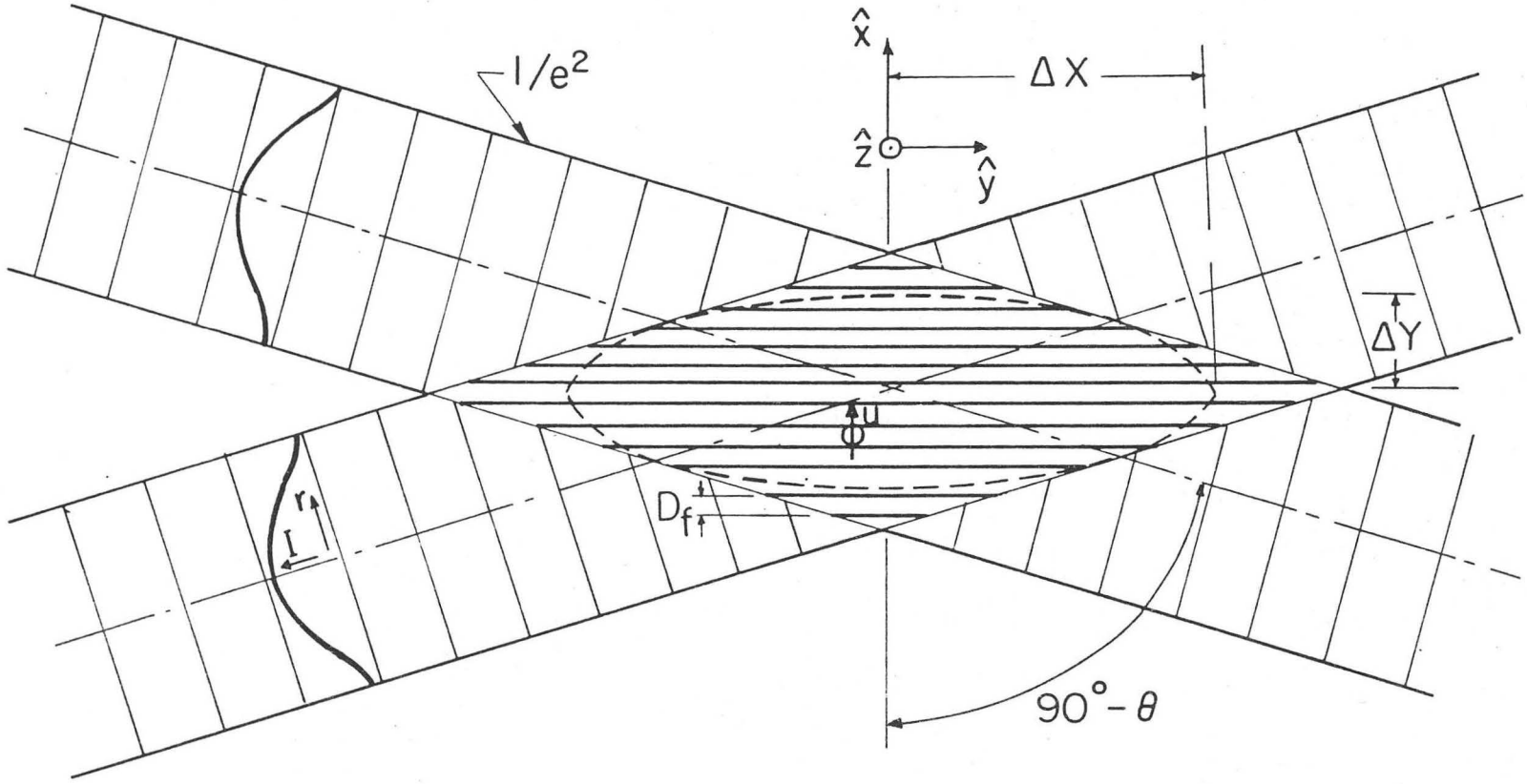

XBL 768-7455

Fig. 39.

anti-reflective coat. The present is a MgF_2 coat adjusted for an incidence angle of 49°. This is quite close to the total reflection angle for MgF_2 (n = 1.38, critical angle = 46.4°). Although CaF_2 has poor mechanical qualities it should greatly reduce such losses since its total reflection angle is 54.4° (n = 1.23).

Fringe contrast should not be a problem for the prism despite an optical path difference of approximately 3 in. (see Fig. 16).

5. Altering the Probe Volume

To use the velocimeter as a high spatial resolution instrument one must not only known the size of the probe volume, but also be able to alter it. When two Gaussian beams with $I/I_o = 1/e^2$ edges intersect, their volume is an ellipsoid. Intersecting non-Gaussian beams would produce a lozenge shaped volume. This intersection is further complicated if the focusing lens has aberrations. But since a camera lens closely represents an ideal lens, the light distribution at the focal point is essentially diffraction limited. The diffraction limited pattern at the focal plane has a diameter equal to the Airy disk and determines the z and y axes of the ellipsoid as shown in Fig. 39. The mathematically derived dimensions[79,80] of the ellipsoidal probe volume as shown in Fig. 39 are given below. As mentioned earlier ΔZ [$\Delta Z = 4\lambda/(2\pi\Delta\theta)$ Eq. (18)] is diffraction limited. For small θ values, one would expect that $\Delta Y = \Delta Z$. (If the two beams overlapped the overlapping circular diffraction patterns of the two beams would also be circular.) As a matter of fact, ΔY [$\Delta Y = 4\lambda/2\pi\Delta\theta\cos\theta$, Eq. (19)] is only 5% larger than ΔZ when θ is as large as 18 degrees. The length

of the ellipsoid should stretch to infinity when the beams overlap $\theta = 0$, and $\Delta Y = \Delta X$ when the $\theta = 45°$. This behavior is seen in

$$\Delta X = \frac{4\lambda}{2\pi\Delta\theta \sin\theta} . \tag{20}$$

The fringe spacing is D_f,

$$D_f = \lambda/(2 \sin\theta) \tag{21}$$

which determines the number of fringes N_f,

$$\Delta Y/D_f = 8\tan\theta/(\pi\Delta\theta) = N_f . \tag{22}$$

The variable $\Delta\theta$ is derived from geometric considerations on Fig. 38,

$$\Delta\theta = \tan^{-1} \left(\frac{D/2 + d/2}{f}\right) - \tan^{-1} \left(\frac{D/2 - d/2}{f}\right) . \tag{23}$$

In Table 3 the dimensions of the intersection volume are calculated for various beam separations and beam diameters. The values of the dimensions shown in Table 1 were derived from Eqs. (19-22) with a correction for the values of $\Delta\theta$ and θ. They were corrected for the effect of refraction at the flow cell wall using Snells law. The index of refraction and effective focal length of the observing lens were 1.33 and 50 mm respectively. Note that since ΔZ and ΔY are diffraction limited dimensions, that they are essentially equal.

For the above table one can see several limitations of the differential mode. For small beam separation, D, (see case 1), the probe depth $2\Delta X = .25$ mm is large, ΔX is closely half the thickness of the roll cells that Hickman[1] reported, and does not provide measurements of high spatial resolution. In Case 4, the laser beam diameter d, is expanded to 4 times that of Case 1. As a result the probe depth ΔX

Table 1

Case	D, cm	d, cm	N_f	$\Delta X, \mu$	$\Delta Y, \mu$	$\Delta Z, \mu$
1	1.11	0.17	8.4	125	18.4	18.2
2	1.11	0.68	2.1	31	4.6	4.55
3	2.2	0.17	17	68.3	20	19.2
4	2.2	0.68	4.5	17.2	5.0	4.8

index of refraction, n = 1.33

XBL 768-7417

0 0 0 0 4 6 0 8 0 9 0

shrinks by a factor of 4. But the number of fringes also decreased by a factor of 4, which unfortunately limits the number of cycles in the wavetrain of the signal and a short signal wavetrain would severly limit the ability of the electronics to discern the signal.

In Cases 1 and 3 or 2 and 4, one can see the effects of enlargening the beam separation, D. By increasing D, not only does the probe depth ΔX decrease, thus giving higher spatial resolution, but the number of fringes N_f, also proportionately increases. This increases the number of cycles in the signal wavetrain and thus improves the chances that a signal will be discerned by the spectrum analyzer. In increasing D the fringe spacing D_f (Eq. 21), decreases and thus affects the selection of the size of light scattering particles used.

6. Light Scattering Particles[88,89]

The particle which traverses the probe volume's fringes gives the sharpest signal when the intensity is strong. For dielectric particles where the particle diameter is smaller than the wavelength, contrast is sharp as the particle traverses the fringes (the fringes are larger than the wavelength). But the intensity is low since scattering cross sections are small. One cannot improve the intensity by increasing the number of particles since they enter the probe volume at random times. Hence they pulsate in random phase, producing a weak ac and a strong dc signal on the phototube.

The advantages in using this dipole scattering regime (Rayleigh-Gans Scattering)[81] are that backscattered and forward scattered

intensities are nearly equal, and that such small particles of neutral bouyancy are assured of flowing as if they were part of the fluid, even if they are in turbulent eddies.

If spheres of diameters in the range of probe volume fringe spacings were used, one would imagine that the signal intensity would be greatly improved, increasing either by r^3 (number of dipole molecules) or at least by r^2 (increase in scatter cross section). Yet contrast should remain as sharp as in the previous case, as long as the particle diameter is the same size as the fringe spacing up to dpart=d fringe, for one particle per probe volume.

With particles larger than the wavelength, one leaves the dipole scattering regime, and enters the geometric and diffraction scattering regime.[82] Now the forward scatter intensity is two to three orders of magnitude higher than the backscatter intensity, with lobes at other angles also. This particle size range is then excellent for forward scatter experiments but very poor for this author's purposes. But despite the low backscatter ratio they may scatter more light than the small Rayleigh-Gans sized particles.[83]

Metallizing light hollow particles or using metals particles can reverse the above behavior, giving the characteristic cardiod curve of intensity versus polar angle of observation. Neutral density metal spheres in the micron range are not available, so that hollow glass spheres must be coated by electroless deposition with either a silver or nickel coating. Small metal flakes such as brass sink slowly unless constantly stirred. Aluminum flakes tend to float, or clump

and sink, possibly due to a oily coat on the metal. Scaps can be used to dissolve the oil and thus suspend the aluminum, but this also attacks the clumps very slowly. Clumps when broken, release their oily coated flakes which float to the surface. Concentrated soap solutions with dissolved suspended aluminum particles, did not produce any more floating flakes, but rather the suspended matter slowly dissappeared in 3 days. Perhaps they were oxidized to a clear oxide. For particle diameters greater than fringe spacings, the scattering process remains unchanged but the intensity should increase by r^2. Such large particles will be clearly seen by the phototube, but they settle easily, and can hardly be expected to accurately reproduce the fluid flow pattern. Their use are mainly for testing the sensitivity of the receiving optics and electronics.

It is curious to note that for particles as large as the probe volume, that the fringe model suggests two wavetrains. One as the particle enters the volume, crossing the fringes, and one as the particle exits the volume, none when all fringes are lighted. But the wave vector analysis suggests that the signal should be constant, and possible brighter as the bulk (equatorial zone) of the particle begins to scatter.

0 0 0 0 4 6 0 8 0 9 2

V. EXPERIMENTAL

A. Differential Mode

A small flow channel was built of plexiglass but even light scratches in the walls were enough to significantly reduce the signal to noise ratio. When microscope slides which were flat when checked against an optical flat, and did not have orange peel surfaces replace the plexiglass walls, the noise level was much reduced. The 1/8 by 5/32 rectangular flow channel with glass window is illustrated in Fig. 40.

The water was driven through the channel by a single stroke piston pump with a 1/3 horsepower, 1732 rpm motor and a "Zero-Max" power block to provide an adjustable drive rate to the piston shaft. Settings of the power block gave constant speeds, but the same setting at different runs were of different speeds, so that the revolutions per seconds of the piston drive shaft gear were timed for each run. This motor had three shortcomings. When it stopped a large inductive discharge travelled through the electrical lines and induced a spurious peak on the spectrum analyzer (Fig. 43). It has a limited capacity which meant frequent stopping to refill the reservoir (suction and compression rates differed at the same block setting). And a disturbing feature of the motor was its high degree of vibration. This vibrated the isolated stand on which the pump stood, and propagated its vibration through the connecting tubes to the flow channel. This would be a possible source of noise from acousto-optic interactions. Accompanying the vibrations was a great deal of whinning, which is most unpleasant to the pump

operator. This pump was replaced with a miniature, centrifugal, variable voltage (head), D.C. motor driven (3-6V) pump. Its lower half was submerged into a recirculating reservoir, thus providing for quiet and continuous, operation. Moreover the open reservoir permitted quick changes of seeding solutions, cleaning, and the installation of a magnetic stirrer to maintain particle suspension. Output though required bucket velocity measurements.

B. Miniature Flow Channel

Data were taken on the small flow channel for 2.02 and .822 micron latex scattering particles dispersed into glass distilled water at the concentration of one particle per differential mode probe volume. Solutions were made by successive dilutions from 10% stock solutions of "Dow" latex solutions.[51] The intermediate dilution solutions also permitted easy increases in particle concentrations as 2x, 4x and 8 times the original concentration by addition of a small amount of that solution.

Flow rates were adjusted to 1 cm/sec. or less, approximating expected boundary layer velocities. Observations were made normal to the channel wall, positioned 1 in. from location of fluid entrance into the duct, and viewed without a downward observation angle.

With 22 ppm for 2.02 μ diameter latex spheres and 1.5 ppm for 0.8 μ spheres (one particle per volume, 4.32 and 1.8 cc 10% stock solution to 120 liter water respectively) and a forward velocity of 1 cm/sec the residence time of a particle in the 20 micron diameter intersection volume was 2 msec. With spectrum analyzer settings of 500 Hz/horizontal division, and allowing for an extremely conservative

0 0 0 0 4 6 0 8 0 9 3

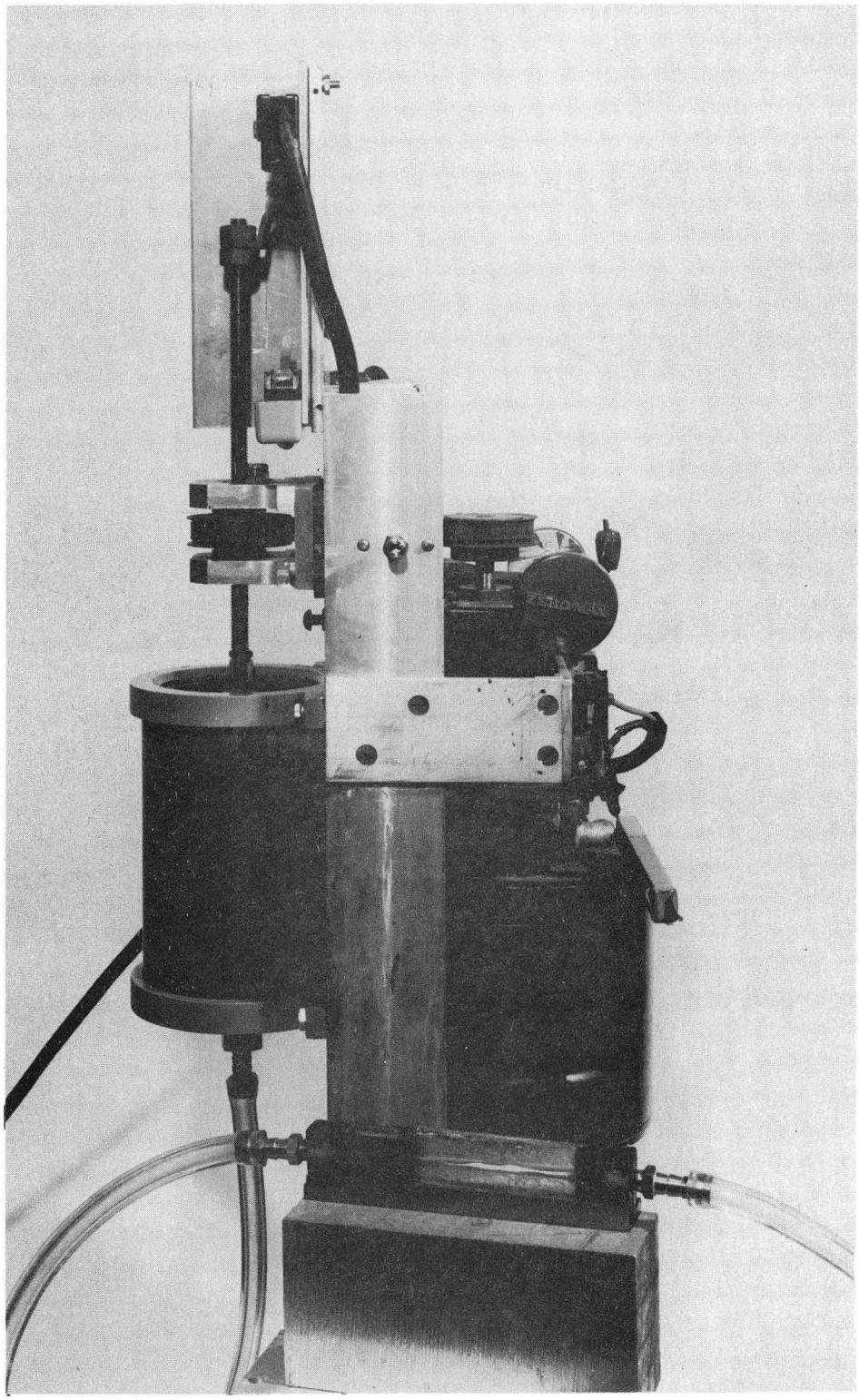

BBC 768-7314

Fig. 40. Miniature flow cell with piston pump.

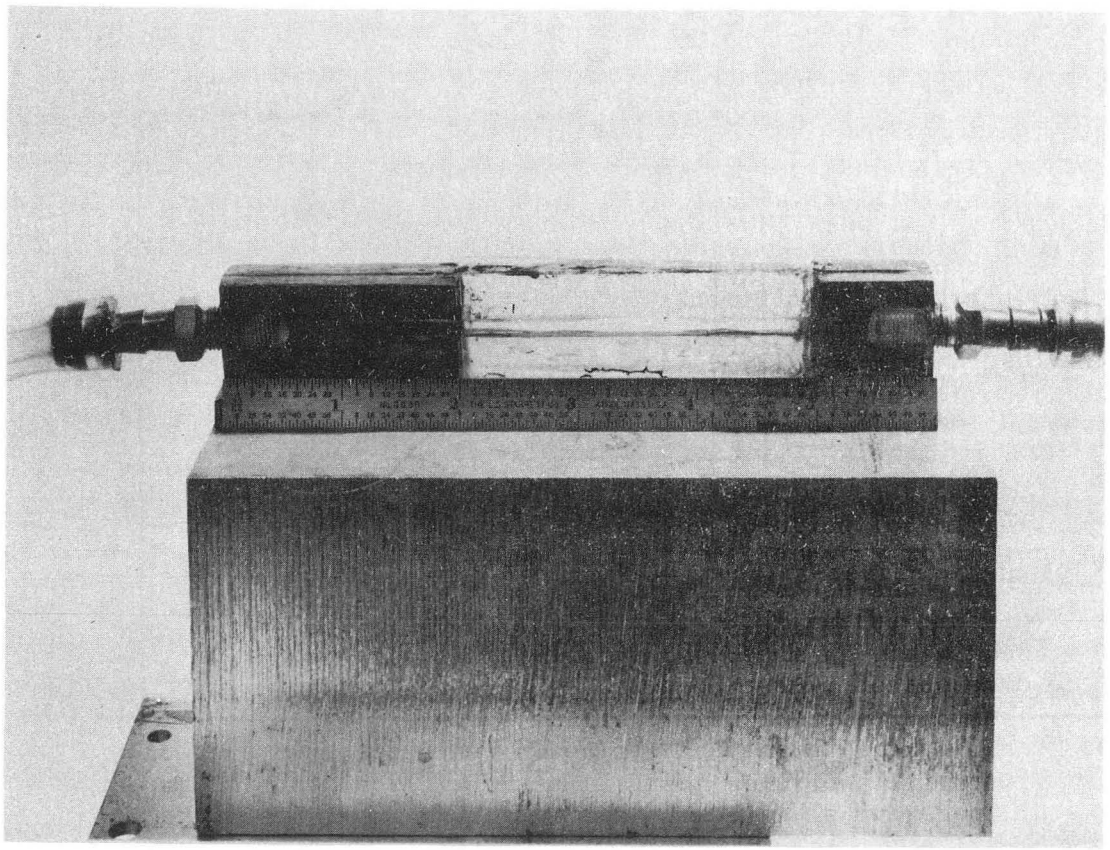

BBC 768-7312

Fig. 41. Miniature flow channel.

peak bandwidth of 100 Hz (later diffuse reflecting disk experiments show a 1 KHz spread at half peak), this region would be scanned over a period 20 seconds (at 100 sec/division). Thus 10^4 particles would have been observed during such a period. But attaching the phototube output to a differential amplifier showed only of the order 10 signal bursts per second (mV ranges). This suggested either a lack of sensitivity on the part of the phototube, insufficient signal strength, or excessive stray light.

The signals displayed on the spectrum analyzer (Fig. 43) showed what must have been stray particles or bubbles large enough to scatter a sufficient light intensity and over a sufficiently long duration that it was processed. The narrow peak of the signal also implied that it must have been due solely to one particle, with its frequency given by Eq. (14).

The observed fluid velocity derived from signals displayed by the spectrum analyzer agrees with that expected for the volume average velocity (Fig. 42), a laminar velocity profile was not yet established in the channel as one would expect for observations 8 channel diameters downstream from the inlet. Probably because of the limited electronics available, despite the larger signal rate recorded by the differential amplifier, the spectrum analyzer read a signal only once in every 3 to 5 scans. This was a average of one per hour. When not using the 2.02 micron particle, such as, .822 and .2 micron diameter latex particles, signals were even more infrequent (none were ever observed for .2μ). Increased concentration of particles did not show any improvement.

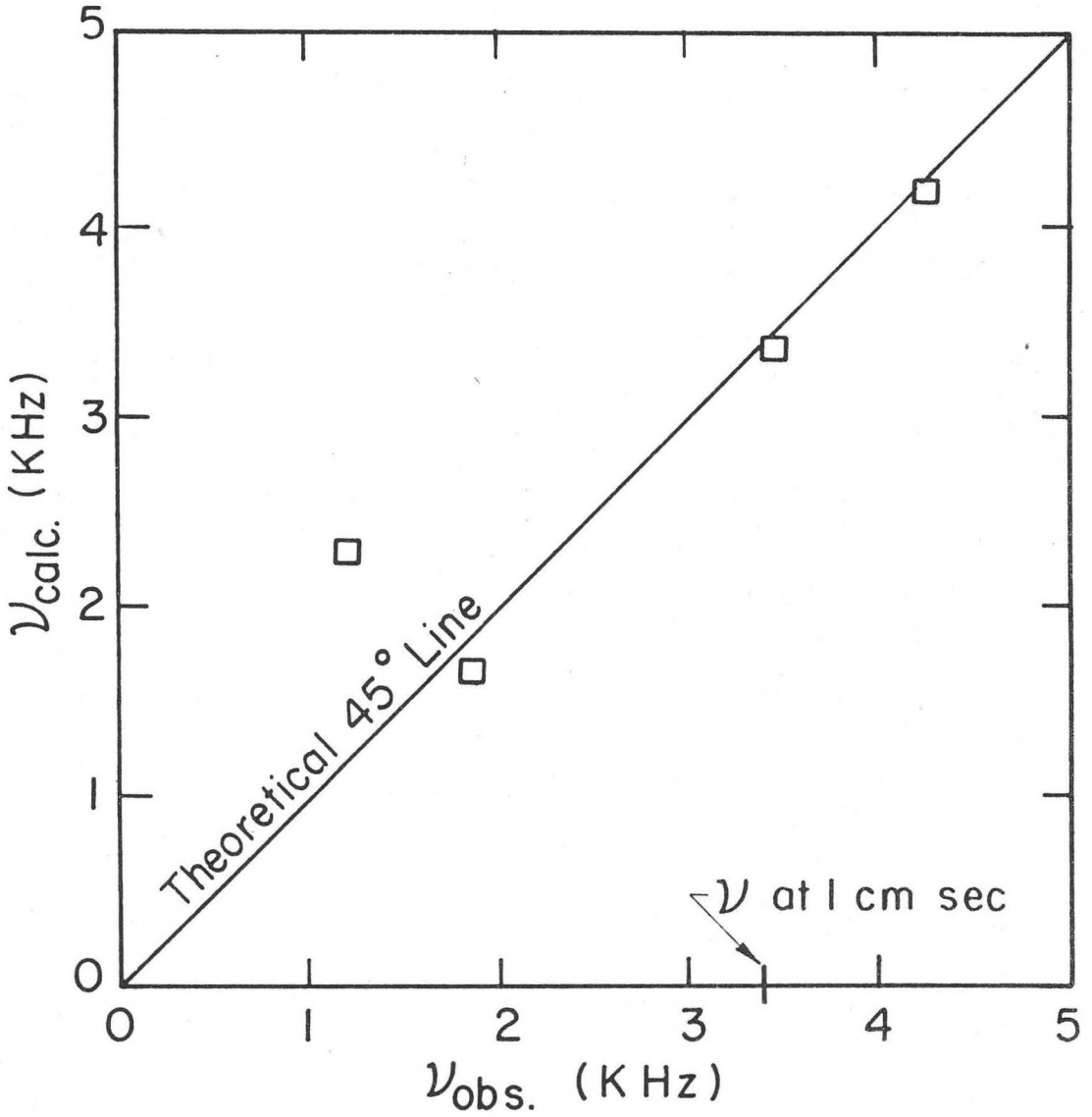

XBL 768-7419

Fig. 42. Doppler beat frequency ν_{obs}, as observed on the spectrum analyzer is compared with the calculated frequency ν_{calc} which corresponds to the average velocity of the fluid in the channel as determined from the displacement rate of the piston pump.

0 0 0 0 4 6 0 8 0 9 5

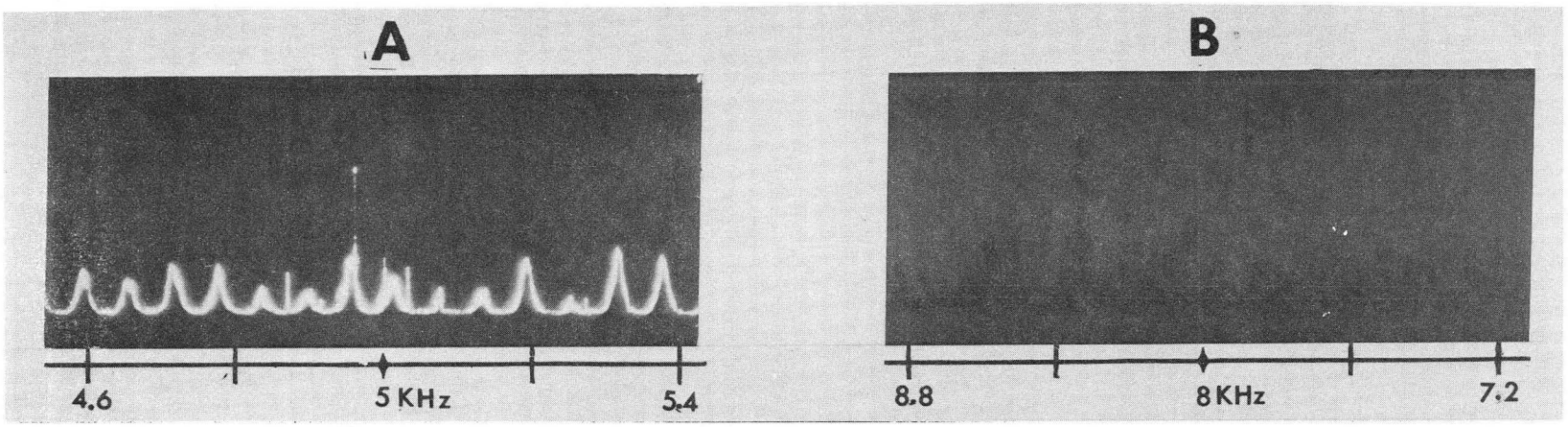

XBB 768-7818

Fig. 43. Spectrum analyzer (oscillograph) tracings of signal peaks obtained from experiments on the miniature flow channel show the peaks to be extremely narrow. The scan rate of Photo A, .2 KHz/div., is twice that of Photo B. The longer scan rate allows the a longer period for the spectrum analyzer to add up the amplitudes of the waves at any particular frequency. Hence the peak of Photo B is twice as large at that of Photo A. Photo A at 8.05 KHz there is a signal peak of .6 microvolts. An adjacent larger peak at 8.35 KHz is an induction peak resulting from the sudden switching off of the piston pump motor. The other broad peaks below .5 microvolts are harmonic peaks of noise. Photo B also shows the harmonically spaced pattern of the noise peaks. A fairly large peak occurs at 4.95 KHz. The peak is extremely monochromatic. This signal could result only if the signal was produced by a large contaminating (dust) particle traversing the probe volume. A peak produced from the 2.02 micron light scattering particles seeded into the water of the flow channel would have formed a broad peak containing about 100 signals per Hz scanned.

C. Rotating Disk

To further test whether the electronics were inadequate or whether scatter intensities were too low, a 2.820 in. radius, quarter inch aluminum disk was plated with a white satin finish of silver and mounted onto a synchronous 1 rpm motor. Measurements were then taken along the edge of the disk in the differential mode, giving various tangential velocities (Figs. 6 and 7).

Because the reflection coefficient of the metal especially silver, is high, the signal intensity was greatly increased. During experiments a screen placed before the spectral filter showed a red glow and the outline of the central hole of the mask mirror (Fig. 6 mirror D). No light was visible on the screen for the seeded latex solutions. The satin finish consisted of many surface irregularities that can be assumed to act as light scattering centers similar to the latex suspension. Thus the residence time of scattering in the probe volume of the flow channel and scattering of the disk should be the same.

The results of these disks experiments using a 1 rpm and a 25 rmp motor with a variac speed control on the same disk is presented in Figs. 44 and 45. Hence one can now see that the backscatter intensity is either too low, or that noise from stray light is burying the signal. For the latter, the superposition of a high frequency (megahertz) signal onto one of the incident laser beams, which would also give directional sensitivity, would shift the signal out of the high noise range. But this would have required considerable investment for both new processing electronics and the acousto-optic or other frequency

0 0 0 0 4 6 0 8 0 9 6

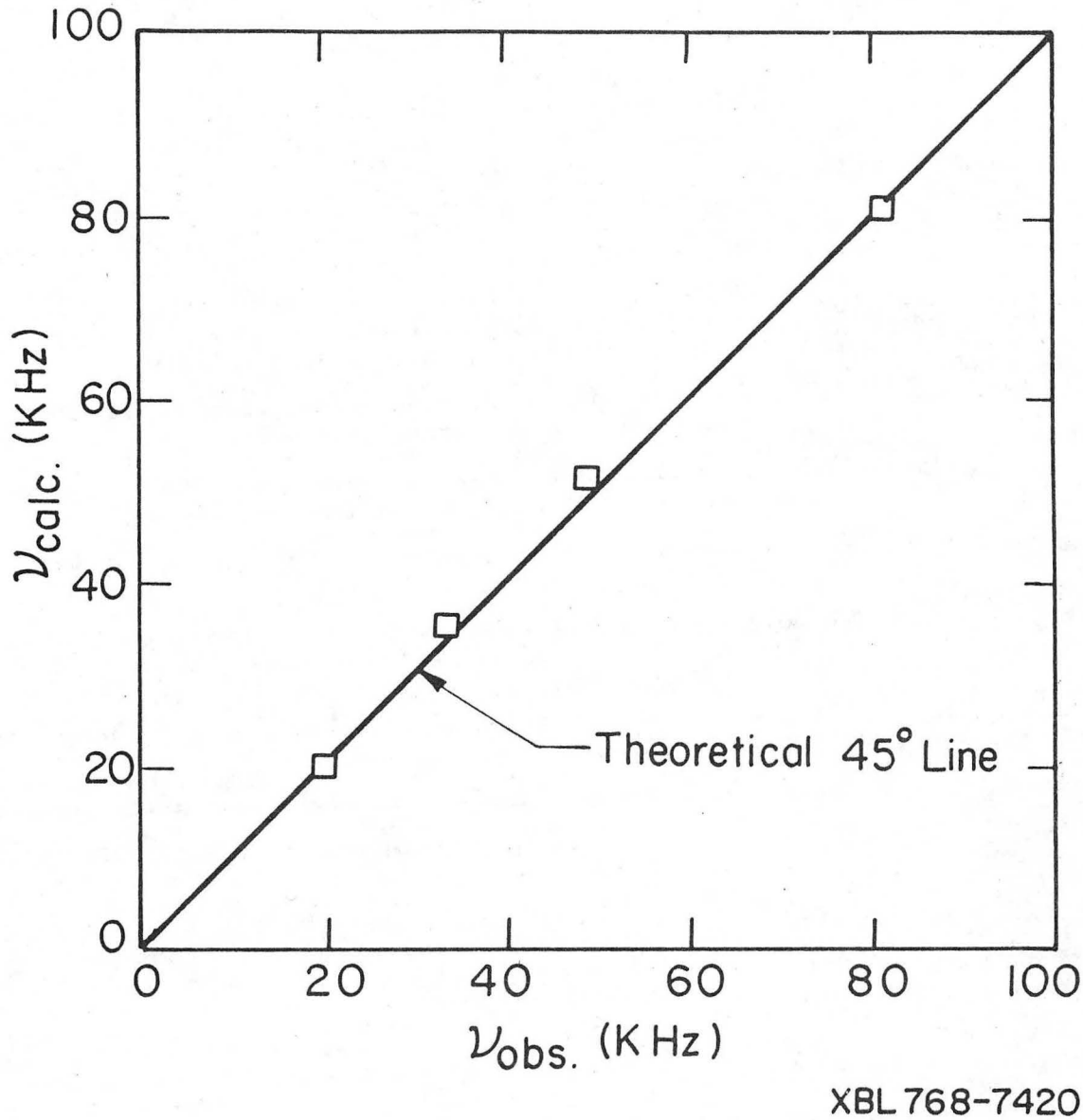

Fig. 45. Theoretical Doppler beat frequency ν_{calc} corresponding to various rates of rotation of the rotating disk is plotted against the signal observed ν_{obs}, on the spectrum analyzer for these rates of rotation.

Fig. 44. Photographs of the spectrum analyzer displays of the Doppler beat frequency are shown. The shifting of the frequency peak demonstrates that in the differential mode the velocity perpendicular to the lens axis and in the plane of the illuminating beams is measured. The probe volume was moved along the edge of the rotating disk shown in Fig. 6A. The velocity measured by the velocimeter is the rate of rotation times the tangent of the angle formed by the lens axis and the tangent line of the circle at the location of the probe volume. Scale of vertical axis is in 1 mV/div.

Photo 0 is viewing the disk at normal incidence (as in Fig. 6A) but the rate of rotation is 0 rpm.

Photo 1 is viewing the disk at normal incidence the rate of rotation of the 2.82 inch radius disk is 1 rmp.

Photo 3A is viewing the disk at roughly 55° incidence, the rate of rotation is 1 rpm.

Photo 3 is done at the same conditions as Photo 3A, except that the spectrum analyzer sweep rate is halved. This should double the resolution. Note that the signal and noise peak heights are both larger than those of Photo 3.

Photo 2 rate 1 rmp, angle of incidence very roughly 30 deg.

Photo 4 rate 1 rmm, angle of incidence is very roughly 60 deg.

0 0 0 0 4 6 0 8 0 9 7

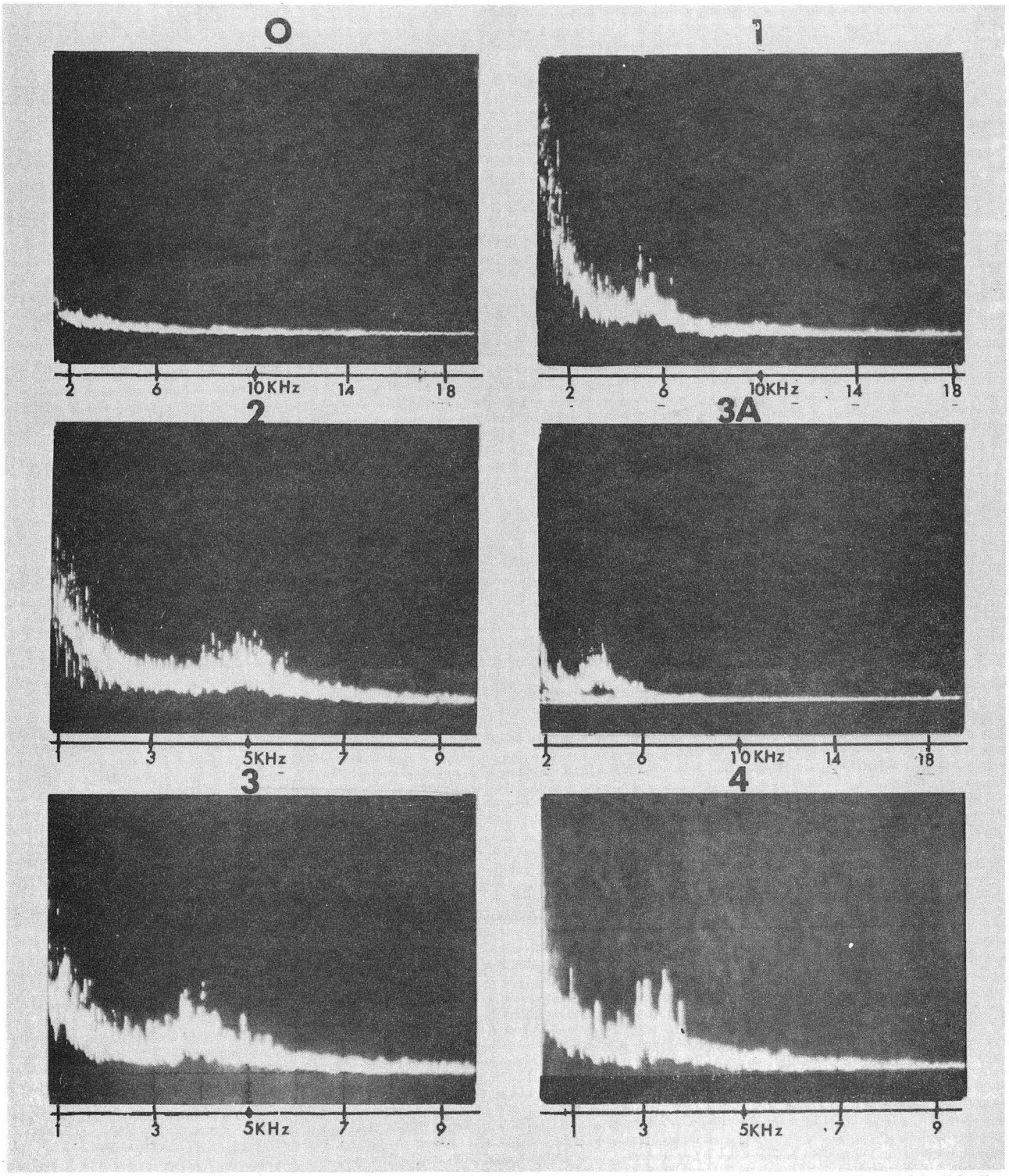

XBB 768-7817

Fig. 44.

shifting device.

D. Hollow Metallized Glass Spheres

Alternatively the signal strength could be increased to above the forward scatter intensities of latex particles by using metal particles in backscattering. While metal flakes show a very high reflection, (Al or brass from commercial watercolors) no signal was recorded. It may have been that the particles flow preferibly with their edges to be beams (least resistance to fluid flow), or tumble in the fluid. In either case the scattering profile would not be the expected cardioid scatter angle diagram expected of metal spheres.

A third experiment was then tried to increase signal strength by applying metal coatings to hollow glass spheres (eccospheres).[84] Floating quartz spheres placed in a silvering solution for mirroring semimirrors by electroless plating[85] resulted in a non adhering white silver mossy precipitate, while the non floating glass spheres became evenly coated with a black coating. The spheres were next soaked in a gold chloride-(1g/lit) activating solution, filtered, and then placed in electroless copperplating[86] solution. A stannous chloride -HCl sensitizing bath followed by a $PdCl_2$- concentrated HCl bath for activation could have been used in place of the $AuCl_3$ bath, as well as a number of other electroless plating formulae and metals.[87,90] But the gold-copper scheme was the simplest, and caused the least difficulty in obtaining the necessary chemicals.

Of the three varieties of Eccospheres used, (silica, BK and high strength spheres) only the high strength spheres were noticeably sensitized by the $AuCl_3$. After 48 hours of soaking in the Au^{+3} sensitizing solution the spheres were filtered and rinsed. Only the high strength spheres appeared to be tinted yellow by the solution. After the spheres were dried, they were immersed in the copper electroless plating solution. Upon addition of the high strength spheres, the initially blue solution, immediately turned green. A number of the white high strength spheres soon appeared to be plated with copper. When the silica (quartz) and BK spheres were added to the plating bath, the bath remained blue. For the above two types of spheres, the copper deposited preferentially on the unsensitized flask wall rather than on the particles. When the particles from these two solutions were filtered after the 3 hour period allowed for plating, the spheres still appeared white. It may have been that the silica and BK spheres were coated with a substance which inhibited plating. After filtering the high strength spheres only a small number of spheres appeared to be coated. The bulk of the spheres were a gray in color. The few spheres which became metallized were unfortunately, like the previous trials with silverplating, coated with a black metallic coat.

Limited time prevented further investigations into various ways to metallize the hollow glass spheres. Because the spheres are of a fairly low density, they can be plated with a fairly thick coat of metal before their density approached that of the water. Hence there was a possibility of making small spheres of neutral bouyance with a

very high backscattering intensity. Such particles would be ideal for use as light scattering particles in our backscatter operation velocimeter. Figure 48 shows the preponderantly backscatter scattering intensity distribution for a metallized sphere.

0 0 0 0 4 6 0 8 0 9 9

Symbols:

A direction of incident beam

r_p radius of the light scattering sphere

i_2 scattering intensity for the light polarized normal to the incident axis and vibrating in the plane of the page.

i_1 scattering intensity for light polarized pendicular to i_2 and the incident axis.

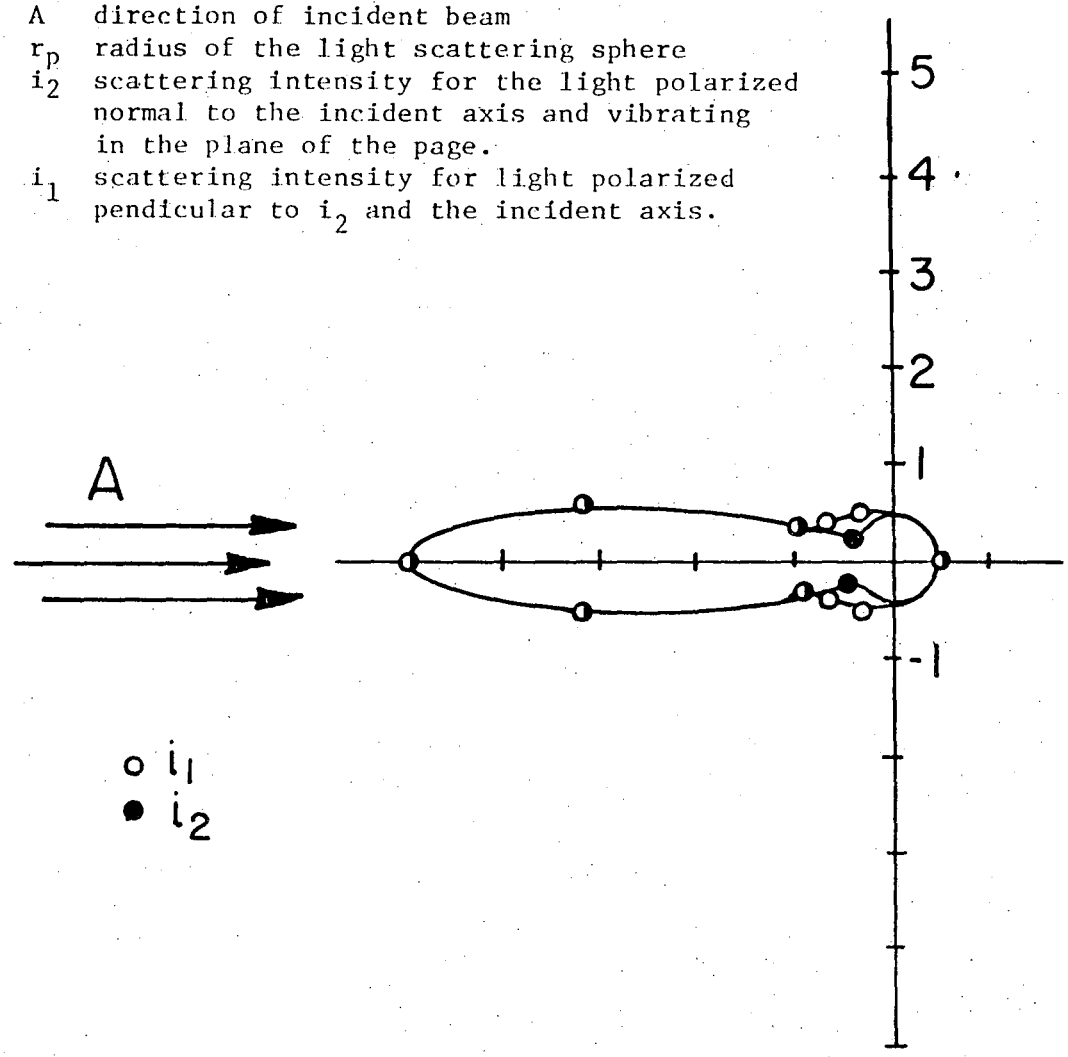

XBL 768-7434

Fig. 48. Scattering intensity distribution pattern[81] for a metallized (index of refraction is infinity) sphere with a 2 micron diameter ($m=r_p 2\pi/\lambda=10$). The scatter intensity is confined to a narrow backscattering lobe ($A=180°$). The scattering pattern is just opposite that of dielectric spheres, see Fig. 17.

VI. CONCLUSION

A laser Doppler velocimeter has been built with a sufficiently high spatial resolution and accuracy in the determination of the location of the probe volume to map the flow field of a hydrodynamic boundary layer. In the differential mode, the axes of the ellipsoidal probe volume are 19.6, 19.3 and 68 microns. The reference mode volume is determined by the parabolic profile of the illuminating beam and the ellipsoidal profile of the probe region determined by the spatial filter. The reference mode probe volume is a truncated ellipsoid (axis parallel to lens axis = .23 mm), with dimensions transverse to the focusing lens axis truncated by the parabolic beam profile (focal waist radius = 10.8 microns). The velocimeter operates sequentially in the reference mode and in the two orthogonal positions of the differential mode to give the three velocity components at the same probe volume. The focusing lens is positioned by three stacked translators with micrometer drives (.01 mm divisions with 50 mm travel). The lens and hence its focal volume, probe volume, can thus scan the region of interest with three degrees of translational freedom.

Light deflection of the illuminating beams and signal beam is minimized by using a backscatter design and observing the electrode at an angle to the surface. Experiments with the laser velocimeter have shown that the backscatter signal intensities are quite low when dielectric light scattering particles (Dow latex spheres) are used. Large light scattering particles would increase the signal intensity

but the particles may not accurately represent the flow. Light scattering from metallized spheres is mainly backscattered radiation. Further experiments to successfully produce metallized glass spheres of neutral bouyancy may provide the needed stronger signal intensities without the use of higher power and hence more hazardous lasers.

The present spectrum analyzer is adequate for simple experiments but more sophisticated signal process electronics will be needed for detailed hydrodynamic studies. For detailed studies of boundary layer phenomena where the velocity would vary gradually while approaching the wall, tracking electronics such as a phase lock loop would be necessary. While in studies of turbulent eddies, where velocities are random, a multichannel spectrum analyzer would be needed to observe the entire range of possible eddy velocities.

With metallized scattering particles and the necessary processing electronics the present velocimeter should have the capability to make measurements of the flow field of hydrodynamic boundary layers, and in particular make measurements on the boundary at the electrode surface of our electrochemical reactor.

APPENDIX I

The size of the reference mode probe volume is determined by the size of the aperture in the spatial filter. Since light scattering particles outside the parabolic focal volume of the focused laser beam are not illuminated, no signal comes from that region. The beam intensity profile determines the radial dimensions of the probe volume. The location along the z axis (Fig. 20) at which light scattering from particles are blocked by the aperture of the spatial filter determines the size of the axial dimensions of the probe volume. The extent along the axial direction at which scattered light is accepted is Δf, the probe depth. The radius of the spatial filter is R. Various focal lengths, angles and dimensions are as given in Fig. 21. The slope of the ray emanating from the distance $f + \Delta f$ along the axial direction is determined by calculating its displacement from the optical axis at the focal plane, h.

In Fig. 21 for the convergent case, one can apply the oblique ray method to the focusing lens (lens on the left side), to determine the height of the image h, at the focal plane,

$$h = f \tan\theta \qquad \text{(a)}$$

The angle ϕ_c is taken at the edge of the focusing lens and is formed by the angle between the path of a light ray coming from the focal point f of the focusing lens and the path of a light ray coming from the location $f + \Delta f$ away. The light from $f + \Delta f$ enters the lens of the spatial filter at an angle ϕ_c. At f; the location of the focal plane

of the spatial filter aperture, only images shorter than the radius of the aperture of the spatial filter R, will pass through the spatial filter and thus reach the phototube. From geometric arguments,

$$\tan\phi_c = (d-h)/f \quad . \tag{b}$$

For the divergent case where the scattering particle is closer to the focusing lens than the focalpoint, one obtains from inspection of the geometry;

$$h = f\tan\theta \tag{c}$$

and

$$\tan\phi_d = (h-d)/f$$

By applying the oblique ray method to find the at the height of the image h, at the focal plane of the spatial filter lens (the right side of Fig. 21), one obtains (see Fig. 21A) for the convergent case the equation,

$$R = f\ \tan\phi_c \tag{d}$$

and for the divergent case,

$$R = f'\ \tan\phi_d = -f'\tan\phi_c \ . \tag{e}$$

In order to express Δf as a function of R, Δf must be related to the angles ϕ and θ.

Referring back to the left side of Fig. 21, one can see that

$$\tan\theta = d/(f + \Delta f)$$

for the convergent case, and (f)

$$\tan\theta = d/(f - \Delta f)$$

for the divergent case.

Fig. 21. Axial dimension of reference mode probe volume as determined by the spatial filter, Δf

Symbols:

d	Radius of focusing lens
f	Focal length of focusing lens
f'	Focal length of first lens of spatial filter
h	Distance between the axis of the focusing lens at the focal plane to the location of the ray emanating from a distance of $f+\Delta f$ along the focusing lens axis
H	Radius of spatial filter lens
L	Distance along the lens axis where the ray mentioned in h intersects the lens axis while in the spatial filter
P_o	Distance between focusing and spatial filter lenses
θ_1	$\tan\theta_1 = d/f$
R	Radius of pinhole
$\phi_{c,d}$	Angle of slope of the ray described in h
ω	Slope of ray described in h as it is focused by the spatial filter lens

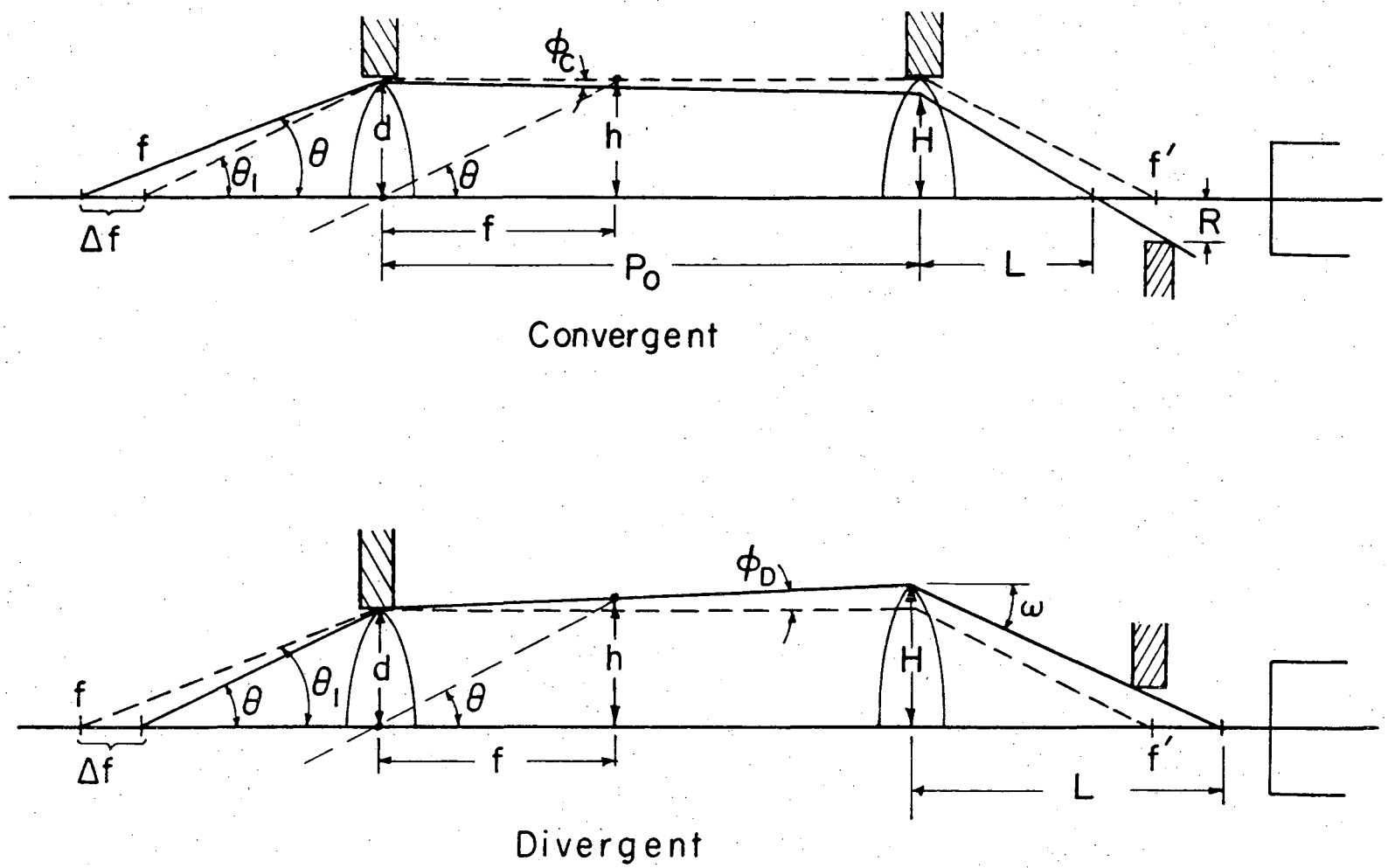

XBL 768-7439

Fig. 21.

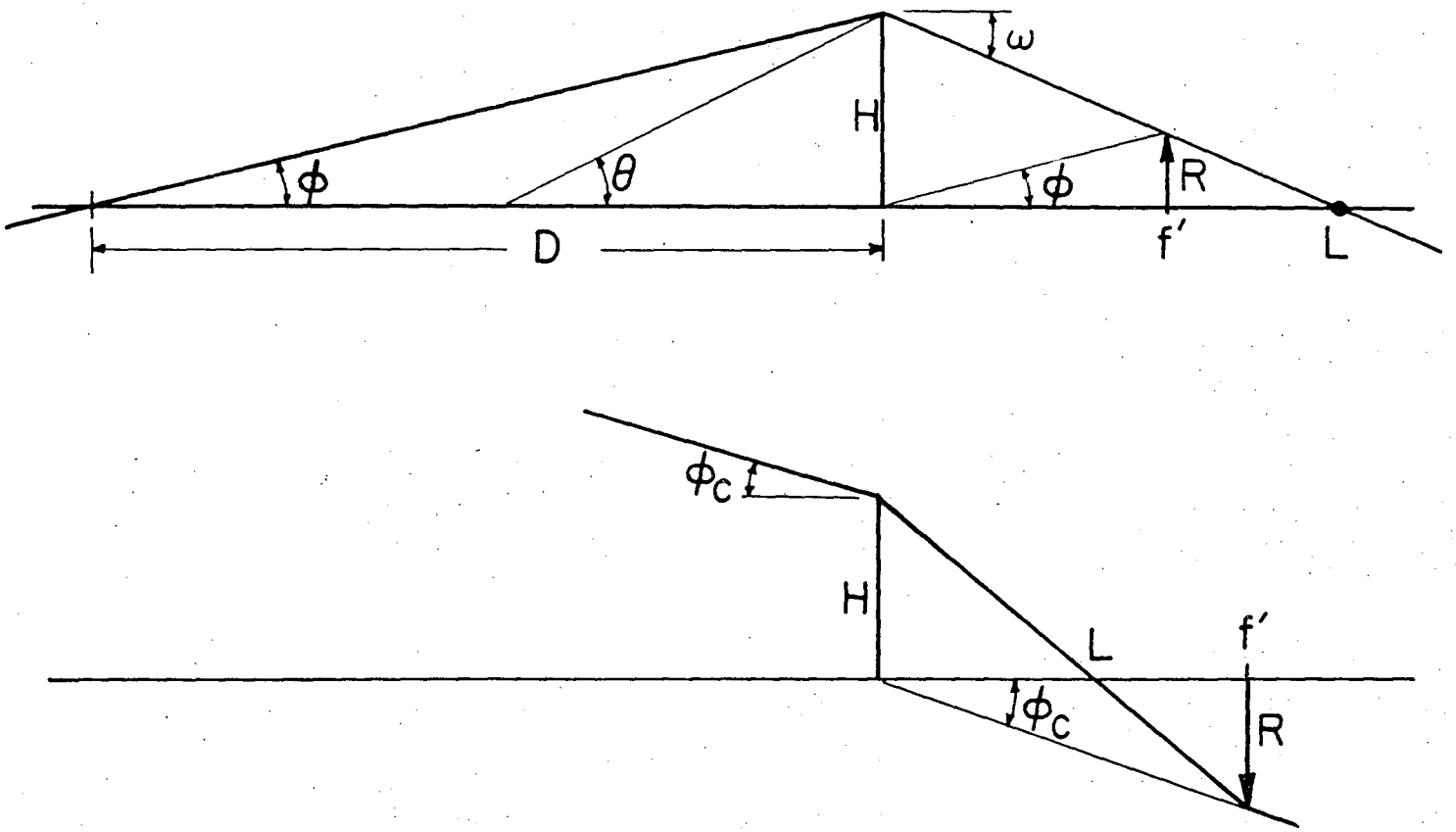

XBL 768-7440

Fig. 21 (Cont'd).

From Eqs. (b) and (c), ϕ can be expressed as a functions of h. Equations a permits h to be expressed as a function of θ. Hence

$$\frac{f \tan\phi_c}{d} = h = f\tan\theta. \qquad (g)$$

And substituting the expression for $\tan\theta$ into Eq. (f), one obtains

$$R = \frac{(f'd)}{f} \cdot \frac{(-\Delta f)}{(f + \Delta f)}$$

Note that R is independent of the distance between the focusing and spatial filter lenses, P_o. Since $\Delta f \ll f$, then

$$R = \frac{(f'd)}{f^2} \Delta f$$

With R = .05 mm, f = 50 mm, f'+88 mm fl., and d = 11 mm, one obtains the expression R = .03 Δf.

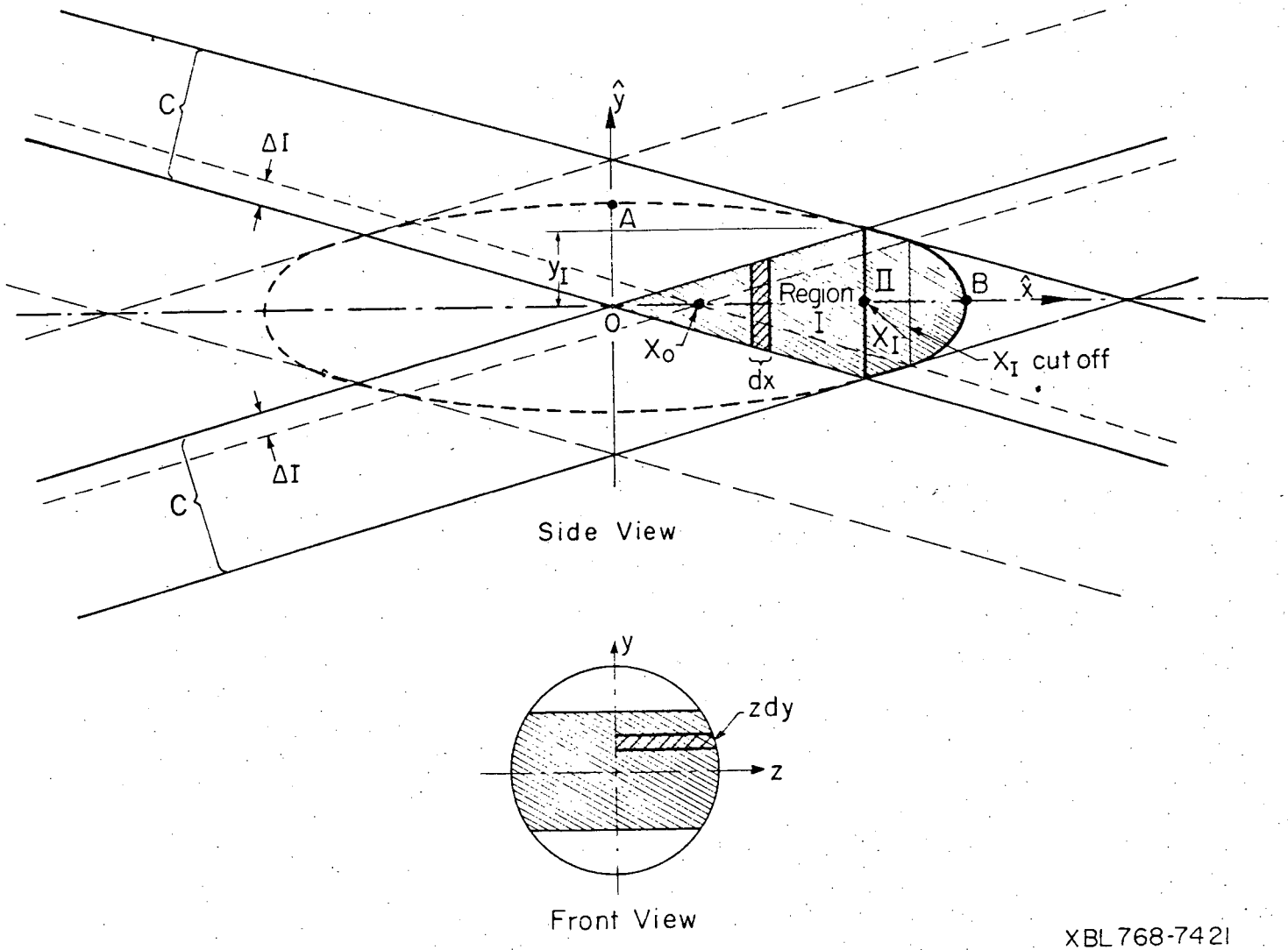

XBL 768-7421

Fig. 47. The intersection of two truncated Gaussian beams forms the shaded figure. Region I is a wedge shaped region, while Region II is a nosecone shaped region. When the beams have a circular cross section instead of the semicircular cross sections of the truncated beams, the figure outlined by the dotted line, an ellipsoid, forms.

0 0 0 0 4 6 0 8 1 0 4

APPENDIX II

(Differential mode probe volume with the geometric beam splitter)

The intersection volume of two semicircular cross section beams is shown in Fig. 47. The intersection volume corresponds to the probe volume of the geometric beam splitter shown in Fig. 28. From Fig. 47 one can see that the probe volume which is a slice of an ellipsoid is composed of two sections, a wedge shaped section, I, and a nosecone shaped region, II.

The volume of the nosecone V_{II} can be calculated as the a stack of ellipsoidal plated stacked from $x=x_1$ to $x=b$. The volume calculated in this manner is

$$V_{II} = \int_{x_I}^{b} c\sqrt{1-(x/b)^2} \quad a\sqrt{1-(x/b)^2} \quad dx$$

$$V_{II} = \pi ac(x - x^3/(2b^2))\Big|_{x_I}^{b}$$

Calculating x_I, the intersection of the wedge and nosecone regions: Calculation of the volume of the wedge V_I is somewhat more involved. The equation of the ellipsoid of Fig. 47 is

$$(x/b)^2 + (y/a)^2 + (z/c)^2 = 1 \ .$$

In the xy plane at $z = 0$, the cross section of the ellipsoid is the ellipse

$$(x/b)^2 + (y/b)^2 = 1.$$

The ellipse intersects the wedge portion of the probe volume at $x=x_I$. The slope of the wedge is $y-x\tan\psi$. Ey equating y from the equation of the ellipse at the nosecone portion with y from the slope of the wedge, one can solve for x_I.

$$x_I = 1/((\tan\psi/a)^2 + 1/b^2)^{1/2}$$

The above results are valid for beamsplitters with an infinitely thin edge. If one accounts for the blunt edge of the prism which truncates a portion of the intersecting beams, then the intersection volume is reduced, (area bounded by the -·- lines). The width of the blunted portion of the edge is $2\Delta l$. The volume of the wedge shaped portion of the intersection volume is now taken from the points $x=x_0$ to $x=x_{Icutoff}$ (see Fig. 47).

$$x_0 = \Delta l \cdot \cos\theta$$

and

$$x_{Icutoff} = \frac{2x_0\tan\psi}{a^2} + \frac{4x_0^2 \tan^2\psi/a^4 - 4(x_0^2/a^2-1)(1/b^2-\tan^2\psi/a^2}{2(1/b^2 - \tan^2\psi/a^2)}$$

To obtain the wedge volume one can slice the wedge into slices of thickness dx, with each slide having the cross sectional area shown in the lower figure of Fig. 47. The area of the cross section is made up of slices z long and dy wide, or

$$\text{Area of cross section} = 4 \int_0^x z\, dy,$$

where

$$z = \sqrt{1 - (x/b)^2 - (y/a)^2} \quad .$$

The wedge volume, V_I is thus,

$$V_I = 4c \int_0^{x_I} \int_0^{x\cdot\tan\psi} \sqrt{1-(x/b)^2-(y/a)^2}\, dy\, dx$$

Let $r_x^2 = a^2(1-(x/b)^2$, then

$$\int_0^{x\tan\psi} \sqrt{1-(x/b)^2-(y/a)^2}\, dy = a \int_0^{x\tan\psi} \sqrt{r_x^2 - y^2}\, dy$$

$$= a\left(\frac{1}{2}\, y(r_x^2 - y^2)^{1/2} + \frac{1}{2}\, r_x^2 \sin^{-1}(y/r_x)\right)\Big|_0^{x\tan\psi}$$

Substituting $a(1-(x/b)^2)$ for r_x, taking the limits and collecting terms,

$$V_I = \int_0^{x_I} \frac{ax\tan\psi}{2} (a^2-x^2((a/b)^2)-x^2\tan^2\psi)^{1/2} + \frac{a^2}{2}\,(1-(\tfrac{x}{b})^2)\sin^{-1} \frac{x\,\tan\psi}{a(1-(\tfrac{x}{b})^2)^{1/2}}$$

$$+ \frac{a^2}{2}\,(1-(\tfrac{x}{b})^2)\sin^{-1} \frac{x\,\tan\psi}{a(1-(\tfrac{x}{b})^2)^{1/2}}\, dx$$

Setting $D^2 = a^2/(\,(a/b)^2 + \tan^2\psi) = a^2/(2\,\tan^2\psi)$

and letting $V_I = I_I + I_{II}$, then

$$I_I = (\,(a/b)^2 + \tan^2\psi)^{1/2}\,(\frac{a\,\tan\psi}{2}) \int_0^{x_I} x\sqrt{D^2-x^2}\, dx$$

$$I_I = -(a\,\tan^2\psi/3\sqrt{2})(D^2-x^2)^{3/2}\Big|_0^{x_I}$$

$$I_{II} = \frac{1}{2} \int_0^{x_I} a^2(1-(x/b)^2)\,\sin^{-1}\,(\tan\psi x/(a(1-(x/b)^2)^{1/2})\, dx$$

To solve I_{II}, let $u = x/(a(1-(x/b)^2)^{1/2})$. Rearranging the equation, one obtains, for $u \geqslant 0$ and $x \geqslant 0$,

$$x = au/\sqrt{(ua/b)^2 + 1)}$$

and

$$x/u = a/((ya/b)^2 + 1)^{1/2} .$$

The increment dx can also be expressed as a function of u,

$$du/dx = \frac{1}{a} \frac{d}{dx} \left(\frac{x}{\sqrt{1 - (\frac{x}{n})^2}}\right) .$$

Carrying out the differentiation and substituting in the definition of u and x/u,

$$du/dx = (u + (a/b)^2 u^3)/x$$

or

$$dx = du \cdot \frac{a}{(1+(a/b)^2 u^2)^{3/2}} .$$

Now the dx and x's of I_{II} can be substituted for u's.

$$I_{II} = \frac{a^3}{2} \int_0^{u_I} \frac{\sin^{-1}(\tan\psi u)}{(1+(ua/b)^2)^{5/2}} du$$

The integral is not tabulated in tables of integrals, so as an approximation the first four terms of the series expression for the arcsin will be substituted into the integral. The approximation is acceptable since the z^7 coefficient is only .0446,

$$\mathrm{Sin}z^{-1} = z+z^3/2\cdot 3 + \frac{1\cdot 3}{2\cdot 4\cdot 5} z^5 + \frac{1\cdot 3\cdot 5}{2\cdot 4\cdot 6\cdot 7} z^7 + \ldots \quad \text{so}$$

$$I_{II} = \frac{a^3 \tan\psi}{2} \int_0^{u_I} \frac{u^5 du}{\sqrt{1+(ua/b)^2}} 5 + \frac{15a^3 \tan^7\psi}{672} \int_0^{u_I} \frac{u^7\, du}{\sqrt{1+(ua/b)^2}} 5 + \ldots$$

The above integrals are found in integral tables under the functions:

$$\frac{u^n\, du}{r^m}$$

where

$$r = (u^2 + A^2)^{1/2} ,$$

Let Λ be the ratio b/a, and $u_1 = x/(a(1-(x/b)^2)^{1/2})$ with x evaluated at x_I. Solving the integrals, gives I_{II}

$$I_{II} = (\frac{b}{a})^5 \cdot (\frac{a^3 \tan\psi}{2} \frac{1}{3r^3} + \frac{a^3 \tan^3\psi}{2} (\frac{-1}{r} + \frac{A^2}{3r^3}) +$$

$$\frac{3a^3 \tan^5\psi}{50} (r + \frac{2A^2}{r} - \frac{A^4}{3r^3}) +$$

$$\frac{15\, a^3 \tan^7\psi}{672} (\frac{r^3}{3} - 3A^2 r - \frac{3A^4}{r} + \frac{A^6}{3r^3}) \Big|_{r_0}^{r_I}$$

where $r_1 = (u^2+A^2)^{1/2}$ evaluated at x_I

and $r_0 = (u^2+A^2)^{1/2}$ evaluated at x=0

For the beamsplitter, $\Lambda x = b = 120$ microns

$\Delta y = a = 19.6$ microns

$\Delta z = c = 19.3$ microns

$\Lambda = b/a = 12$ and $\tan\psi = 8.3\times 10^{-2}$

the above dimensions give: $x_I = 85.6$ microns

$y_I = 14.$ microns

and

$$D^2 = a^2/(a \tan^2\psi) = 7463.3$$

The intersection volume is then,

for the wedge, region I, $V_I = I_I + I_{II} = 45{,}100$ micron^3

for the nosecone, region II, $V_{II} = 11{,}200$ micron^3 and,

for regions I and II, $V_{truncation} = 56{,}300$ micron^3.

The volume of the ellipsoid is $\frac{4}{3}\pi abc$, so $V_{ellipsoid} = 2\times10^5$ micron^3.

The volume ratios are:

$$\frac{V_{wedge}}{V_{ellipsoid}} = 22.6\%$$

$$\frac{V_{nosecone}}{V_{ellipsoid}} = 5.6\%$$

and

$$\frac{V_{truncation}}{V_{ellipsoid}} = 28.2\% .$$

Therefore the probe truncated volume obtained with the geometric beamsplitter is only 28% of the ellipsoid volume obtained by the amplitude beamsplitter.

0 0 0 0 4 6 0 8 1 0 7

$$\Delta y = y_a - y_b = 2d\ (2\ \frac{\sin\theta\ \cos\theta}{\sqrt{n^2-\sin^2\theta}} - \cos\theta)$$

To obtain the angle of incidence for axisymmetric splitting one takes the derivative of Δy with respect to θ and sets it equal to 0. The minimum of Δy occurs at the angle of incidence which gives axisymmetric splitting of the output beams.

$$\frac{d}{d\theta}\ (\ \frac{\sin\theta\ \cos\theta}{\sqrt{n^2-\sin^2\theta}} - \sin\theta) =$$

$$\frac{R\ \frac{d}{d\theta}\ (\sin\theta\cos\theta) - \cos\theta\sin\theta\ \frac{d}{d\theta}\ (\sqrt{R})}{R^2}$$

where

$$R = \sqrt{n^2 - \sin^2\theta}\ .$$

The derivative of Δy is thus,

$$\frac{d(\Delta y)}{d\theta} = 4d\ (\frac{\cos^2\theta-\sin^2\theta}{R} + \frac{\sin^2\theta\cos^2\theta}{R^{3/2}}\ ) - 2d\cos\theta$$

There is no nontrivial solution to $d(\Delta y)/d\theta = 0$, so one obtains the solution to $d(\Delta y^2)/d\theta = 2\Delta y\ d(\Delta y)/d\theta = 0$.

A computer program calculating $d(\Delta y^2)/d\theta$ at various value of θ was used to obtain the angle for axisymmetric splitting, which occurs when the deriative is 0.

Symbols for the program below:

S	$\sin\theta$
C	$\cos\theta$
DY	$\Delta y = y_a - y_b$
R	$(n^2 - \sin^2\theta)^{1/2}$
HTOT	$y_{tot}/d = (y_a + y_b)/d$
F	$d(\Delta y^2)/d\theta$

```
      PROGRAM SNELL(INPUT,OUTPUT)
      READ 1,TH,ETA,DEL,N
    1 FORMAT(3F10.5,I2)
      DO 2 I=1,N
       A=3.141592654*(TH+FLOAT(I)*DEL)/180.
      S=SIN(A)
      C=COS(A)
      R=SQRT(ETA*ETA-S*S)
      F=4.*((C*C-S*S)/R+C*C*S*S/(R*R*R))+2.*C
       HTOT=2.*(S+C/R)
      ANG=A*180./3.141592654
      DY=2.*HTOT-0.*S
      PRINT 3,ANG,F,HTOT,DY
    3 FORMAT(5H ANG=  ,F7.4,12H  DERIV/D=     ,E15.8,6H H/D=    ,F7.4,12H
     1       DELY=  ,F7.4)
    2 CONTINUE
      END
```

```
                                                                                  .E
                                                                                 420
                                                                                2455
                                                                                DELY= -.2490
ANG= 57.6000  DERIV/D=   1.29259867E-01 H/D=   .7181                            DELY= -.2525
ANG= 57.7000  DERIV/D=   1.14876522E-01 H/D=   .7172                            DELY= -.2560
ANG= 57.8000  DERIV/D=   1.00485436E-01 H/D=   .7164                            DELY= -.2596
ANG= 57.9000  DERIV/D=   8.60867958E-02 H/D=   .7156                            DELY= -.2631
ANG= 58.0000  DERIV/D=   7.16807882E-02 H/D=   .7147                            DELY= -.2667
ANG= 58.1000  DERIV/D=   5.72676026E-02 H/D=   .7138                            DELY= -.2703
ANG= 58.2000  DERIV/D=   4.28474287E-02 H/D=   .7130                            DELY= -.2739
ANG= 58.3000  DERIV/D=   2.84204576E-02 H/D=   .7121                            DELY= -.2775
ANG= 58.4000  DERIV/D=   1.39868815E-02 H/D=   .7112                            DELY= -.2811
ANG= 58.5000  DERIV/D=  -4.53106108E-04 H/D=   .7103                            DELY= -.2847
ANG= 58.6000  DERIV/D=  -1.48993107E-02 H/D=   .7093                            DELY= -.2884
ANG= 58.7000  DERIV/D=  -2.93515364E-02 H/D=   .7084                            DELY= -.2921
ANG= 58.8000  DERIV/D=  -4.38095864E-02 H/D=   .7075                            DELY= -.2958
ANG= 58.9000  DERIV/D=  -5.82732624E-02 H/D=   .7065                            DELY= -.2995
ANG= 59.0000  DERIV/D=  -7.27423653E-02 H/D=   .7056                            DELY= -.3032
ANG= 59.1000  DERIV/D=  -8.72165945E-02 H/D=   .7046                            DELY= -.3069
ANG= 59.2000  DERIV/D=  -1.01696046E-01 H/D=   .7036                            DELY= -.3106
ANG= 59.3000  DERIV/D=  -1.16190224E-01 H/D=   .7026                            DELY= -.3144
```

REFERENCES

1. C. W. Tobias and R. G. Hickman, Z. Phys. Chemie 229, 145-65 (1965).
2. H. Tennekes, Physics Today, 52-61 (January 1974).
3. G. A. Simons and R. S. Larson, Phys. Fluids 17, 8-14 (1974).
4. R. G. Hickman, Ph.D. Thesis, University of California, Berkeley Dept. of Chemistry (1963).
5. F. R. McLarnon, Ph.D. Thesis, University of California, Berkeley, Dept. of Chemistry (1974).
6. K. W. Beach, Ph.D. Thesis, University of California, Berkeley, Dept. of Chemistry (1974).
7. R. J. Goldstein and D. K. Kreid, J. Appl. Mech. 34, 813-8 (1967).
8. N. S. Berman and V. A. Santos, AIChE 15, 323-27 (1969).
9. J. W. Foreman, Jr., E. W. George and R. D. Lewis, Appl. Phys. Letters 7, 77-8 (1965).
10. J. W. Foreman, Jr., R. D. Lewis, J. R. Thornton and H. J. Watson Proc. IEEE 424-5 (March 1966).
11. E. R. Pike, D. A. Jackson, P. J. Bourke and D. I. Page, J. Sci. Instr. (J. Phys. E) Ser. 2, 1 727-30 (1968).
12. R. J. Goldstein, and W. F. Hagen, Phys. Fluids 10, 1349-52 (1967).
13. P. J. Bourke, J. Butterworth, L. E. Drain, P. A. Egelstaff, P. Hutchinson, B. Moss, P. Schofield, A. J. Hughes, J. J. B. O'Shaughnessey, E. R. Pike, E. Jakemann and D. A. Jackson, Phys. Letters 28A, 692-3 (1969).
15. G. Gouesbet and M. Trinite, J. Phys. E: Sci. Intrum. 7, 891-6 (1974).

16. L. F. Jernqvist and T. G. Johansson, J. Phys. E: Sci. Instrum. 7, 246-7 (1974).

17. Y. Yeh and H. Z. Cummins, Appl. Phys. Lett. 4, 176-8 (1964).

18. M. J. Rudd, J. Sci. Instr. (J. Phys. E) Ser. 2 2, 55-7 (1969).

19. W. H. Stevenson, Appl. Opt. 9, 649-52 (1970).

20. M. K. Denham, P. Briard, and M. A. Patrick, J. Phys. E: Sci. Instrum. 8, 681-3 (1975).

21. D. F. G. Durao and J. H. Whitelaw, J. Phys. E: Sci. Instrum. 8, 776-80 (1975).

22. F. Durst and M. Zuré, Appl. Opt. 13, 2562-79 (1974).

23. R. Dändliker and P. D. Iten, Appl. Pot. 13, 286-90 (1974).

24. G. R. Grant and K. L. Orloff, Appl. Opt. 12, 2913-6 (1973).

25. R. J. Adrian, J. Phys. E: Sci. Instrum. 8, 723-6 (1975).

26. C. P. Wang, Appl. Opt. 13, 1193-4 (1974).

27. F. Durst and J. L. Whitelaw, Proc. Roy. Soc. London A324, 157 (1971).

28. J. A. Maynard, T. K. Gaylord and J. H. Rust, Rev. Sci. Instrum. 46, 469-73 (1975).

29. R. L. Simpson and P. W. Barr, Rev. Sci. Instrum. 46, 835-7 (1975).

30. M. J. Rudd, J. Sci. Instr. (J. Phys. E Ser. 2 1, 724-6 (1968).

31. D. K. Kreid, Appl. Opt. 13, 1872-81 (1974).

32. Yu. N. Dubnitshev, V. P. Koronkevich, V. S. Sobolev, A. A. Stolpovski, Yu. G. Vasilenko and E. N. Utkin, Appl. Opt. 14, 180-4 (1975).

33. M. K. Mazumder and D. L. Wankum, Appl. Opt. 9, 633-7 (1970).

34. H. Mishina, T. Koyama and T. Asakura, Appl. Opt. 14, 2326-7 (1975).

35. W. Johnson, A. Dybbs and Robert Edwards, Phys. Fluids 18, 913-4 (1975).

36. J. M. Avidor, Appl. Opt. 13, 280-5 (1974).

37. M. R. Barrault, G. R. Jones and T. R. Blackburn, J. Phys. E: Sci. Instrum. 7, 663-6 (1974).

38. E. E. Uzgiris, Rev. Sci. Instrum. 45, 74-80 (1974).

39. R. E. Anderson, C. E. Edlund and B. W. Vanzant, J. Appl. Phys. 42, 2741-3 (1971).

40. S. Asano, and G. Yamamoto, Appl. Opt. 14, 29-49 (1975).

41. Thermo Systems Inc., 2500 Cleveland Ave., N. St. Paul, Minn. 55113, Phone: (612) 633-0550.

42. DISA Electronics, 779 Susquehanna Ave. Franklin Lakes, New Jersey 07417.

43. Sci-Metrics, Electro-Optics Instrumentation, P.O. Box 377, Tullahoma, Tenn. 37388, Phone: (615) 455-8603.

44. H. Schlichting, Boundary Layer Theory, 6th Ed. McGraw-Hill Book Co., New York , (1968).

45. Leica-Summilux lens, 50 mm, f/1.4

46. Done as a courtesy to the customer by Jodon Engineering Associates, Inc., 145 Enterprise Drive Ann Arbor, Michigan 48103, Phone: (313) 761-4044.

47. Optical Industries, Inc., Part 02WRQ 001, Multiple order Quartz retardation plate.

48. P. Lorrain and D. Corson, Electromagnetic Fields and Waves, 2nd Ed., W. H. Freeman and Co., San Francisco, 1970, pp. 510-1.

49. Spectra Physics, Model 130B He-Ne

50. Ardel Kinematic, Model T-103 (horizontal) and Model TT-103Y (vertical translator).

51. Uniform size latex spheres Dow Diagnostic, P. O. Box 68511, Indianapolis, Ind. 46268, Phone: (317) 257-5271 Ext. 388

52. Phototube RCA 6342

53. Phototube RCA 4526 VI with small shell 12 pin JEDEC NOB12-43 Socket.

54. Tektronix 5L4N Spectrum Analyzer.

55. Tektronix Model 5111 with modification 768T Storage Oscilloscope.

56. Oriel Corporation of America, 15 Market St., Stanford, Conn. 06902

57. Private communication from Unov. of Calif., Berkeley, Physics Department undergraduate laboratory, holography experiment.

58. I. J. Bigio, R. S. Finn and J. F. Ward, Appl. Opt. 14, 336-42 (1975).

59. C. M. Penney, Appl. Phys. Lett. 16, 167-9 (1970).

60. E. A. Ballik and J. H. C. Chan, Appl. Opt. 12, 2607-15 (1973).

61. P. S. Bedi, J. Phys. E: Sci. Instrum. 4, 27-8 (1970).

62. O. Lanz, C. C. Johnson and S. Morikawa, Appl. Opt. 10, 884-9 (1971).

63. E. B. Denison and W. H. Stevenson, Rev. Sci. Instr. 41, 1475-8 (1970).

64. K. A. Blake, J. Sci. Instr. (J. Phys. E) Ser. 2, 5, 623-4 (1972).

65. S. J. Bennett and W. R. C. Rowley, J. Phys. E: Sci. Instrum. 6 963-4 (1973).

66. J. Josefowicz and F. F. Hallett, Appl. Opt. 14, 740-2 (1976).

67. T. H. Wilmhurst and J. E. Rizzo, J. Phys. E: Sci. Instrum. 7, 924-30 (1974).

68. J. H. C. Chen and E. A. Ballik, Appl. Opt. 14, 1839-46 (1975).

69. R. M. Munoz, H. W. Mocker and L. Koehler, Appl. Opt. 13, 2890-8 (1974).

70. D. Davis, ISA Trans. 7, 43-51 (1968).

71. D. B. Brayton, H. T. Kalb, and F. L. Crosswy, Appl. Opt. 12, 1145-56 (1973).

72. K. L. Orloff and S. E. Logan, Appl. Opt. 12, 2477-81 (1973).

74. Flat Glass No. 7913, Corning Vycor, Esco Products, 171 Oakridge Rd., N.J. 07438.

75. John Turney, M. S. Thesis, Univ. of Calif., Berkeley, Dept. of Chemistry (1971).

76. Done as a favor to Jack Borde, Bldg 25, Lawrence Berkeley Lab., Univ. of Calif., Berkeley.

77. D. B. Brayton, Appl. Opt. 13, 2346-51 (1974).

78. Optical Coating Laboratory, Inc., 2789 Giffen Ave., Santa Rosa, Calif. 95401. Phone: (510) 744-2083.

79. D. B. Brayton and W. H. Gochart, Trans. Instrum. Soc. Am. 10, 40 (1971).

80. R. J. Adrian and R. J. Goldstein, J. Phys. E: Sci. Instrum., 4, 505-11 (1971).

81. Van de Hulst, Light Scattering by Small Particles, Wiley, New York, (1957) p.65.

82. Ibid. p.103.

83. Table of Scattering Functions for Spherical Particles, Dept. of Commerce, National Bureau of Standards Applied Mathematics Series 4, January 1949.

84. Eccospheres, Emerson & Cuming, Inc., Gardena, Calif.

85. Chemical Rubber Co., Handbook of Chemistry and Physics 20th Edition, 1935.

86. R. F. Bunshan, Ed., Techniques of Metals Research, Vol. I, part 3, J. Wiley and Sons, N.Y. (1968) p. 1374.

87. Symposium on Electroless Nickel Plating, ASTM Special Technical Publication No. 265 (1959).

88. D. K. Kreid and K. S. Rowe, Appl. Opt. 15, 321-2 (1976)

89. R. Eiden, Appl. Opt. 14, 2486-91 (1975).

90. R. Sard, J. Electrochem. Soc. 117, 7, 864 (1970).

ACKNOWLEDGEMENTS

I am especially grateful to Dr. Rolf H. Muller for his patient guidance under which this work was done. The cryptographic and typing skills of Alice Ramirez and the talented drafting skills of Gloria Pelatowski have transformed my rough original manuscript and drawings into this attractive and presentable manuscript. Special thanks goes to Walter Giba for his invaluable technical assistance without which the velocimeter could not have been built.

This work was performed under the auspices of the U.S. Energy Research and Development Administration.

This report was done with support from the United States Energy Research and Development Administration. Any conclusions or opinions expressed in this report represent solely those of the author(s) and not necessarily those of The Regents of the University of California, the Lawrence Berkeley Laboratory or the United States Energy Research and Development Administration.

TECHNICAL INFORMATION DIVISION
LAWRENCE BERKELEY LABORATORY
UNIVERSITY OF CALIFORNIA
BERKELEY, CALIFORNIA 94720